Revised version with a referee's comments (Mar 25, 2013)

Transitional disks and their origins: an infrared spectroscopic survey of Orion A

K. H. Kim[1], Dan M. Watson[1], P. Manoj[1], W. J. Forrest[1], Joan Najita[2], Elise Furlan[2,8], Benjamin Sargent[3], Catherine Espaillat[4,5], James Muzerolle[6], Tom Megeath[7], Nuria Calvet[9], Joel D. Green[10], Laura Arnold[1,11]

ABSTRACT

Transitional disks are protoplanetary disks around young stars, with inner holes or gaps which are surrounded by optically thick outer, and often inner, disks. Here we present observations of 62 new transitional disks in the Orion A star-forming region. These were identified using the *Spitzer Space Telescope*'s Infrared Spectrograph and followed up with determinations of stellar and accretion parameters using the Infrared Telescope Facility's SpeX. We combine these new observations with our previous results on transitional disks in Taurus,

[1]Department of Physics and Astronomy, University of Rochester, Rochester, NY 14627, USA; khkim@pas.rochester.edu

[2]National Optical Astronomy Observatory, 950 North Cherry Avenue, Tucson, AZ 85719, USA

[3]Center for Imaging Science and Laboratory for Multiwavelength Astrophysics, Rochester Institute of Technology, 54 Lomb Memorial Drive, Rochester, NY 14623, USA

[4]Harvard-Smithsonian Center for Astrophysics, 60 Garden St, Cambridge, MA 02138

[5]Sagan Fellow

[6]Space Telescope Science Institute, 3700 San Martin Dr., Baltimore, MD 21218, USA

[7]Department of Physics and Astronomy, University of Toledo, 2801 W. Bancroft St., Toledo, OH 43606, USA

[8]Visitor at the Infrared Processing and Analysis Center, Caltech, 770 S. Wilson Ave., Pasadena, CA, 91125, USA

[9]Department of Astronomy, University of Michigan, 830 Dennison Building, 500 Church St, Ann Arbor, MI 48109

[10]Department of Astronomy, University of Texas, 1 University Station, Austin, TX 78712

[11]The college at Brockport, State University of New York, Brockport, NY 14420

Chamaeleon I, Ophiuchus and Perseus, and with archival X-ray observations. This produces a sample of 105 transitional disks of "cluster" age 3 Myr or less, by far the largest hitherto assembled. We use this sample to search for trends between the radial structure in the disks and many other system properties, in order to place constraints on the possible origins of transitional disks. We see a clear progression of host star accretion rate and the different disk morphologies. We confirm that transitional disks with complete central clearings have median accretion rates an order of magnitude smaller than radially continuous disks of the same population. Pre-transitional disks — those objects with gaps that separate inner and outer disks — have median accretion rates intermediate between the two. Our results from the search for statistically significant trends, especially related to $\dot{M}$, strongly support that in both cases the gaps are far more likely to be due to the gravitational influence of Jovian planets or brown dwarfs orbiting within the gaps, than to any of the photoevaporative, turbulent or grain-growth processes that can lead to disk dissipation. We also find that the fraction of Class II YSOs which are transitional disks is large, 0.1-0.2, especially in the youngest associations.

Subject headings: accretion, accretion disk — planetary systems: protoplanetary disks — stars: pre-main sequence — infrared: stars — X-rays: stars.

1. INTRODUCTION

Transitional disks (TDs) are protoplanetary disks around young stars which are optically thick and gas-rich, but which have AU-scale radial gaps or central clearings in their dust distribution. Usually the gap, which is depleted of small dust grains, is revealed as a deficit in the host T Tau star's infrared excess, with respect to its siblings. Such disks are thought to represent an evolutionary stage between Class II and Class III young stellar objects (YSOs).[1] Strom et al. (1989) first drew attention to these objects, using examples with small — almost photospheric — infrared excess at short mid-infrared ($5 - 50\mu$m) wavelengths but switching sharply to large and strong excess at longer wavelengths.

[1]As in Evans et al. (2009), we mean by Class II YSO an object with 2-20 μm spectral index between -1.6 and -0.3, which physically corresponds to a (T Tauri) star surrounded by a (radially-continuous) accretion disk which is not viewed close to edge-on. Similarly, by Class III YSO we mean an object with 2-20 μm spectral index less than -1.6, corresponding to a pre-main-sequence star with little or no circumstellar material.

During the past decade, there have been significant improvements on the study of YSOs and protoplanetary disks based on data from the *Spitzer Space Telescope* (Werner et al. 2004) launched in 2003. Detailed studies of disk structure have been possible with mid-IR spectra taken using from the Infrared Spectrograph (IRS; Houck et al. 2004). In particular, there has been major progress revealing the detailed disk structures and uncovering a variety of transitional disks.

After the distinctive spectrum of CoKu Tau/4 was discovered by Forrest et al. (2004), several transitional disks in the Taurus star-forming region were studied in detail with self-consistent disk modeling by D'Alessio et al. (2005) (CoKu Tau/4), Calvet et al. (2005) (DM Tau and GM Aur) and Espaillat et al. (2007a,b, 2008) (LkCa 15 and UX Tau A). Calvet et al. (2005) and D'Alessio et al. (2005) suggested that DM Tau and CoKu Tau/4, respectively, can be explained with an empty central cavity in the disk surrounding the central star, but GM Aur requires a disk structure with a gap separating an inner optically thin disk and an outer optically thick disk to match the observed SED (Calvet et al. 2005). Espaillat et al. (2008, 2010) confirmed that LkCa 15 and UX Tau A have gaps between optically thick inner and outer disks. We will refer in the following to these three types of disks as classical transitional disks (CTDs; e.g. DM Tau), weak-excess transitional disks (WTDs; e.g., GM Aur) and pre-transitional disks (PTDs; e.g., LkCa 15), respectively.

There is generally good agreement with the gap sizes inferred from SED modelling, and direct observations of the outer edges of the gaps. Gaps in some 15 transitional disks have been confirmed by submillimeter interferometry (Piétu et al. 2006; Hughes et al. 2007, 2009; Andrews et al. 2009, 2011), and one of these, LkCa 15, also in near-infrared light scattered by the outer disk (Thalmann et al. 2010). The resolved inner disk of a pre-transitional disk, T Cha, also confirms its gapped structure (Olofsson et al. 2011).

The definition and selection criteria of transitional disks have been far from homogeneous considering all objects called 'transition' or 'transitional' objects from other works. Many authors define transitional disks rather loosely, with diverse nomenclatures[2]. Circumstellar disks with a deficit of dust emission from the inner disk and large 30/13 μm flux ratio indicating an optically thick outer disk have been designated "cold disks" by Brown et al. (2007) and Merín et al. (2010). A more relaxed definition includes disks with a much smaller excess for wavelengths beyond > 13 μm representing a depleted or settled outer disk compared to our definition of transitional disks. Those disks are named "anemic disks" (Lada et al. 2006), "homologously depleted disks" (Currie et al. 2009), or "weak-excess disks"[3] (Muzerolle et al.

[2]The definition of diverse nomenclatures are summarized in Evans et al. (2009)

[3]The definition of WTD (weak excess transitional disk) in this work and in Muzerolle et al. (2010) are

2010). Such SEDs can result from dust settling to the disk midplane (Luhman et al. 2010; Espaillat et al. 2012), or outward truncation of a disk by gravitational interaction with a companion (McClure et al. 2008). Therefore, it is important to clarify by which definition and selection criteria the sample of transitional/transition disks are selected, especially if the sample is to be used for searching for any trends to understand the properties of transitional disks and their origin.

Several physical mechanisms have been suggested to explain inside-out disk dispersal: photoevaporation (Clarke et al. 2001; Alexander et al. 2006a,b; Gorti et al. 2009; Owen et al. 2012); grain growth/coagulation/settling (Dullemond & Dominik 2005; Ciesla 2007); inside-out clearing by Magneto-Rotational Instability (MRI) (Chiang & Murray-Clay 2007; Suzuki et al. 2010; Perez-Becker & Chiang 2011); dynamical effects by stellar/substellar companions (Lubow & D'Angelo 2006); giant planet formation (Marsh & Mahoney 1992; Rice et al. 2003; Quillen et al. 2004; Varnière et al. 2006; Lubow & D'Angelo 2006; Zhu et al. 2011, 2012). To distinguish and understand which mechanisms are dominant for the origin of transitional disks, not only flux density information at all wavelengths for a specific target but also empirical trends from observational data in a large sample are indispensable.

There have been several efforts to use statistical trends among several properties of transitional disks and their host stars to constrain models of the origins of these objects. Kim et al. (2009) analyzed IRS spectra of 13 transitional disks in Taurus and Chamaeleon (1-3 Myr) and found a strong correlation between stellar mass and outer gap radius, R_{wall}. Merín et al. (2010) collected broadband SEDs of some fifteen "cold" disks from several young associations. Including some objects reported in the literature (e.g. Brown et al. 2007; Kim et al. 2009) to improve the sample size, they found the gap radius to scale linearly with $M_\star$, and to be significantly correlated with disk mass, with more massive disks tending to have larger holes. In the somewhat older (4-12 Myr) clusters, Tr 37 and NGC 7160, Sicilia-Aguilar et al. (2010) found the median accretion rates in the transitional-disk systems to be about an order of magnitude smaller than in Taurus and Chamaeleon, but similar to these associations' normal Class II YSOs, in contrast to Najita et al. (2007) who found that accretion rates for transitional disks in the Taurus-Aurigae association are systematically a factor of 10 smaller than the normal Class IIs.

In this paper, we present IRS spectra of 62 newly selected transitional disks in the Orion A star-forming region and near-IR spectra of 52 of them from SpeX/IRTF followup observation. Orion A consists of the Lynds 1640 dark cloud which includes the Orion Nebula Cluster (henceforth ONC) and the Lynds 1641 (henceforth L1641). This cloud stretches over

---

different.

~ 30 deg^2 on the sky with Declination from -4^d30^m to -9^d. In this paper, we assume objects to the north of $\delta_{J2000} = -6^d$ belong to ONC while objects to the south belong to L1641. The distance to the Orion A complex has been estimated to be somewhere between 300 to 600 pc (Muench et al. (2008) and references therein). Here, we adopt the distance to Orion A as 414 pc based on the study by Menten et al. (2007). We take the median age of ONC members as less than 1 Myr (Hillenbrand 1997a) and that of L1641 members as 1 Myr (Gâlfalk & Olofsson 2008).

We consider 105 transitional disks not only of Orion A including ONC and L1641, but also of Taurus (henceforth Tau; Furlan et al. 2011), Chameleon I (henceforth Cha I; Manoj et al. 2011), Ophiuchus (henceforth Oph; McClure et al. 2010), and NGC 1333 (henceforth N1333; Arnold et al. 2012). From this very large sample of transitional disks selected homogeneously from disk properties measured with IRS spectra, and comprehensive information on mass accretion rates from SpeX spectra and X-ray luminosity, we are now able to search for trends between stellar parameters and disk parameters with robust statistics. We anticipate this work to help in understanding mechanisms responsible for the origins of transitional disks.

In Section 2, we present IRS and SpeX observations and data reduction procedures. In Section 3, we describe the measurements of stellar properties and mass accretion rates. We describe the extraction of the outer gap radius, R_{wall}, after explanation of how we selected transitional disks and their sub-classification in Section 4. We discuss the fraction of transitional disks and age trends in Section 5. In Section 6, we explore correlations and trends of the transitional disks properties and compare them to those of radially-continuous disks where possible. Then, we review and discuss what these findings mean and how they can be used to help our understanding of the origin of transitional disks in Section 7. Summary and conclusions drawn from our finding follows in Section 8.

2. OBSERVATIONS AND DATA REDUCTION

We observed the Orion A star-forming region between 2006 November and 2007 October, during *Spitzer*-IRS campaigns 36, 39, 40 and 44. In all, our targets were 555 objects selected on the basis of their *Spitzer*-IRAC and MIPS colors to belong to YSO Classes 0, I, flat-spectrum and II, with flux densities in excess of 2 mJy at 8 μm and 15 mJy at 24 μm (Megeath et al. 2012). Of these, 303 objects were classified as Class II based on their spectral index between 4.5 μm (IRAC channel 2) and 24 μm (MIPS channel 1) or have the colors of transitional disks seen in other regions; they do not show evidence of envelopes in their IRS spectra, and thus their infrared excess is due to circumstellar disks.. We observed

241 objects (114 in L1641; 127 in ONC) with the IRS with full IRS wavelength coverage of 5-37 μm in the low resolution mode. We observed 62 additional objects located close to the Trapezium region with only partial wavelength coverage (5-14 μm), as the detectors for the longer wavelengths would have been saturated by the bright background emission. We estimate that our sample is complete for star-and-disk dominated objects for which the host-star spectral type is M4 or earlier. Analysis of the full sample will be presented in more detail by Kim et al. (2013, in preparation). The complementary sample of objects with envelopes – Class 0, I and flat-spectrum objects – will be discussed by Poteet et al. (2013, in preparetion).

2.1. IRS/*Spitzer*

The IRS spectra of the 62 transitional disks were selected from among the 241 objects which were observed with the IRS low resolution modules ($\lambda/\Delta\lambda \sim 90$; Short-Low (SL):5.3-14 μm; Long-Low (LL): 14-38 μm), based on the selection criteria described in Section 4. Each object was observed at two nod positions separated by one-third the length of the slit in the staring mode. To extract the spectra, we used version S15.3 of the basic calibrated data (BCD) product from the Spitzer Science Center IRS pipeline for both SL and LL.

To fix bad, hot and rogue detector-array pixels before extracting objects from the 2D spectral images, we generated a set of "grand rogue masks" for Orion A data. A grand rogue mask for the general data reduction process is generated by combining rogue mask files available up to a recent IRS campaign supplied from the Spitzer Science Center, and adding additionally identified rogue pixels from data images. However, we applied additional special treatment to make LL grand rogue masks for these data because (1) the LL array exposure to cosmic rays had increased continuously up to campaign 44 [4], which caused the S/N to decrease and the number of rogue pixels and hot pixels to increase, (2) fluxes from our objects are fainter than similar sources in other nearby star-forming regions due to the greater distance to OriA, (3) the large number of rogue pixels and hot pixels severely degraded the signal-to-noise ratio of our targets, and introduced spectral artifacts when many rogue pixels were grouped in clusters. To avoid rejection of too many pixels which might be perfectly good, we chose only the rogue pixels which appear in the campaign rogue masks more than 10 times through campaign 44. To these we added hot pixels selected by eye from LL 2D images from campaign 39 and campaign 44. The usage of grand mask files

[4]In IRS campaign 45 the bias voltage on the Long Low array was reduced from 1.8 to 1.6 volts and the array temperature was reduced from 4.4 to 4.1 K)

including rogue pixels and hot pixels cannot perfectly clean bad pixels. However, we tested several version of grand rogue masks for our LL data and chose a set of grand rogue masks to apply for all of OriA ClassII data. We fixed those rogue pixels in the grand rogue mask (and the permanently bad pixels) by interpolation in the spectral direction from nearest-neighbor good pixels.

Spectral extraction of Class II YSOs in Orion A is generally much more challenging than in other nearby star-forming regions. This is due not only to the source faintness but also to the range of spatial structure in sky emission from the Orion HII regions, and the high stellar density. We used four source extraction methods to derive the final point-source spectra, choosing among them to optimize the rejection of emission from the sky and other nearby point sources.

As a first, basic source extraction step, we used an automated extractor ("auto") based upon the IRS instrument team's Spectral Modeling, Analysis and Reduction Tool (SMART; Higdon et al. 2004). In auto we extracted sources from the uniformly-weighted signal along a tapered column, 3-5 pixels wide. In this step we used two versions of background-subtracted images: one prepared by subtraction of the two nods ("off-nod"), and the other by subtraction of the sky spectrum in each grating order obtained while the target was being observed in the other order ("off-order"). If there were no serious sky background issues or no additional sources in the 2D images, the spectra taken from images subtracted by off-order or off-nods backgrounds are very similar. We examined each sky-subtracted image and the resulting spectra. If large sky-subtraction artifacts (e.g. spectral lines in the sky, contamination from nearby point sources) remained in both auto products, we re-reduced the data in SMART by using the same tapered column extraction as before, but with sky removed by fitting and subtracting a 0th- or 1st order polynomial to emission outside the span of the target. We designate the tapered column extraction with subtraction of a polynomial sky selected manually as "man".

Usually One of three tapered column extractions gave artifact-free results even when the sky emission had complicated structure, but issues remained for targets with a neighbor closer than four pixels away along the slit. In those cases, we resorted to optimal point-source extraction, using both the AdOpt script in SMART (Lebouteiller et al. 2010) and another routine, OPSE, developed by our group (Tayrien & Forrest 2013, in preparation). They are complementary: AdOpt employs an empirical point response function (PRF) and can fit multiple objects along the slit; OPSE uses an analytical PRF and can make corrections to the spectrum for pointing errors, and thus was useful for extracting our target sources, as it can account other sources in a image.

For the flux calibration of the spectra, we multiplied relative spectral response functions

(RSRFs), which were generated by dividing a template spectrum (M. Cohen, private communication; J. Marshall, private communication) by a calibrator's spectrum, extracted in the same way as the target spectrum. Our photometric standards were α Lac (A1V) for SL, ξ Dra (K2III) for LL, and Mrk 231 (assumed to radiate as a power law) for LL wavelength greater than 32 μm.

We compared the spectra from all different versions of source extraction for each object, then we selected the final spectrum based upon freedom from artifacts. During the process, we combined spectra from different versions of methods if necessary to get the best spectra. For example, we use the combined spectrum for OriA-19: SL from AdOpt and LL from OPSE. Reduction choices for the final selection of spectra are noted in Table 1.

2.2. SpeX/IRTF

52 out of 62 transitional objects in Orion A were observed at Near-IR (0.8-2.4 μm) wavelengths with the medium resolution spectrograph SpeX (Rayner et al. 2003), on the NASA Infrared Telescope Facility (IRTF) on Mauna Kea during the 2010A, 2011A , and 2011B semesters.

We observed our Orion A transitional disks with the Short-wavelength Cross-dispersed mode (SXD) on the nights of 15-17 Feb. 2010 and 25-27 Feb. and 6-10 Nov. 2011. We obtained spectra with various slit widths of 0.3", 0.5" and 0.8" for observations during the 2010A semester depending on the seeing conditions of each night. We used only the 0.8" slit width for the observations 2011 February because the weather and seeing were generally poor. Among the objects observed during the 2010A semester, 8 lacked reliable spectral types in the literature, so we used their spectra for the determination of spectral type as well as accretion rate. Of the 8 objects, OriA-34 was only observed with the 0.3" slit to get the highest resolution (R = 2000) available at SpeX in order to determine the spectral type as well as measure the mass accretion rate under good conditions (seeing $\sim$ 0.3"). The spectra of the other 7 objects were obtained with the 0.8" slit (R $\sim$ 800-1200), sufficient to narrow the spectral type range down to 2-3 sub-types by comparing absorption features of the Na I, Al I, Mg I, Ca I and CO to those of template spectra (Rayner et al. 2009a; Cushing et al. 2005). The details on spectral type determination are described in §2.2.1. For targets with very close neighbors, we oriented the slit so as to observe both simultaneously. For airmass greater than 2 we kept the slit orientation fixed to the parallactic angle. The SpeX/IRTF observation log is given in Table 2. We reduced our spectra with the Spextool package (Cushing et al. 2004), and the flux calibration and telluric absorption correction (Vacca et al. 2003) were done with a spectrum of an A0V star, HD 37887, observed near in

time and close in air mass to each object.

2.2.1. Spectral Type Determination

We list in Table 3 the spectral type of the host star of each of our transitional disks. Most of our spectral-type information is gathered from the literature (Hillenbrand 1997b; Rebull et al. 2000; Allen 1995; Da Rio et al. 2010; Fang et al. 2009; Parihar et al. 2009), or from unpublished results kindly provided by Lori Allen, John Tobin and Jesús Hernández. In addition, we determined several new or improved spectral types from our SpeX spectra. In Figure 1, we show the SpeX spectra of these objects and illustrate our spectral-typing procedure. We used Mg I, Al I, Na I, Ca I, and CO features in the H and K band as the SpeX sensitivity is best in those bands and as those absorption features are very sensitive to spectral types in the G-M range.

It would have been best if the spectral resolution of our target spectra was the same as that of the standard spectra in order to distinguish adjacent lines and spectral depth. However, most of our SpeX spectra were taken at R $\sim$ 800-1200. Only OriA-34 was observed with 0.3 arcsec slit giving R $\sim$ 2000. Even though some lines are blended due to the modest spectral resolution, we were able to narrow down spectral types to about +/− 2-3 subtypes. We adopt the spectral type of the first five objects from top of Figure 1 from the spectral typing using our SpeX spectra. The S/N on OriA-302 is not good enough to determine a sub-class of its spectral type, but OriA-302 is thought to be an M-type star based on the broad spectral features attributable to Mg I, Na I, and CO overtone bands. We found that the uncertain spectral type from HECTOSPEC data (Lori Allen, private communication) of OriA-230, OriA-271, and OriA-294 are in reasonably good agreement with those from our spectra.

2.3. Ancillary Data: Photometry

We also compiled broadband photometry from ultraviolet to mid-infrared wavelengths from the literature. From the Naval Observatory Merged Astrometric Dataset (NOMAD) catalog (Zacharias et al. 2005) we collect B (0.44 μm), V(0.55 μm), and R (0.64 μm). There is a rather recent photometry data set for ONC objects from Da Rio et al. (2010). From their tables, we gathered optical photometry at U (0.347 μm), B (0.454 μm), V (0.538 μm), TiO (0.6217 μm), and I (0.862 μm). Photometry from one more optical band (I at 0.8 μm) was taken from the DENIS database as well as two near-IR bands, J (1.25 μm) and K (2.16

μm). Most of our targets (except OriA-302) have 2MASS photometry in the J (1.25 μm), H (1.65 μm), and K (2.17 μm) bands. We collected 2MASS information from Skrutskie et al. (2006). The photometry in the JHK bands for OriA-302 in Figure 2 are the averaged fluxes from our SpeX spectra. All of our targets were observed with IRAC (3.6, 4.5, 5.8, and 8.0 μm) and MIPS (24 μm) prior to the IRS observations (Megeath et al. 2012). The SEDs (Spectral Energy Distributions) constructed with the broadband photometry are shown in Figure 2.

3. STELLAR PROPERTIES AND ACCRETION PROPERTIES

3.1. Extinction Correction

Extinction toward protoplanetary disks can lead to misclassification of evolutionary stages and misinterpretation of disk spectra. To minimize the effects of extinction toward our targets, we de-reddened our data based on the estimates of visual extinction (A_V) obtained using the following relationship between A_V and the color excess $E(\lambda_1 - \lambda_2) = ([\lambda_1] - [\lambda_2])_{obs} - ([\lambda_1] - [\lambda_2])_{int}$:

$$A_V = \frac{\frac{A_V}{A_{\lambda_2}}}{\frac{A_{\lambda_1}}{A_{\lambda_2}} - 1} \times E(\lambda_1 - \lambda_2) \quad (1)$$

To get a color from two wavelengths, λ_1 and λ_2, we used 2MASS JHK photometry for most of the sample and DENIS IJH photometry for the rest, when available. We measured A_V in several ways for each object. We use either $(J-H)_{2MASS}$, $(H-K)_{2MASS}$, or $(I-J)_{DENIS}$ as an observed color $([\lambda_1] - [\lambda_2])_{obs}$. We adopt $I-J$, $J-H$, and $H-K$ photospheric colors from Kenyon & Hartmann (1995) or $J-H$ and $H-K$ of the Classical T Tauri Star (CTTS) locus of colors from Meyer et al. (1997) as the intrinsic color, $([\lambda_1] - [\lambda_2])_{int}$. To get A_λ, for each set of λ_1 and λ_2, we used the Mathis (1990) extinction curve for $R_V = 5.0$ if the resulting $A_V < 3$. In case of $A_V > 3$, we followed the empirical extinction curves from McClure (2009): two composite extinction curves, one for $3 < A_V < 8$ and one for $A_V > 8$. After calculation of extinction corrections with each intrinsic color choice, we examined the extinction-corrected SEDs and selected a final result based on freedom from artifacts of the correction (e.g. artificial CO_2 ice features or structure in the silicate features) and good agreement with the photospheric spectrum of the star's type, at short wavelengths. (< 1 μm). In Table 3, we list the A_V method selected for each object: $I-J$, $J-H$, and $H-K$.

3.2. Stellar Properties

We list the adopted spectral types in Table 3. Among 62 Orion A TDs, we have 55 objects with well-determined spectral types, one with spectral type constrained to a broad range, and 6 with unknown spectral types. In Figure 3 we show the spectral type distribution of objects with known spectral types in ONC and L1641. The spectral types of ONC objects range from G5 to M5, while that of the L1641 objects are more concentrated around the M1 type. The SpT distribution of 27 TDs in ONC and 28 TDs in L1641 generally agree with the SpT distribution of the general stellar populations of ONC (Rebull et al. 2000) and L1641 (Hsu et al. 2012), respectively.

The effective temperatures, T_{eff}, are adopted from Kenyon & Hartmann (1995) (see Table 4), corresponding to the spectral type of each object. For the objects of unknown spectral types, we used 3850K, the mean T_{eff} of Class II sources with known SpT in Orion A. The stellar luminosity ($L_\star$) of each object was derived from the stellar effective temperature and the stellar radius ($R_\star$). $R_\star$ was calculated from the scaling factor ($(R_\star/d)^2$) applied to the photosphere model, where $d = 414$ pc was assumed to be the distance to Orion A. The photosphere was derived from the intrinsic colors from Kenyon & Hartmann (1995) at temperature T_{eff}, scaled to match the de-reddened the 2MASS J band photometry. The mass of star ($M_\star$) was inferred from the Siess PMS evolutionary tracks (Siess et al. 2000) using the assumed luminosities and effective temperatures. TDs with known spectral types in Orion A are shown on an H-R diagram along with Z=0.02 evolutionary tracks in Figure 4. We also plot H-R diagrams for our TD sample from the Tau, ChaI, Oph, and N1333 associations, which we also use in the present analysis, in Figure 4. We see that the host stars of transitional disks in Orion A lie furthest above the main sequence. This agrees with the generally-accepted age sequence in which Orion A is younger than that of Tau, ChaI, or Oph.

We compiled X-ray observations for our TD sample from a variety of sources. We searched for X-ray data in HEASARC, in the published literature (Güdel et al. (2007) for Tau; Winston et al. (2010) for NGC 1333), and in the Chandra Source Catalog (Evans et al. 2010) for objects in ONC. We were permitted pre-publication access to data from the XMM-Newton survey of L1641 (SOXS, Pillitteri et al. 2013). We have also used data from the Second XMM-Newton Serendipitous Source Catalog (Watson et al. 2009b). The X-ray luminosity L_X we adopt in this work is that within 0.2-12 keV, the total band of XMM-Newton.

These properties, T_{eff}, $L_\star$, $M_\star$, $R_\star$, and L_X are listed in Table 4.

3.3. Mass Accretion Rates: $\dot{M}$

We observed 52 of Orion A transitional disks with SpeX/IRTF in SXD mode from 0.8-2.4 μm to measure mass accretion rates from their hydrogen recombination lines: Paγ (1.094 μm), Paβ (1.282 μm), and Brγ (2.166 μm). From the de-reddened SpeX spectra with the A_V determined as described above, we obtained mass accretion rates of all the objects except the G5 star, OriA-88, which shows strong Hydrogen absorption lines.

The method of mass accretion rate measurement is as follows. We fit each hydrogen recombination line with a gaussian function plus a local continuum. We measure the line luminosity of each line from the fit. Then we use the following relations to convert line luminosity to accretion luminosity L_{acc} (Muzerolle et al. 1998; Gatti et al. 2008):

$$log(L_{acc}/L_{\odot}) = 1.36 \times log(L_{Pa\gamma}/L_{\odot}) + 4.1 \quad (2)$$

$$log(L_{acc}/L_{\odot}) = 1.14 \times log(L_{Pa\beta}/L_{\odot}) + 3.15 \quad (3)$$

$$log(L_{acc}/L_{\odot}) = 1.26 \times log(L_{Br\gamma}/L_{\odot}) + 4.43 \quad (4)$$

whence we obtain the disk-star accretion rate:

$$\dot{M} = \frac{L_{acc} R_{\star}}{G M_{\star}} \quad (5)$$

In Figure 5 we show as an example the results for OriA-59.

In general, the three recombination lines in our spectra yield similar results for accretion rate within a factor of 2-3, so we report the average in Table 4. When fewer than three lines were detected we adopt the resulting average $\dot{M}$ as an upper limit and indicate them as such in Table 4.

4. DISK PROPERTIES

4.1. Transitional Disks: Selection Criteria and Their Variety

Several spectral indices derived from IRS spectra of Class II YSOs have been used as a first step to separate transitional disks from the radially-continuous bulk of the population (Furlan et al. 2009; Watson et al. 2009a; Manoj et al. 2011; McClure et al. 2010; Arnold et al. 2012), which we also use to identify the transitional disks in Orion A. The continuum spectral indices are defined as

$$n_{\lambda_1-\lambda_2} = \frac{\log(\lambda_2 F_{\lambda_2}) - \log(\lambda_1 F_{\lambda_1})}{\log(\lambda_2) - \log(\lambda_1)} \quad . \quad (6)$$

The wavelengths, λ_1 and λ_2, are selected to avoid emission features, and thus to represent the spectral shape of the optically-thick disk continuum emission. This in turn reveals disk structure, both radial (central clearings and gaps) and vertical (degree of flaring). The equivalent width of the 10 μm silicate emission feature (EW(10μm)),

$$EW(10\mu\mathrm{m}) = \int_{8\mu\mathrm{m}}^{13\mu\mathrm{m}} \frac{F_\lambda - F_{\lambda,con}}{F_{\lambda,con}}\, d\lambda \quad , \tag{7}$$

is a measure of the amount of optically thin dust per unit area of optically thick disk.[5] Thus, a large EW(10μm) is a sign of a large amount of optically thin dust and/or an indication of a reduction in disk continuum due to the absence of optically thick disk in the region where the 10 micron emission feature is formed. Here we use the continuum spectral indices along with $EW(10\mu\mathrm{m})$ to identify disks with central clearing or radial gap. The principles are that small values of n_{K-6} — down to the color of photospheres — and large values of n_{13-31} indicate the spectral "transition" that signifies a gap with outer gap radius in the few- to few-tens-of AU range; and that large values of $EW(10\mu\mathrm{m})$ connote warm optically thin dust in gaps.

To find out break points for TDs among the Class II YSOs distribution in these observed parameter spaces, we utilized all (∼600) IRS spectra of Class II YSOs observed in Orion A, Tau, ChaI, Oph, and N1333. Using the properties of TDs already well identified in Tau (Furlan et al. 2011), Cha I (Manoj et al. 2011), Oph (McClure et al. 2010), and N1333 (Arnold et al. 2012) as a guide, we found the breaks occur to at

- $n_{K-6} \leq$ -2.1 (the lowest octile for the distribution of n_{K-6})
- $n_{13-31} \geq 0.5$ (the highest octile for the distribution of n_{13-31})
- $EW(10\mu\mathrm{m}) \geq 4.3$ (the highest octile for the distribution of $EW(10\mu\mathrm{m})$)

---

[5]In our analysis EW(10μm) does not depend much on temperature and composition. As is evident in the ubiquity of 10 μm excesses and silicate emission features, disks around young stars or brown dwarfs always have a distribution of temperatures which exceed that required for efficient excitation of 10 μm continuum (T > 300 K), and therefore are well above that required for the silicate features, which are dominated by emission from cooler material at larger radii. We also know from the shape of the silicate emission profiles that essentially all the dust grains we see are optically thin (internally, that is), and composed of amorphous and crystalline silicates (see, e.g., Sargent et al. (2009)). In this case EW(10μm) does not depend upon mass fractions of amorphous and crystalline material. One way to see this is to note that a grain with a given number N of silicate monomers has a fixed number of oscillators, with possibly a small range of oscillation frequency, in any given vibrational mode. Absorption or emission integrated over that mode is, to first order, proportional to N. (This is essentially the Thomas-Kuhn sum rule.) Thus two grains with the same N but different mineral fractions have the same equivalent width in the same vibrational mode – such as that which produces the 10 μm silicate feature – though the one with larger mineral fraction will have a larger number of oscillators at a small set of fixed frequencies, and identifiable sub-structure to the silicate feature.

In Figure 6 we plot n_{13-31} vs. n_{K-6} and n_{13-31} vs. $EW(10\mu\mathrm{m})$ for objects in Orion A. We also added objects in Tau (Furlan et al. 2011) in the plots for comparison.

To identify TDs in Orion A, we first selected objects satisfying one of the above conditions as possible candidates. Second, we rejected objects with spectral types earlier than G because they have significantly higher masses ($> 2\ M_{\odot}$) and their circumstellar disks evolve much faster by possibly different disk clearing mechanisms than the case of transitional disks around the low-mass T Tauri stars. However, we keep objects with unknown spectral type as all appear to lie in the same luminosity range as the low-mass T Tauri stars. Third, we examined the detailed shape of the SEDs, and selected objects with deficits of infrared excess in the 2-8 micron range, compared to the appropriate median IRS spectrum of Class II disks in Tau (Furlan et al. 2011). We used the median of Taurus K5-M2 for objects with the spectral type earlier than M3, and the median of Taurus M3-M5 for objects with the spectral type of M3 or later. We adopt the Taurus median spectra instead of Orion A median because transitional disks in Tau and the median SED of Class II disks in Tau have been well studied and used widely for comparison in studies of other star-forming regions. As shown in Figure 7, the previously characterized TDs in Tau, Cha I, Oph, and N1333 pass these filters clearly.

In Table 5, we indicate how the TDs in this paper were selected based on the selection criteria. Three objects, OriA-44, OriA-88, and OriA-172, are classified as TDs based upon examination of their SEDs which are indicative of gap/central hole, despite the fact that they do not pass any of the three criteria. The spectra of 62 transitional disks in Orion A appear in Figure 2. We use these 62 TDs in Orion A and 43 TDs from Tau (13), Cha I (11), Oph (10), and NGC 1333 (9) to unveil properties of transitional disks in the following.

4.1.1. Subclassification of Transitional Disks: CTD, WTD, and PTD

The mid-infrared spectrum of a CTD like DM Tau and CoKu Tau/4, having a few-AU to few-tens of AU central clearing, is distinctive compared to a radially-continuous Class II disk: it shows very little continuum excess over the photosphere from near-IR (1-2 μm) to wavelengths in the mid-infrared (around 8-13 μm), at which point the excess increases exponentially with increasing wavelength until it matches or exceeds the median spectrum. The other two types of TDs have excesses from near-IR to the shorter mid-infrared wavelengths ($\sim$5-8 μm) that are smaller than or similar to the median. In some, like LkCa 15 and UX Tau A, veiling in the near IR spectra points to an underlying optically thick inner disk (Espaillat et al. 2007b, 2008), and their distinctive spectrum corresponds to optically thick inner and outer disks separated by a gap. These are PTDs. Intermediate

between CTDs and PTDs are WTDs, in which the weaker near- and mid-infrared excess is best explained by an optically-thin inner disk separated by a gap from an optically-thick outer disk, as in GM Aur (Calvet et al. 2005; Espaillat et al. 2010). Therefore, the distinction between CTDs, WTDs, and PTDs is whether an (optically thick/thin) inner disk exists or not.

It is useful to define the Inner Disk Excess Fraction (*IDEF*) to characterize the near-infrared and shorter-wavelength mid-infrared excess fraction relative to the K5-M2 median spectrum of Class II sources in Tau. Since our sample is complete in H band data from the 2MASS catalog and we have IRS spectra starting at ∼5.2 μm, we interpolate H band to 6 μm to acquire the assumed spectrum covering 1.65-6 μm:

$$IDEF = \frac{\int_{1.65\mu\mathrm{m}}^{6\mu\mathrm{m}} F_{\lambda,obj} - F_{\lambda,photosphere}\, d\lambda}{\int_{1.65\mu\mathrm{m}}^{6\mu\mathrm{m}} F_{\lambda,median} - F_{\lambda,photosphere}\, d\lambda} \tag{8}$$

In the case of OriA-88 for which we do not have an SL2 spectrum, the flux at IRAC channel 3 (5.8 μm) is used instead of IRS fluxes.

By taking the already well studied Taurus TDs as references, we adopt a set of infrared-excess ranges to subclassify TDs:

CTD: $IDEF < 0.25$
WTD: $0.25 \leq IDEF < 0.5$
PTD: $IDEF \geq 0.5$

The *IDEF* values for the TD subclassification criteria are derived by adopting the K5-M2 median spectrum. The M3-M5 median spectrum is fainter than the K5-M2 median spectrum due to an effect of lower stellar luminosity and lower disk emission(Furlan et al. 2011). Therefore the excess emission over photosphere at 2-8 μm is weaker. It may lead to misclassification to compare objects of M3 or later spectral type to the K5-M2 median spectrum: an *IDEF* value of an object with M3 or later spectral type derived from the K5-M2 median spectrum is generally lower than that derived from the M3-M5 median spectrum. Furthermore, there are no WTDs and few PTDs with M3 or later spectral type among the already well studied TDs in Tau, Cha I, and Oph. Thus, for M3-M5 types, we rely on confirmation by other TD selection criteria. Considering the additional contributions such as the disk inclination and scattered light to the degeneracy of the interpretation of the excess emission in the near-infrared, we consider the subclassification of TDs based on *IDEF* as preliminary. We note the subclassification based on *IDEF* values and some cases of exceptions of using this criteria in Table 5.

With these criteria we obtain 34 CTDs, 15 WTDs and 13 PTDs in Orion A. Adding the four other nearby associations of Tau, ChaI, Oph, and N1333 brings the totals to 47 CTDs, 17 WTDs and 41 PTDs. Spectral indices of these objects are plotted in Figures 6 and 7.

Most CTDs are placed below the lower octile of n_{K-6}, which reflect their negligible short-wavelength infrared excess from the inner disk, while PTDs are distributed over the whole range greater than the lower octile of n_{K-6}. The WTDs are mostly located between the distribution of CTDs and PTDs in n_{K-6}.

In the plot of n_{13-31} vs. $EW(10\mu\mathrm{m})$ in Figure 6 and Figure 7, we also indicate the ranges occupied by radially-continuous disk models with a range of inclination angles, stellar masses, degrees of dust settling, and mass accretion rates (D'Alessio et al. 2006; Watson et al. 2009a; Espaillat 2009). Most of TDs in Orion A lie outside the model polygon. However, in contrast to the positions of TDs in other star-forming regions, some of CTDs, WTDs, and PTDs in Orion A are located inside the polygon, indicating that they could be modeled as radially-continuous disks, with respect *only* to these two parameters. With the exception of IRS-18 (PTD) and IRS-154 (WTD) in ONC, the transitional disks inside of the polygon are located in the region for vertically well-mixed disks (the area toward the upper right side in the polygon). Few objects lie in the domain of well-mixed disks for Tau, ChaI, Oph and N1333. Furlan et al. (2009) concluded from this that substantial disk structural evolution, especially settling of dust to the disk midplane, has occurred in 1-2 Myr. Arnold et al. (2012) showed that the disks in N1333 are statistically indistinguishable from those in Tau, Cha I and Oph in this regard.

In the ternary plot of Figure 8 we see the distribution of TDs are separated from the radially-continuous disks in the three dimensional parameter spaces of n_{K-6}, n_{13-31}, and $EW(10\mu\mathrm{m})$: especially CTDs and WTDs are nicely located in the different region from the region occupied by the radially-continuous disks.

We plot n_{13-31} and $EW(10\mu\mathrm{m})$ of disks in Orion A along IDEF in Figure 9, as well as TDs in Tau as the references of criteria along IDEF. We find that n_{13-31} of TDs decreases as IDEF increase, i.e., CTDs tend to have larger n_{13-31} than PTDs. We note that CTDs with low IDEF span through the ranges of $EW(10\mu\mathrm{m})$, whereas most PTDs have high values (>4) of $EW(10\mu\mathrm{m})$.

4.1.2. TD Selection Criteria in the Literature

We have compared our selection criteria for TDs to other selection criteria used in the literature. We plot TDs as well as Class II sources in OriA on the color-color diagrams

used for the selection criteria by Merín et al. (2010) (left panel), Cieza et al. (2010) (middle panel), and Muzerolle et al. (2010) (right panel) in Figure 10. These authors used *Spitzer* IRAC and MIPS broadband photometry, not IRS spectra, for their selection criteria.

Merín et al. (2010) identified and characterized disks with inner holes from the *Spitzer* c2d Legacy program. They used [3.6]-[8.0] vs. [8.0]-[24] color-color diagram to identify TDs that fell in two separate regions:

Region A: $0.0 <$ [3.6]-[8.0] < 1.1 and $3.2 <$ [8.0]-[24] < 5.3
Region B: $1.1 <$ [3.6]-[8.0] < 1.8 and $3.2 <$ [8.0]-[24] < 5.3

Region A selects TDs with central clearings like CTDs in our sample. Region B corresponds to the disks with some excess flux in the IRAC bands like WTDs and PTDs in our sample. Their selection criteria of region A agrees with our criteria for CTDs in L1641, but some number of CTDs in Orion A fall in Region B or outside the Region A and B (the left panel of Figure 10).

Cieza et al. (2010) set selection criteria based on the [3.6]-[24] vs. [3.6]-[4.5] color-color diagram, in which TDs are located in the region where [3.6]-[4.5] < 0.25 and [3.6]-[24] $>$ 2. We see that most of our CTDs fall in that region, but PTDs have [3.6]-[4.5] > 0.25 (the middle panel of Figure 10).

Muzerolle et al. (2010) used spectral slopes (i.e. spectral indices) at two different wavelength intervals, 3.6-5.8 μm and 8-24 μm. The criteria for the classical transitional disks with central holes based on a red α_{8-24} in Muzerolle et al. (2010) agrees with our criteria for CTDs. However, similar to Cieza et al. (2010), most of our WTDs and all of our PTDs will be missed by this criterion (the right panel of Figure 10).

From the comparisons of selection criteria for TDs, we find that (1) CTDs can be commonly identified by a variety of criteria; (2) a criterion utilizing the largest wavelength interval in the IRAC channels (between ch1 (3.6 μm) and ch4 (8 μm) in Merín et al. (2010)) can select WTDs and PTDs, but a color (i.e. the spectral slope) based on other broadband channels, such as [3.6]-[4.5] in Cieza et al. (2010) or 3.6-5.8 μm in Muzerolle et al. (2010), cannot find PTDs.

4.2. Radial Properties of Transitional Disks: R_{wall}

One of the most important properties of a transitional disk is how large the gap or hole is; that is, the radius at which the inner wall of the optically thick outer disk lies. Bearing in

mind the limitations of inference of structure from the SED, we derive the radius, R_{wall}, from the shape of the spectrum at the transition from small to large infrared excess within the IRS spectrum. Our procedure, illustrated in Figure 11, is the same as in our previous work (Kim et al. 2009): we model the inner edge of the outer disk as an optically thick insulating wall, with dust temperature T, as follows. We first subtract a power-law fit to the IRS spectrum in the 5-8 μm region to remove the flux from the photosphere or an excess from the inner disk. To the residuals, we fit a model with two components tightly constrained at 13-16 μm and 30-33 μm. One component is emission from optically-thin astronomical-silicate dust (Draine & Lee 1984) with 0.1 μm radius, to represent the inner disk and the bulk of the optically thin atmosphere of the outer disk. The other component is a single-temperature (T) blackbody that represents the insulated inner edge of the optically thick outer disk. As we described in Kim et al. (2009), we do not aim to fit the details of the spectrum perfectly, but merely to separate the optically-thick continuum — for which the SED shape is the signature of the wall — from the silicate emission features centered at 10 and 20 μm. With the temperature T, we calculate R_{wall} using radiative equilibrium at the inner wall:

$$R_{wall} = \sqrt{\frac{L_\star(1-A_\star)}{4\pi\sigma T^4 \epsilon_{IR}}} \left(\equiv \sqrt{\frac{L_\star}{4\pi\sigma T^4}} \right) \tag{9}$$

where $A_\star$ is the effective albedo at stellar wavelengths and ϵ_{IR} is the effective emissivity at mid-IR wavelengths. We adopt $(1-A_\star)/\epsilon_{IR} = 1$: a perfectly black wall.

We compared the resulting R_{wall} of several transitional disks in Tau (CoKu Tau/4; DM Tau; GM Aur; LkCa 15; UX TauA), Cha I (CR Cha; SZ Cha; T11; T25; T35; T56), and Oph (Rox 44, 16126-2235AB) with the same quantity determined from detailed self-consistent models (Espaillat et al. 2010, 2011). We found the derived R_{wall} from Equation (9) are within about 33% of those obtained from detailed models. We also compared our R_{wall} estimates to the cavity radius (R_{cav}) derived from the Submillimeter Array (SMA) observation for DM Tau, GM Aur, LkCa 15, UX Tau A, and ROX 44 (Andrews et al. 2011), and these results lie within 34% of each other. Comparison of R_{wall} from the detailed model and the R_{cav} observed by SMA also gives a similar range of difference, about 34%. Therefore, we adopt 33 % as the uncertainty of R_{wall} estimated from Equation (9). The R_{wall} results are listed in Table 4.

5. FREQUENCY AND AGE DISTRIBUTION

Most previous studies of transitional disks (e.g. Kim et al. 2009; Muzerolle et al. 2010; Merín et al. 2010; Currie & Sicilia-Aguilar 2011) and protoplanetary disks (Furlan et al.

2009; Luhman et al. 2010; Manoj 2010) have estimated the fractions of transitional disks to infer when the transition occurs and how long the transition stage persists. We take the fraction of CTDs+WTDs to compare to the Muzerolle's CTDs because the qualitative definition of the classical transitional disks in Muzerolle et al. (2010) is most nearly equivalent to the definition of the combined set of CTDs and WTDs in our sample. We note that the quantitative selection criteria used by Muzerolle et al. (2010) missed some WTDs as discussed in §4.1.2

The fraction of TDs in this work is defined as n(TD type)/n(disks) using the number of TDs and number of Class II sources identified from the IRS survey of each region (see, Table 6). We exclude samples in Ophiuchus for the frequency and age trend search even though it is listed in Table 6 because the selected TDs are from several sub-regions of Ophiuchus with differing estimated ages, and the sample sizes are too small to separate by subregion with high statistical significance.

The TD fraction is plotted as a function of age in Figure 12. We note that (1) the fraction of CTDs+WTDs can be high over the broad age ranges (1-10 Myr) and (2) the fraction of TDs varies from region to region at young ages ($<$ 3 Myr), with some having a fraction of only a few % while others have fractions of >20 % even at age $\leq$ 1 Myr.

Also shown in Figure 12 are the fractions of transitional disks of each type from this work only: CTD (square), WTD (circle), PTD (star), and the total of them (cross). If we consider the fraction of TDs including all CTD, WTD, and PTD, the fractions of all TDs in each region are significantly high even at very young ages of less than 1 Myr: 17±6% for N1333, 25±4% for ONC, and 26±5% for L1641 versus the TD fractions for the 2-3 Myr old associations: 8±2% for Tau and 16±5% for Cha I.

6. DISTRIBUTION AND TRENDS OF PROPERTIES

6.1. Transitional Disk Types *vs.* Spectral Type, R_{wall}, and $\dot{M}$

In this section, we examine how the distributions of host star spectral types, R_{wall}, and $\dot{M}$ compare for transitional disks with different inner disk structures: CTD, WTD and PTD types. In this analysis we exclude the TDs for which we do not have reliable host-star spectral types.

In Figure 13, we show the spectral type distribution for all TDs and for each subtype. The median spectral type differs slightly among the TD subtypes: M2 for CTDs; M1 for WTDs; K7 for PTDs; M0 for WTD+PTD; M1 for TDs. The spectral type distributions of

CTDs and PTDs differ noticeably, even if we consider the general spectral type uncertainty of one to two subtypes. However, a Kolmogorov-Smirnov (K-S) test shows that the spectral type difference between CTDs and PTDs is of marginal statistical significant: for CTDs vs. PTDs, $D = 0.31$ and $p = 0.037$; where D is the maximum deviation between the cumulative distribution of two groups and p indicates the probability that there is no significant difference between the distributions.

In Figure 14, we show the frequency distribution of R_{wall} for each TD subtype. For almost 90% of TDs R_{wall} is less than 30 AU. This pattern is similar whether the inner disk exists or there is an empty inner cavity. However, we see that the median R_{wall} is smaller for CTDs than WTDs and PTDs. Most CTDs have $R_{wall} < 10$ AU (about 52 %), whereas 71 % of WTDs and PTDs with inner disks have $R_{wall} > 10$ AU. A K-S test that compares the R_{wall} distributions of CTDs and PTDs yields values similar to those for the comparison of the spectral type distributions: $D = 0.29$ and $p = 0.05$, which is not very significant. The p value decreases to 0.02 when comparing CTDs and WTDs+PTDs. The difference in the R_{wall} distributions of the TD subtypes could also be due to the impossibility of distinguishing PTDs with very small gaps from radially continuous disks based on the IR spectrum alone. Overall, Figure 14 shows that the IRS spectra are most sensitive to disk holes with $R_{wall} <$ 30 AU.

In Figure 15 we plot the $\dot{M}$ distribution for all TDs and broken down by subtype. TDs with central clearings (CTDs) and gapped disks (WTDs and PTDs) differ significantly in $\dot{M}$. Both groups also have $\dot{M}$ substantially smaller than the typical $\dot{M}$ of radially-continuous disks. The median $\dot{M}$ of the gapped disks is $10^{-8.25} M_{\odot}/yr$ and that of CTDs is $10^{-8.7}$ $M_{\odot}/yr$. This visible difference is confirmed by statistical analysis with the K-S tests. When we include the upper limits, the K-S test results $D = 0.46$ and $p = 0.001$. Even when we do not include the upper limits, the statistical significant difference between the two groups is still valid with $D = 0.5$ and $p = 0.002$. Thus we confirm that the $\dot{M}$s of CTDs are smaller on average than those of WTDs and PTDs.

For fair comparison of the $\dot{M}$ of radially-continuous disks and TDs, we need to be sure that these two groups have similar ages and stellar masses because $\dot{M}$ decreases with age (Hartmann et al. 1998) and increases with $M_{\odot}$ (Muzerolle et al. 2003; Calvet et al. 2004). Because systematic differences of stellar masses and ages can arise from a choice of different evolutionary tracks (e.g. Simon et al. 2000; Najita et al. 2007), the best would be to have $\dot{M}$ estimated with the same method and assumptions used for $\dot{M}$ estimation of TDs. However, there is currently no such $\dot{M}$ survey of low-mass T Tauri stars. A comparison between $\dot{M}$ of Orion A TDs and other radially-continuous Class II disks measured in an homogeneous method will be discussed by Kim et al. (2013, in preparation).

Therefore, for the next best comparison, we use the $\dot{M}$ measurements of T Tauri stars in Taurus by Gullbring et al. (1998) for the following reasons. Gullbring et al. (1998) adopted the evolutionary tracks of D'Antona & Mazzitelli (1997), which tends to result in younger stellar ages and lower stellar masses. Simon et al. (2000) found both the Baraffe et al. (1998) model and Siess et al. (2000) model agree with dynamical masses in the 0.7-1 $M_{\odot}$ range, while D'Antona & Mazzitelli (1997) do not agree as precisely. Even though White & Ghez (2001) measured $\dot{M}$ of T Tauri stars in Taurus as adopting an evolutionary track combined Baraffe et al. (1998) and Palla & Stahler (1999), the samples are binary systems and $\dot{M}$ of binary system is not comparable to $\dot{M}$ of TDs. Hence, we adopt the median $\dot{M}$ from Gullbring et al. (1998) as the median $\dot{M}$ of radially-continuous disks in Taurus, $\dot{M} = 10^{-7.8} M_{\odot}/yr$.[6] While bearing in mind the possible uncertainties (∼30%) of stellar masses between two different evolutionary tracks, we confirm that the ages and stellar masses of the Gullbring et al. (1998) sample are similar to those of TDs studied in this work. Thus our results confirm that TDs in general have substantially smaller $\dot{M}$ than radially-continuous disks, in accord with the findings by Najita et al. (2007), Kim et al. (2009), and Espaillat et al. (2012).

6.2. Trends among TD Properties

Understanding the correlations between disk and stellar properties of TDs is an essential and important key to understand how protoplanetary disks evolve from radially-continuous optically thick disks to a final planetary system. We have gathered the largest sample of TDs which are identified by homogeneous criteria. From this large sample, we are able to find not only trends of TDs in general but also detailed trends of the three different types of TDs.

Except for $\dot{M}$, we estimate the stellar/disk properties of TDs in Tau, ChaI, Oph and N1333 in the same ways as for Orion A TDs. The $\dot{M}$ of TDs of other star-forming regions are from literature or personal communication. Adopting $\dot{M}$ measured by different techniques from that for the TDs of OriA should not affect significantly these trends, based on the demonstration of the tight correlation between the luminosities of IR hydrogen recombination lines and L_{acc} measured from the blue excess spectrometry and/or U-band photometry by Muzerolle et al. (1998). Therefore, we expect that any discrepancies in luminosity between the two (IR and UV) data sets on average will be small (Muzerolle et al. 1998). These

[6]We excluded three TDs, GK Tau, GM Aur, and IP Tau, in the sample of Gullbring et al. (1998) to measure the median $\dot{M}$ of radially-continuous disks in Taurus. If we include those three TDs, the median Mdot decreases to $\dot{M} = 10^{8} M_{\odot}/yr$.

stellar/disk properties and other properties obtained from the literature are also listed in Table 4.

Among trends from many possible combinations of properties, we present the trends of interesting pairs of properties showing somewhat different behaviors from non-transitional disks in Figure 16 through Figure 21. The correlation parameters are calculated by using *linmix_err.pro* which was developed for the Bayesian approach to linear regression with errors in both X and Y, by Kelly (2007), and the trends line in each plot can be read in the manner of $\log_{10}(Y) = (\alpha \pm e\_\alpha) + (\beta \pm e\_\beta)\log_{10}(X)$. We indicate the correlation parameters (*corr*) and probabilities (P) of pairs of properties in Table 7 for TDs without separation by subtype and in Table 8 for two subgroups of TDs separated by their radial disk structures, i.e., CTDs and WTPs+PTDs. In general, a 5% or lower P value is considered to be statistically significant. Sometimes $P \lesssim 2\%$ is considered as a conservative threshold of statistically significant. Therefore, we interpret a correlation to be a statistically significant with $P \lesssim 2\%$ and to be a marginally significant if P is 2-5%.

6.2.1. Trends of TDs

Our search for trends related to $\dot{M}$ utilized weighted linear regression to account properly for upper limits of $\dot{M}$ in our samples. The resulting trend for $\dot{M}$-$M_\star$ in Figure 16-(a) is $\dot{M} \propto {M_\star}^{1.6\pm0.3}$. To compare this to the $\dot{M}$-$M_\star$ relations from the previous studies ($\dot{M} \propto {M_\star}^{1.95}$ (Calvet et al. 2004); $\dot{M} \propto {M_\star}^{2.0}$ (Muzerolle et al. 2003); $\dot{M} \propto {M_\star}^{2.1}$ (Muzerolle et al. 2005)), we include in Figure 16-(a) a plot of the result, $\log \dot{M} \approx 2 \log M_\star - 7.5$ (Muzerolle et al. 2003; Telleschi et al. 2007). The slope of the $\dot{M}$-$M_\star$ relation of TD host stars is roughly consistent with previous studies among T Tauri stars, but the trend line for $\dot{M}$ is shifted downward by factor of about 10 with respect to the thick dashed line representing T Tauri stars in Taurus, consistent with the results discussed in Section 6.1.

In Figure 16-(b), we plot L_X as a function of $M_\star$. Compared to the results in Taurus $\log L_X = 1.69 \log M_\star + 30.33$ (Telleschi et al. 2007), the regression of our TD data is $\log L_X = 1.1 \log M_\star + 30.1$: slightly smaller slope than that of T Tauri stars.

Figure 16-(c) shows $\dot{M}$ as a function of L_X compared to the Taurus results derived from Taurus's $\dot{M}$-$M_\star$ and L_X-$M_\star$, $\dot{M}$-L_X relation for T Tauri stars $\log \dot{M} = 1.2 \log L_X - 43$. The $\dot{M}$-L_X trend line for our TD sample, $\log \dot{M} = 0.2 \log L_X - 14.6$. This shows that TD's $\dot{M}$ is not related to L_X, unlike CTTSs.

The most interesting relations are the correlation of R_{wall} to stellar properties. In Figure 17-(a), we find a very strong correlation between $M_\star$ and R_{wall}. For both cases of $\dot{M}$ and

L_X, we also see the increasing trends of $\dot{M}$-R_{wall} in Figure 17-(b) and L_X-R_{wall} in Figure 17-(c). However, we should recall that there is a tight correlation of $M_\star$-R_{wall} and a statistically significant correlation of $\dot{M}$-$M_\star$. Therefore, the correlation showing in the plots of $\dot{M}$-R_{wall} may merely reflect the combination of correlations between $M_\star$-R_{wall} and $\dot{M}$-$M_\star$. To test this hypothesis, we looked for a trend between $\dot{M}$ and R_{wall} in more restricted mass bins (e.g., 0.2-0.4 $M_\odot$, 0.4-0.7 $M_\odot$, and 0.7-2.3 $M_\odot$) and did not find significant trends. Similarly, the increasing trend of L_X-R_{wall} may be the result of combination of the correlations between L_X-$M_\star$ and $M_\star$-R_{wall}.

For further examination of the difference between $\dot{M}$-R_{wall} relationship of TDs and that of CTTSs under the strong dependence on $M_\star$, we derived an expected $\dot{M}(M_\star)$-R_{wall} of CTTSs by combining the $\dot{M}$-$M_\star$ of CTTSs ($\log \dot{M} = 2 \log M_\star - 7.5$) and a strong $M_\star$-R_{wall} correlation of TDs ($\log M_\star = 0.7 \log R_{wall} - 1.0$): $\log \dot{M}(M_\star) = 1.4 \log R_{wall} - 9.5$ (Figure 17-(b)). The expected $L_X(M_\star)$-R_{wall} of CTTSs considering the $M_\star$ dependence is also derived by combining L_X-$M_\star$ of CTTSs and $M_\star$-R_{wall}: $\log L_X(M_\star) = 1.2 \log R_{wall} - 28.6$ (Figure 17-(c)). We find that the trends of TDs in $\dot{M}$-R_{wall} and L_X-R_{wall} generally agree with the trends of CTTSs.

Several other interesting correlations for TDs are listed in Table 7. The very strong correlation of $L_\star \sim {M_\star}^{1.6}$ which is similar to that ($L_\star \sim {M_\star}^{1.5}$) found from T Tauri stars in Tau by Telleschi et al. (2007) supports that the basic stellar properties, $M_\star$ and $L_\star$, of TDs are not very different from the stars hosting radially-continuous flared disks and/or homologously evolved disks.

6.2.2. Trends of $\dot{M}$ and L_X for Transitional Disk Subtypes

In this section we explore characteristics of $\dot{M}$ and L_X, which are sensitive to the different inner disk structures and to the different disk evolution mechanisms, by searching for detailed trends of sub-samples grouped by different TD types. The correlation parameters of the detailed trend analysis for the case of inner clearings (CTDs) and the case of radial gaps (WTDs+PTDs) are listed in Table 8.

It is clear that the trend between $\dot{M}$ and $M_\star$ of CTDs is different from that of WTDs+PTDs from the left panels ((a) and (b)) of Figure 18. When the inner disk is essentially empty as for the CTDs, no correlation exists between $\dot{M}$ and $M_\star$. However, for the case of WTDs+PTDs, $\dot{M}$ and $M_\star$ are significantly correlated each other, and the relation ($\dot{M} \propto {M_\star}^{1.9}$) is very close to that of CTTS ($\dot{M} \propto {M_\star}^2$). Therefore, the increasing tendency shown in Figure 16 probably leads to a strong effect from the significant correlation of $\dot{M}$ and $M_\star$ for WTDs+PTDs

which still have an inner disk in their disk. In contrast to $\dot{M}$, we find no significant difference between the two subgroups of TDs for the L_X-$M_\star$ correlation (the right panels ((c) and (d)) of Figure 18).

Similar to the left panels of Figure 18, in the left panels of Figure 19, we also see no correlation of $\dot{M}$-R_{wall} for CTDs but a significant and strong correlation for WTDs+PTDs. To find the genuine behavior of TDs between $\dot{M}$ and R_{wall} which is different from $\dot{M}$ of CTTSs, we divided $\dot{M}$ of our sample by the $\dot{M}(M_\star)$ (the thick long-dashed lines). The right panels of Figure 19 show the residual relation between $\dot{M}$ and R_{wall} of CTDs ((c); anti-correlation) and WTDs+PTDs ((d); no correlation) after taking the dominant effect of $M_\star$ out. This supports the ideas that (1) the mass accretion behaves similarly to the case of radially-continuous disks while an inner disk exists in a TD, and (2) the mass accretion rate decreases as the size of inner cavity increases.

In the left panels of Figure 20, CTDs have a very strong and significant correlation between L_X and R_{wall}, while WTDs+PTDs have a weak relationship with large uncertainty in the trend of L_X and R_{wall} comparing to that for all TDs combined. Therefore, we infer that the general increasing tendency of L_X along R_{wall} in Figure 17 is due to the dominant effect of the strong correlation for CTDs. After removing the underlying contribution from $M_\star$ to L_X-R_{wall} relation by dividing L_X-R_{wall} by $L_X(M_\star)$-R_{wall}, we see no correlation for CTDs and insignificant anti-correlation with large uncertainty for WTDs+PTDs from the right panel of Figure 20.

From Figure 21, we confirm that $\dot{M}$ and L_X are not correlated with each other regardless of subtypes of TDs not like the strong correlation between them in case of T Tauri stars (the thick dashed line in the (a) and (b) panels). The residual $\dot{M}$ after removing the strong $\dot{M}$-L_X correlation of T Tauri stars in the right panels are anti-correlated to L_X for both CTDs and WTDs+PTDs. We note that this is a similar to the trend found for CTTSs by Telleschi et al. (2007). Drake et al. (2009) also shows the similar result that the objects with higher L_X have lower $\dot{M}$ and find a strong anti-correlation between L_X normalized to $M_\star$ and $\dot{M}$ with CTTS/WTTS in ONC. Therefore, the anti-correlation shown in the right panels of Figure 21 for both CTDs (c) and WTDs+PTDs (d) may be a common characteristic of protoplanetary disks, not a unique characteristic of TDs.

6.3. Summary of Significant Trends

Here, we summarize the correlations and trends of TD properties we find to help our insights on the origin of TDs, which will be discussed through the next section.

$L_\star$ and $M_\star$ are independent of the subtypes of transitional disks. The significantly strong correlation between $M_\star$ and R_{wall} is consistent regardless of the subtype of TDs as $M_\star \propto R_{wall}$.

$\dot{M}$ and L_X vary/evolve with time. We have seen that some trends differ by subtypes of TDs and some trends are comparable to those of the larger T Tauri star population overall. The residual (or normalized) properties after removing the underlying effect of $M_\star$ which is a parameter correlated with $\dot{M}$ and L_X may show the effect of the transition process from a radially continuous disk to a transitional disk.

Some properties have very different trends according to whether the inner disk exists (WTD/PTD) or not (CTD).

(1) Trends related to $\dot{M}$ show a strong correlation with WTDs+PTDs, but no correlation with CTDs:
• $\dot{M}$ vs. $M_\star$: WTDs+PTDs show a very similar correlation to that of T Tauri stars with $\dot{M} \propto {M_\star}^{1.9}$. In stark contrast, no correlation shows for CTDs.
• $\dot{M}$ vs. R_{wall}: WTDs+PTDs show a very tight correlation between the two properties, $\dot{M} \propto {R_{wall}}^{1.9}$, but the two properties are not correlated for CTDs.

(2) Trends of some properties are strongly correlated for CTDs, but not for WTDs+PTDs:
• L_X vs. $M_\star$: The trend of CTDs ($L_X \propto {M_\star}^{1.8}$) alone is very close to the trend of T Tauri stars ($L_X \propto {M_\star}^{1.7}$), but the slope ($\beta$) of the trends of WTDs+PTDs is smaller by about a factor of two ($L_X \propto M_\star$).
• L_X vs. R_{wall}: A significant correlation between L_X and R_{wall} for CTDs, but the trend for WTDs+PTDs is very uncertain.
• *residual* $\dot{M}$ vs. R_{wall}: The residual trend of $\dot{M}$ and R_{wall} is opposite to the trend before removing $M_\star$ effect from $\dot{M}$ vs. R_{wall}: CTDs show an anti-correlation, but WTDs+PTDs do not show any correlation.

On the other hand, $\dot{M}$ vs. L_X show no correlations from any subtype of TDs, in contrast to the strong correlation for T Tauri stars with full disks.

7. MECHANISMS FOR THE ORIGINS OF TRANSITIONAL DISKS AND CONSTRAINTS

In this section, we briefly review proposed mechanisms for disk dispersal and compare how our findings are consistent, or not, with these predictions from the mechanisms: dust coagulation and settling; photoevaporation; inside-out disk clearing by MRI; gravitational effects of one or more low-mass companions.

Grain growth and settling. Dust grains should grow and settle to the disk midplane during the protoplanetary disk evolution process. As grains grow larger, the opacity of the grains becomes smaller, leading to weaker continuum emission in IR range. On this basis, it has been proposed that the flux deficit shown in SEDs of TDs may be due to the existence of an opacity hole caused by grain growth and settling in the inner disk rather than a real material deficit in the inner disk (e.g. Dullemond & Dominik 2005). Tanaka et al. (2005) suggested that the SEDs of TDs could be due to differing opacity as a function of radius; e.g., smaller disk optical depth in the inner disk than in the outer disk at 10 μm. Some authors (Garaud 2007; Brauer et al. 2007, 2008) have demonstrated the short time scale of grain growth and settling. However, considering grain growth/settling only as the main mechanism of TDs cannot explain the sharp transition represented by the sharp edge of the inner wall of the outer disk which is implied from the distinctive characterstic of TD's SEDs and is supported by many resolved submillimeter images of TDs (Hughes et al. 2009; Andrews et al. 2011).In any case, grain coagulation and settling is a process that takes monotonically longer at increasing radius within the disk, so it cannot possibly explain the gaps in WTDs and PTDs.

MRI. A mechanism important in the large scale mixing and turbulence in a disk is the Magnetorotational Instability (MRI). Chiang & Murray-Clay (2007) showed how MRI accelerates mass accretion and leads to inside-out disk clearing. Perez-Becker & Chiang (2011) considered the ionization, necessary for the MRI mechanism, by stellar FUV radiation and demonstrated that the surface layer accretion driven by this could reproduce the trend of increasing accretion rate with increasing hole size seen in TDs. Suzuki et al. (2010), using MHD simulations with X-rays as the ionization source, showed the disk winds driven by MRI leads to a decrease in surface density in the manner of inside-out dispersal irrespective of the existence of a deadzone.

These models based on the inside-out disk clearing by MRI draining predict correlations between R_{wall}, $\dot{M}$, and L_X: (1) a positive correlation between $\dot{M}$ and R_{wall} at a given $M_\star$ because a larger ionized area leads to more mass accretion; (2) a positive correlation between $\dot{M}$ and L_X at a constant R_{wall} because more ionization of disk surface as exposed by stronger energy sources leads to more mass accretion. However, our findings on the trends of $\dot{M}$, L_X,

and R_{wall} do not support these predicted correlations between R_{wall}, $\dot{M}$, and L_X. First, a strong correlation of $\dot{M}$ with R_{wall} is shown only for the case of TDs with radial gaps (WTDs+PTDs) not for the TDs with inner cavities (CTDs). Furthermore, that correlation disappears when differing stellar masses are accounted for. Second, we found no correlation between $\dot{M}$ and L_X for TDs regardless of their subtypes. To test for correlation between $\dot{M}$ and L_X at a given R_{wall}, we examine trends for several different R_{wall} ranges in Figure 22. We find no correlation between $\dot{M}$ and L_X for any ranges of R_{wall}.

Photoevaporation. Photoevaporation has long been thought to be an important and major disk dispersal mechanism (Shu et al. 1994; Hollenbach et al. 1994; Clarke et al. 2001; Font et al. 2004; Alexander et al. 2006a,b). High energy radiation from the central star ionizes and heats the disk surface, which can be unbound and leaves as a wind beyond a certain radius. A gap can be opened when the accretion rate is small enough that material from the outer disk beyond the photoevaporation radius cannot replenish the inner disk. The inner disk, decoupled from the outer disk, drains on to the central star while the outer disk is evaporated into space. These models encounter contradictions when only the EUV ionizing radiation is considered: (1) the mass accretion rates of TDs is higher than the photoevaporation rate (or mass loss rate), (2) the ages of many TDs are less than the dispersal time scale of photoevaporation, and (3) the existence of the large radial gaps of PTDs. Recently, the photoevaporation model has been modified to address those issues by taking much higher energy radiation sources (FUV and X-ray) as sources (Ercolano et al. 2009; Gorti & Hollenbach 2009; Owen et al. 2010, 2011a,b, 2012): (1) much higher mass loss rate can be driven by X-rays (Ercolano et al. 2009); (2) 1-10 AU gap creation at relatively early epochs (3-4 Myr) (Gorti et al. 2009). Considering disk dispersal by photoevaporation through EUV, FUV, and X-ray radiation, Owen et al. (2012) concluded that the stars' intrinsic X-ray luminosity should have a decisive role in disk's life times and evolution.

We compare our data to the theoretical predictions from the X-ray photoevaporation (XPE) model by Owen et al. (2012). Both the TD data and the XPE model have tendencies of increasing R_{wall} and $\dot{M}$ as L_X and $M_\odot$ increase. However, most TDs of all three types in our sample do not fall into the model domains, as indicated in Figure 23[7] and Figure 24. In particular, the XPE model fails to explain the objects with either large R_{wall} or the large $\dot{M}$. More than half of all TDs fall outside the region allowed by the XPE in Figure 24. Therefore, we conclude that X-ray photoevaporation is not the dominant mechanism for creating transitional disks.

[7]Owen et al. (2012) note the difficulty of determining a correlation between any two of the three properties because L_X, R_{wall}, and $M_\star$ are interdependent. Therefore, the predictions in the Figures are the results from numerical simulation.

Morishima (2012) developed a gas disk model taking into account layered accretion driven by MRI and X-ray photoevaporative winds. With a central star of 1 $M_{\odot}$ and an initial disk mass of 0.1 $M_{\odot}$, they found their gas dispersal model can open a gap at large radii while the mass accretion rate is still similar to that of CTTS when dead zones are considered. They show that their model with a dead zone can reconstruct the distribution of the observed transitional disks with high $\dot{M}$ and large R_{wall}, which is the range X-ray photoevaporation cannot reconstruct.

The average disk mass of Class II objects measured by observations of the submm-mm continuum of disks (Andrews & Williams (2005); Andrews & Williams (2007)) in Tau and Oph is about 5 M_J. This is much less than the minimum mass solar nebular (MMSN) and the requirement of disk mass to form giant gas planets or multiple planets which are observationally confirmed. It seems likely that submillimeter continuum observations systematically underestimate disk masses (e.g. D'Alessio et al. (2001), Hartmann et al. (2006)). Alternatively, systems could have more substantial disk mass at the Class 0/I stage (Greaves & Rice 2010).

Gravitational effects of companions. If the disks start with larger masses, photoevaporative gas dispersal models may encounter another challenge to deplete disk material because more massive disks requires stronger energy sources to evaporate disk material. On the other hand, for a more massive disk, the more favorable mechanism to open and clear a gap in a protoplanetary disk is giant planet formation by gravitational instability. Recent theoretical results on planet formation by gravitational instability suggest the possibility of gas giant planet formation at even much closer distances to the central star (10 AU by Inutsuka et al. (2010); R $<$ 25 AU by Meru & Bate (2010)). Even giant planet formation *via* core accretion model, which requires longer time scales, is possible in $\sim$1 Myr with disks substantially larger than the MMSN (Dodson-Robinson et al. 2009; Greaves & Rice 2010).

Giant planet formation in protoplanetary disks has been proposed as the origin of gaps/holes of TDs and debris disks (e.g. Holland et al. 1998; Jura & Turner 1998; Zuckerman & Song 2004). Several hydrodynamical simulations show the companion's presence can reproduce the sharp inner disk truncation and gap formation in a short time scale (Quillen et al. 2004; Rice et al. 2006; Varnière et al. 2006; Zhu et al. 2011, 2012).

Whether the companion is a planetary object or a sub-stellar companion, the observational features can be explained by the dynamical effects of the companion on the central star. The distribution of $\dot{M}$ shown in Figure 15 strongly supports the idea of gap opening and disk dispersal by planet/companion formation. The displacements of $\dot{M}$ of the gapped disks and the CTDs from the median $\dot{M}$ of CTTS is almost a factor of 10, which is consistent with the estimated decrements of the mass flow across a gap created by a low-mass

companion (Lubow & D'Angelo 2006). As we discussed in Kim et al. (2009), the strong correlation between $L_\star$ or $M_\star$ vs. R_{wall} is reminiscent of the observed dependence between binary separation and the system's stellar mass. While this similarity might be taken to suggest that the stellar mass vs. separation dependence is imprinted when stars form, this argument has an important caveat. The strong trend of $M_\star$-R_{wall} of TDs is possibly driven by strong correlations of $L_\star$-$M_\star$ and $L_\star$-R_{wall}. More detailed studies are needed to investigate this possibility.

Giant planet formation can also explain the trends shown in $\dot{M}/\dot{M}(M_\star)$-R_{wall} (Figure 19). Assuming (1) $M_{disk} \propto M_\star$ at a given age which implies (2) normalization by $M_\star$ is the same as normalization by M_{disk}, the mass accretion rates of WTDs+PTDs may not be strongly related to R_{wall} since material accreting from an inner disk may not be dependent on a planet formation location or R_{wall} and the mass accretion from an inner disk may be dominant than mass accretion through a gap from an outer disk. In the case of CTDs when the inner disk is depleted, however, the outer disk mass will decrease as the size of an inner cavity increases. That will result less material to accrete through the larger inner hole, therefore the anti-correlation between $\dot{M}/\dot{M}(M_\star)$ and R_{wall} of CTDs is naturally explained.

The disk-clearing companion can be a stellar companion such as the case of CoKu Tau 4 (Ireland & Kraus 2008) because a large fraction of stars form in multiple systems. If a stellar companions are the dominant origin of TDs, they should be of lower mass than the primary to explain the strong correlations in $\dot{M}$-$M_\star$ of WTD+PTD. Sensitive searches have been made for 10 AU-scale binaries in Taurus (Pott et al. (2010), Kraus et al. (2011)), but only one (CoKu Tau/4; Ireland & Kraus (2008)) of the nine transitional disk systems so studied has a stellar companion been detected with binary separation similar to the gap radius. The limits on companion luminosity for the other eight rule out stars. In addition, Kraus & Ireland (2012) have tentatively detected an infant giant planet in the gap of the LkCa 15 disk. Therefore, planet formation could possibly be chiefly responsible for the origin of TDs.

Currently it is not clear that how different paths of disk evolution are followed, and which mechanisms dominate on a track of evolution given different initial conditions. We do not deny the contribution to the dispersal of disk material and disk evolution from other mechanisms such as grain growth, MRI action in the inner disk, and photoevaporation. In other types of evolved disks, such as the anemic, homologously depleted, and weak excess disks, which are not covered in this study, grain growth and photoevaporation could be dominant mechanisms. However, we find that giant planet formation is probably the dominant mechanism in gap formation for our sample of TDs, based on the trends reported here.

8. Summary and Conclusions

We presented the SEDs of 62 new TDs identified from IRS spectra in the Orion A star-forming region and discussed selection criteria for TDs. Utilizing the TDs already identified in Taurus, Chamaeleon I, Ophiuchus, and NGC 1333, in a manner similar to TDs in Orion A, we explored statistically robust trends with the largest and most homogeneous set of TDs to date.

We presented a set of TD selection criteria and a quantitative empirical method to classify three subtypes of TDs: CTD, WTD, and PTD.

We found the TD fraction of Class II YSOs is very high ($\sim$20%) even at the youngest ages ($\leq$ 1 Myr, Orion A and NGC 1333). This could indicate early disk evolution even in the Class 0/I stages, most likely due to giant planet formation (Lubow & D'Angelo 2006).

We have examined various mechanisms of disk clearing utilizing our observation of TDs. We confirm that disk clearing mechanisms including MRI action and photoevaporation generated by X-ray/FUV photons are consistent with some of the observations, but not all. In particular, there are several observational trends which cannot be explained by these mechanisms, especially those related to $\dot{M}$ and L_X:
(1) the observed mass accretion rate suppression of CTD's ($10^{-8.7}$ $M_\odot/yr$) and PTD's ($10^{-8.25}$ $M_\odot/yr$) compared to the radially continuous disks ($10^{-7.8}$ $M_\odot/yr$);
(2) the lack (or negative) correlation between $\dot{M}$ and R_{wall} after accounting for $M_\star$'s effects
(3) no correlation of L_X and R_{wall} after correcting for $M_\star$'s effects
(4) no correlation of L_X and $\dot{M}$ at constant R_{wall}.
However, these properties/trends are naturally explained by substellar companions, formed within the disks in the early stages of disk evolution. Infant jovian-mass planets would nicely explain the size and structure observed for the gaps (Quillen et al. (2004); Edgar et al. (2007)).

Based on our results from the largest sample of transitional disks to date, as summarized above, we conclude that giant planet formation plays the dominant role in opening gaps and creating transitional disks presented in this work.

We thank Lori Allen, Gregory Mosby, and Jesús Hernández for supplying the spectral types of objects, and John Tobin for the information of spectroscopic binaries and spectral types. We also thank Ignazio Pillitteri and Scott Wolk for supplying the X-ray luminosity of L1641 objects from their SOXS project.

Several of the authors were visiting astronomers at the Infrared Telescope Facility, which

is operated by the University of Hawaii under Cooperative Agreement no. NNX-08AE38A with the National Aeronautics and Space Administration, Science Mission Directorate, Planetary Astronomy Program.

This publication makes use of data products from the Two Micron All Sky Survey, which is a joint project of the University of Massachusetts and the Infrared Processing and Analysis Center/California Institute of Technology, funded by the National Aeronautics and Space Administration and the National Science Foundation.

This work is based on observations made with the *Spitzer Space Telescope*, which is operated by the Jet Propulsion Laboratory, California Institute of Technology under NASA contract 1407. Support for this work was provided by NASA through Contract Number 1257184 issued by JPL/Caltech, and Cornell subcontracts 31419-5714 to the University of Rochester. N. C. acknowledges support from NASA Origins grant NNX08AH94G. C. E. was supported by a Sagan Exoplanet Fellowship from the National Aeronautics and Space Administration and administered by the NASA Exoplanet Science Institute (NExScI).

A. Notes on Individual Objects

OriA-5: It is a single line spectroscopic binary (SB1), the average radial velocity is 18±4.8 km/s, and the maximum velocity difference between two components is 3.8±4.8 km/s (Tobin et al. 2009). Its SED shows steeply decreasing fluxes after 20 μm and this may be the reflection of the effect of a second companion. It also shows prominent crystalline silicate features.

OriA-8: This one satisfies the criteria on both n_{K-6} and n_{13-31}. There are no obviously resolved sources within 30 arcsec around the target, but the target image in the Digitized Sky Survey (DSS) looks elongated, and it is suspected to have contributions from two sources.

OriA-18: This object lies inside of the radially continuous disk model region in n_{13-31}-$EW(10\mu\text{m})$ space; however, its n_{K-6} is much less than the lower octile of n_{K-6}, which is one of the selection criteria. The reason for low n_{13-31} is due to the decreasing flux after 20 μm, which could be the effect of external strong radiation evaporating the outer disk. There are 3-4 other sources near this target. This object's spectral type is not known.

OriA-39: It satisfies only one criterion of n_{K-6}. Its IRS spectrum is very noisy (Figure 2). It is faint at IRS wavelengths, and the sky emission around it is very complicated because it lies in a fringe area of the bright nebula NGC 1977, even though there are no point sources within 40 arcsec.

OriA-47: It lies in a very crowded and complicated region. There are many HH objects about 2 arcmin away, and there is much complicated background emission from bright sources in the center of ONC, the Trapezium. There is also an additional point source about 1.5 arcsec away. Recently, OriA-47 has also been identified as a variable star, [PMD2009] 185, as well as the nearby star [PMD2009] 183 (Parihar et al. 2009). The IRS didn't resolve the signals from the two sources, and the IRS fluxes are the composite fluxes from both.

OriA-88: Its SL2 data is not available because the array of SL2 is saturated due to the bright radiation entering in the IRS Peak-up cameras. This target is located just outside of the HII region, about 9 arcmin away from the center of ONC (M42). The PAH features are real and come from the disk.

OriA-149: This target lies in a complicated region of OMC2/3. It is reported to be an X-ray source ([TKK] 780) (Tsujimoto et al. 2003), and there is a point source identified as an IR-source ([TKK] 774) about 5 arcsec away from the target. IRS SL and LL slits were placed to avoid [TKK] 774 as much as possible, but the source's IR radiation seems to affect LL1: there is a kind of extended emission entering in LL1 as background, very close to our target source. We tried to remove the effect from the extended emission as much as possible by blocking the pixels corresponding the emission and using multiple source extraction in AdOpt.

OriA-154: Its spectral indices and $EW(10\mu\mathrm{m})$ are similar to OriA-18, and it is located in a similar position on n_{13-31}-$EW(10\mu\mathrm{m})$ space. Source extraction for LL spectra was performed by AdOpt multiple source extraction because an additional source appeared in the LL slit. Its outer disk could be affected by strong radiation from nearby bright sources.

OriA-164: It lies in a dense dark core region, and it is very faint at optical wavelengths. This supports the large value of A_V found here, even though its spectral type is unknown so that there are large uncertainties in our A_V estimate. It is barely passed the criteria of $EW(10\mu\mathrm{m})$. Its SED, which is restricted from J band to 35 μm in IRS data, with strong silicate features at 10 μm and 20 μm, lets us infer that this object is a possible PTD.

OriA-174: The prominent emission lines in its IRS spectra are molecular hydrogen $\nu = 0 \rightarrow 0$ S(1), S(2), S(3) and S(5), which arise in the foreground and background cloud material rather than our target, and did not subtract away precisely. The object is an embedded source which is not shown up at optical wavelength ranges.

OriA-188: The spectral type of this object is not known. There were no issues in the IRS data reduction, and its SED is like an object with a central clearing or gap. About in 30 arcsec radius from the target there are three faint 2MASS objects, but they don't enter in the IRS slits. A significant environmental concern is that there are two OB type stars about 6.7 arcmin away from the target: iot Ori (O9) and V2451 Ori (B7). The disk surface of the target may be affected by the strong radiation from the bright sources.

OriA-198: This target also barely passed the criteria on $EW(10\mu\mathrm{m})$ while its n_{K-6} and n_{13-31} fail to pass the criteria. There is a bright nebula, [B77] 122, about 7 arcmin away, and no nearby sources within 10 arcsec of the target. OriA-198 has strong silicate features

at 10 μm and 20 μm. These could be due to radial gaps in a more settled disk than a typical ClassII disk.

OriA-221 Its $EW(10)\mu$m satisfies the TD selection criteria, and it lies in the area of the well studied TDs of Tau, the region of outliers in n_{13-31} vs. $EW(10)\mu$m space. After extinction correction, this object's flux at optical wavelengths exceeds considerably that expected for photospheric spectra that fit well at longer wavelengths. This could be overcorrection of extinction toward the star, but we consider it more likely to be due to near-edge-on view and the extinction overcorrection of scattered visible light. There are several 2MASS objects within 40 arcsec, but they do not affect the source extraction at all. There is a bright B type star 7.4 arcmin away, HR 1911 (B1; double or multiple system). This target is also a PTD candidate.

B. Consideration of $\dot{M}$ and $\dot{M}_W$ from XPE

To ponder the mass dissipation through $\dot{M}$ and/or the expected mass loss rate ($\dot{M}_W$), we overlay ($\dot{M}_W$) by X-ray photoevaporation (Owen et al. 2012) on the observed mass accretion rate of TDs in Figure 25. The plus and cross data points in Figure 25 is the estimated $\dot{M}_W$ of each TD with its $M_\star$ and L_X as the input condition of $\dot{M}_W$. The estimated $\dot{M}_W$ have higher values than the mass accretion rates for most targets with high L_X and high $\dot{M}$. However, $\dot{M}_W$ is weaker comparing $\dot{M}$ of CTTS indicated as the gray dashed line. From this, we may raise the question of when $\dot{M}_W$ overcomes $\dot{M}$ to create a gap/hole like in TDs. The $\dot{M}$ of TDs is not the $\dot{M}$ when $\dot{M}_W$ is able to open a gap. However, the estimated $\dot{M}_W$ are not very different whether for radially continuous disks (plus sign) or disks with a large inner hole (cross sign). If we assume that each TD should have followed the gray dashed line for their initial $\dot{M}$-L_X relation before they became TDs, their initial $\dot{M}$ must have been greater than the theoretical $\dot{M}_W$. And the current $\dot{M}$ of TDs are much lower than the theoretical $\dot{M}_W$ of TDs. Some possible scenarios might explain these inconsistencies: (1) the TDs in our sample have already evolved much after gap opening, and they have lost much inner material to accrete to the central star; (2) there could be some other contribution (e.g. planets) to make the mass accretion rate decrease quickly, such as intercepting disk material on the way to the central star while $\dot{M}_W$ forces material to drift away outward.

C. Trends of TDs in Orion A

We examine trends for the sample of TDs in Orion A and the linear correlations of any two properties in $log - log$ scale are listed in Table 9 and Table 10. Comparing trends in Table 9 and Table 7 before separating by subtypes of TDs, the trends of TDs in Orion A generally agree within 1 σ uncertainties with the trends of the full sample of TDs not only from Orion A but also from Tau, ChaI, Oph, and N1333, despite L_X and $M_\star$ of TDs in Orion A tend to distribute toward lower values than that of other region. The trends of subtypes of TDs of Orion A in Table 10 are also not very different from that of full samples in Table 8, even though uncertainties of the results from linear regression are larger due to smaller sample sizes for some correlations. We will discuss difference/similarity of properties of TDs and Class II objects in Orion A from that in other star-forming regions in a separate paper (Kim et al. 2013) because the discussion is outside the scope of this paper.

REFERENCES

Alexander, R. D., Clarke, C. J., & Pringle, J. E. 2006a, MNRAS, 369, 216

—. 2006b, MNRAS, 369, 229

Allen, L. & Mosby, G. 2008, personal communication

Allen, L. E. 1995, PhD thesis, School of Physics, University of New South Wales, Sydney, NSW 2052, Australia ¡EMAIL¿lea@newt.phys.unsw.edu.au¡/EMAIL¿

Andrews, S. M. & Williams, J. P. 2005, ApJ, 631, 1134

—. 2007, ApJ, 671, 1800

Andrews, S. M., Wilner, D. J., Espaillat, C., Hughes, A. M., Dullemond, C. P., McClure, M. K., Qi, C., & Brown, J. M. 2011, ApJ, 732, 42

Andrews, S. M., Wilner, D. J., Hughes, A. M., Qi, C., & Dullemond, C. P. 2009, ApJ, 700, 1502

Arnold, L. A., Watson, D. M., Kim, K. H., Manoj, P., Remming, I., Sheehan, P., Adame, L., et al. 2012, ApJS, 201, 12

Baraffe, I., Chabrier, G., Allard, F., & Hauschildt, P. H. 1998, A&A, 337, 403

Bertout, C., Siess, L., & Cabrit, S. 2007, A&A, 473, L21

Brauer, F., Dullemond, C. P., & Henning, T. 2008, A&A, 480, 859

Brauer, F., Dullemond, C. P., Johansen, A., Henning, T., Klahr, H., & Natta, A. 2007, A&A, 469, 1169

Brown, J. M., Blake, G. A., Dullemond, C. P., Merín, B., Augereau, J. C., Boogert, A. C. A., Evans, II, N. J., et al. 2007, ApJ, 664, L107

Calvet, N., D'Alessio, P., Watson, D. M., Franco-Hernández, R., Furlan, E., Green, J., Sutter, P. M., et al. 2005, ApJ, 630, L185

Calvet, N., Muzerolle, J., Briceño, C., Hernández, J., Hartmann, L., Saucedo, J. L., & Gordon, K. D. 2004, AJ, 128, 1294

Chiang, E. & Murray-Clay, R. 2007, Nature Physics, 3, 604

Ciesla, F. J. 2007, ApJ, 654, L159

Cieza, L. A., Schreiber, M. R., Romero, G. A., Mora, M. D., Merin, B., Swift, J. J., Orellana, M., et al. 2010, ApJ, 712, 925

Clarke, C. J., Gendrin, A., & Sotomayor, M. 2001, MNRAS, 328, 485

Currie, T., Lada, C. J., Plavchan, P., Robitaille, T. P., Irwin, J., & Kenyon, S. J. 2009, ApJ, 698, 1

Currie, T. & Sicilia-Aguilar, A. 2011, ApJ, 732, 24

Cushing, M. C., Rayner, J. T., & Vacca, W. D. 2005, ApJ, 623, 1115

Cushing, M. C., Vacca, W. D., & Rayner, J. T. 2004, PASP, 116, 362

Da Rio, N., Robberto, M., Soderblom, D. R., Panagia, N., Hillenbrand, L. A., Palla, F., & Stassun, K. 2010, VizieR Online Data Catalog, 2183, 30261

D'Alessio, P., Calvet, N., & Hartmann, L. 2001, ApJ, 553, 321

D'Alessio, P., Calvet, N., Hartmann, L., Franco-Hernández, R., & Servín, H. 2006, ApJ, 638, 314

D'Alessio, P., Hartmann, L., Calvet, N., Franco-Hernández, R., Forrest, W. J., Sargent, B., Furlan, E., et al. 2005, ApJ, 621, 461

D'Antona, F. & Mazzitelli, I. 1997, Mem. Soc. Astron. Italiana, 68, 807

Dodson-Robinson, S. E., Willacy, K., Bodenheimer, P., Turner, N. J., & Beichman, C. A. 2009, Icarus, 200, 672

Draine, B. T. & Lee, H. M. 1984, ApJ, 285, 89

Drake, J. J., Ercolano, B., Flaccomio, E., & Micela, G. 2009, ApJ, 699, L35

Dullemond, C. P. & Dominik, C. 2005, A&A, 434, 971

Edgar, R. G., Quillen, A. C., & Park, J. 2007, MNRAS, 381, 1280

Ercolano, B., Clarke, C. J., & Drake, J. J. 2009, ApJ, 699, 1639

Espaillat, C. 2009, PhD thesis, University of Michigan

Espaillat, C., Calvet, N., D'Alessio, P., Bergin, E., Hartmann, L., Watson, D., Furlan, E., et al. 2007a, ApJ, 664, L111

Espaillat, C., Calvet, N., D'Alessio, P., Hernández, J., Qi, C., Hartmann, L., Furlan, E., & Watson, D. M. 2007b, ApJ, 670, L135

Espaillat, C., Calvet, N., Luhman, K. L., Muzerolle, J., & D'Alessio, P. 2008, ApJ, 682, L125

Espaillat, C., D'Alessio, P., Hernández, J., Nagel, E., Luhman, K. L., Watson, D. M., Calvet, N., Muzerolle, J., & McClure, M. 2010, ApJ, 717, 441

Espaillat, C., Furlan, E., D'Alessio, P., Sargent, B., Nagel, E., Calvet, N., Watson, D. M., & Muzerolle, J. 2011, ApJ, 728, 49

Espaillat, C., Ingleby, L., Hernández, J., Furlan, E., D'Alessio, P., Calvet, N., Andrews, S., et al. 2012, ApJ, 747, 103

Evans, I. N., Primini, F. A., Glotfelty, K. J., Anderson, C. S., Bonaventura, N. R., Chen, J. C., Davis, J. E., et al. 2010, ApJS, 189, 37

Evans, N., Calvet, N., Cieza, L., Forbrich, J., Hillenbrand, L., Lada, C., Merín, B., Strom, S., & Watson, D. 2009, ArXiv e-prints

Fang, M., van Boekel, R., Wang, W., Carmona, A., Sicilia-Aguilar, A., & Henning, T. 2009, A&A, 504, 461

Font, A. S., McCarthy, I. G., Johnstone, D., & Ballantyne, D. R. 2004, ApJ, 607, 890

Forrest, W. J., Sargent, B., Furlan, E., D'Alessio, P., Calvet, N., Hartmann, L., Uchida, K. I., et al. 2004, ApJS, 154, 443

Furlan, E., Luhman, K. L., Espaillat, C., D'Alessio, P., Adame, L., Manoj, P., Kim, K. H., et al. 2011, ApJS, 195, 3

Furlan, E., Watson, D. M., McClure, M. K., Manoj, P., Espaillat, C., D'Alessio, P., Calvet, N., et al. 2009, ApJ, 703, 1964

Gâlfalk, M. & Olofsson, G. 2008, A&A, 489, 1409

Garaud, P. 2007, ApJ, 671, 2091

Gatti, T., Natta, A., Randich, S., Testi, L., & Sacco, G. 2008, A&A, 481, 423

Gorti, U., Dullemond, C. P., & Hollenbach, D. 2009, ApJ, 705, 1237

Gorti, U. & Hollenbach, D. 2009, ApJ, 690, 1539

Greaves, J. S. & Rice, W. K. M. 2010, MNRAS, 407, 1981

Güdel, M., Briggs, K. R., Arzner, K., Audard, M., Bouvier, J., Feigelson, E. D., Franciosini, E., et al. 2007, A&A, 468, 353

Gullbring, E., Hartmann, L., Briceno, C., & Calvet, N. 1998, ApJ, 492, 323

Hartmann, L., Calvet, N., Gullbring, E., & D'Alessio, P. 1998, ApJ, 495, 385

Hartmann, L., D'Alessio, P., Calvet, N., & Muzerolle, J. 2006, ApJ, 648, 484

Hernandez, J. 2008, personal communication

Hernandez, J. & Tobin, J. 2009, personal communication

Higdon, S. J. U., Devost, D., Higdon, J. L., Brandl, B. R., Houck, J. R., Hall, P., Barry, D., et al. 2004, PASP, 116, 975

Hillenbrand, L. A. 1997a, AJ, 113, 1733

—. 1997b, AJ, 113, 1733

Holland, W. S., Greaves, J. S., Zuckerman, B., Webb, R. A., McCarthy, C., Coulson, I. M., Walther, D. M., et al. 1998, Nature, 392, 788

Hollenbach, D., Johnstone, D., Lizano, S., & Shu, F. 1994, ApJ, 428, 654

Houck, J. R., Roellig, T. L., van Cleve, J., Forrest, W. J., Herter, T., Lawrence, C. R., Matthews, K., et al. 2004, ApJS, 154, 18

Hsu, W.-H., Hartmann, L., Allen, L., Hernández, J., Megeath, S. T., Mosby, G., Tobin, J. J., & Espaillat, C. 2012, ApJ, 752, 59

Hughes, A. M., Andrews, S. M., Espaillat, C., Wilner, D. J., Calvet, N., D'Alessio, P., Qi, C., Williams, J. P., & Hogerheijde, M. R. 2009, ApJ, 698, 131

Hughes, A. M., Wilner, D. J., Calvet, N., D'Alessio, P., Claussen, M. J., & Hogerheijde, M. R. 2007, ApJ, 664, 536

Inutsuka, S.-i., Machida, M. N., & Matsumoto, T. 2010, ApJ, 718, L58

Ireland, M. J. & Kraus, A. L. 2008, ApJ, 678, L59

Jura, M. & Turner, J. 1998, Nature, 395, 144

Kelly, B. C. 2007, ApJ, 665, 1489

Kenyon, S. J. & Hartmann, L. 1995, ApJS, 101, 117

Kim, K. H., Watson, D. M., Manoj, P., Forrest, W. J., Furlan, E., Sargent, B. A., Najita, J. R., et al. 2013, in preparation

Kim, K. H., Watson, D. M., Manoj, P., Furlan, E., Najita, J., Forrest, W. J., Sargent, B., et al. 2009, ApJ, 700, 1017

Kraus, A. L. & Ireland, M. J. 2012, in American Astronomical Society Meeting Abstracts, Vol. 219, American Astronomical Society Meeting Abstracts, 228.03

Kraus, A. L., Ireland, M. J., Martinache, F., & Hillenbrand, L. A. 2011, ApJ, 731, 8

Lada, C. J., Muench, A. A., Luhman, K. L., Allen, L., Hartmann, L., Megeath, T., Myers, P., et al. 2006, AJ, 131, 1574

Lebouteiller, V., Bernard-Salas, J., Sloan, G. C., & Barry, D. J. 2010, PASP, 122, 231

Lubow, S. H. & D'Angelo, G. 2006, ApJ, 641, 526

Luhman, K. L., Allen, P. R., Espaillat, C., Hartmann, L., & Calvet, N. 2010, ApJS, 186, 111

Manoj, P. 2010, in Astronomical Society of the Pacific Conference Series, Vol. 432, New Horizons in Astronomy: Frank N. Bash Symposium 2009, ed. L. M. Stanford, J. D. Green, L. Hao, & Y. Mao, 49

Manoj, P., Kim, K. H., Furlan, E., McClure, M. K., Luhman, K. L., Watson, D. M., Espaillat, C., et al. 2011, ApJS, 193, 11

Marsh, K. A. & Mahoney, M. J. 1992, ApJ, 395, L115

McClure, M. 2009, ApJ, 693, L81

McClure, M. K., Forrest, W. J., Sargent, B. A., Watson, D. M., Furlan, E., Manoj, P., Luhman, K. L., et al. 2008, ApJ, 683, L187

McClure, M. K., Furlan, E., Manoj, P., Luhman, K. L., Watson, D. M., Forrest, W. J., Espaillat, C., et al. 2010, ApJS, 188, 75

Megeath, S. T., Gutermuth, R., Muzerolle, J., Kryukova, E., Flaherty, K., Hora, J., Allen, L., et al. 2012, ArXiv e-prints

Menten, K. M., Reid, M. J., Forbrich, J., & Brunthaler, A. 2007, A&A, 474, 515

Merín, B., Brown, J. M., Oliveira, I., Herczeg, G. J., van Dishoeck, E. F., Bottinelli, S., Evans, II, N. J., et al. 2010, ApJ, 718, 1200

Meru, F. & Bate, M. R. 2010, MNRAS, 406, 2279

Meyer, M. R., Calvet, N., & Hillenbrand, L. A. 1997, AJ, 114, 288

Morishima, R. 2012, MNRAS, 420, 2851

Muench, A., Getman, K., Hillenbrand, L., & Preibisch, T. 2008, Star Formation in the Orion Nebula I: Stellar Content, ed. Reipurth, B., 483

Muzerolle, J., Allen, L. E., Megeath, S. T., Hernández, J., & Gutermuth, R. A. 2010, ApJ, 708, 1107

Muzerolle, J., Hartmann, L., & Calvet, N. 1998, AJ, 116, 2965

Muzerolle, J., Hillenbrand, L., Calvet, N., Briceño, C., & Hartmann, L. 2003, ApJ, 592, 266

Muzerolle, J., Luhman, K. L., Briceño, C., Hartmann, L., & Calvet, N. 2005, ApJ, 625, 906

Najita, J. R., Strom, S. E., & Muzerolle, J. 2007, MNRAS, 378, 369

Natta, A., Testi, L., & Randich, S. 2006, A&A, 452, 245

Olofsson, J., Benisty, M., Augereau, J.-C., Pinte, C., Ménard, F., Tatulli, E., Berger, J.-P., et al. 2011, A&A, 528, L6

Owen, J. E., Clarke, C. J., & Ercolano, B. 2012, MNRAS, 422, 1880

Owen, J. E., Ercolano, B., & Clarke, C. J. 2011a, MNRAS, 412, 13

—. 2011b, MNRAS, 411, 1104

Owen, J. E., Ercolano, B., Clarke, C. J., & Alexander, R. D. 2010, MNRAS, 401, 1415

Palla, F. & Stahler, S. W. 1999, ApJ, 525, 772

Parihar, P., Messina, S., Distefano, E., Shantikumar, N. S., & Medhi, B. J. 2009, MNRAS, 400, 603

Perez-Becker, D. & Chiang, E. 2011, ApJ, 735, 8

Piétu, V., Dutrey, A., Guilloteau, S., Chapillon, E., & Pety, J. 2006, A&A, 460, L43

Pillitteri, I., Wolk, S. J., Megeath, S. T., Allen, L., Bally, J., Gagne‘, M., Gutermuth, R. A., et al. 2013, ArXiv e-prints

Poteet, C., Watson, D. M., Megeath, S. T., & Muzerolle, J. 2013, in preparation

Pott, J.-U., Perrin, M. D., Furlan, E., Ghez, A. M., Herbst, T. M., & Metchev, S. 2010, ApJ, 710, 265

Quillen, A. C., Blackman, E. G., Frank, A., & Varnière, P. 2004, ApJ, 612, L137

Rayner, J. T., Cushing, M. C., & Vacca, W. D. 2009a, ApJS, 185, 289

—. 2009b, ApJS, 185, 289

Rayner, J. T., Toomey, D. W., Onaka, P. M., Denault, A. J., Stahlberger, W. E., Vacca, W. D., Cushing, M. C., & Wang, S. 2003, PASP, 115, 362

Rebull, L. M., Hillenbrand, L. A., Strom, S. E., Duncan, D. K., Patten, B. M., Pavlovsky, C. M., Makidon, R., & Adams, M. T. 2000, AJ, 119, 3026

Rice, W. K. M., Armitage, P. J., Wood, K., & Lodato, G. 2006, MNRAS, 373, 1619

Rice, W. K. M., Wood, K., Armitage, P. J., Whitney, B. A., & Bjorkman, J. E. 2003, MNRAS, 342, 79

Sargent, B. A., Forrest, W. J., Tayrien, C., McClure, M. K., Watson, D. M., Sloan, G. C., Li, A., et al. 2009, ApJS, 182, 477

Shu, F., Najita, J., Ostriker, E., Wilkin, F., Ruden, S., & Lizano, S. 1994, ApJ, 429, 781

Sicilia-Aguilar, A., Henning, T., & Hartmann, L. W. 2010, ApJ, 710, 597

Siess, L., Dufour, E., & Forestini, M. 2000, A&A, 358, 593

Simon, M., Dutrey, A., & Guilloteau, S. 2000, ApJ, 545, 1034

Skrutskie, M. F., Cutri, R. M., Stiening, R., Weinberg, M. D., Schneider, S., Carpenter, J. M., Beichman, C., et al. 2006, AJ, 131, 1163

Strom, K. M., Strom, S. E., Edwards, S., Cabrit, S., & Skrutskie, M. F. 1989, AJ, 97, 1451

Suzuki, T. K., Muto, T., & Inutsuka, S.-i. 2010, ApJ, 718, 1289

Tanaka, H., Himeno, Y., & Ida, S. 2005, ApJ, 625, 414

Tayrien, C. & Forrest, W. J. 2013, in preparation

Telleschi, A., Güdel, M., Briggs, K. R., Audard, M., & Palla, F. 2007, A&A, 468, 425

Thalmann, C., Grady, C. A., Goto, M., Wisniewski, J. P., Janson, M., Henning, T., Fukagawa, M., et al. 2010, ApJ, 718, L87

Tobin, J. J., Hartmann, L., Furesz, G., Mateo, M., & Megeath, S. T. 2009, ApJ, 697, 1103

Tsujimoto, M., Koyama, K., Kobayashi, N., Goto, M., Tsuboi, Y., & Tokunaga, A. T. 2003, AJ, 125, 1537

Vacca, W. D., Cushing, M. C., & Rayner, J. T. 2003, PASP, 115, 389

Varnière, P., Bjorkman, J. E., Frank, A., Quillen, A. C., Carciofi, A. C., Whitney, B. A., & Wood, K. 2006, ApJ, 637, L125

Watson, D. M., Leisenring, J. M., Furlan, E., Bohac, C. J., Sargent, B., Forrest, W. J., Calvet, N., et al. 2009a, ApJS, 180, 84

Watson, M. G., Schröder, A. C., Fyfe, D., Page, C. G., Lamer, G., Mateos, S., Pye, J., et al. 2009b, A&A, 493, 339

Werner, M. W., Roellig, T. L., Low, F. J., Rieke, G. H., Rieke, M., Hoffmann, W. F., Young, E., et al. 2004, ApJS, 154, 1

White, R. J. & Ghez, A. M. 2001, ApJ, 556, 265

Winston, E., Megeath, S. T., Wolk, S. J., Spitzbart, B., Gutermuth, R., Allen, L. E., Hernandez, J., et al. 2010, AJ, 140, 266

Zacharias, N., Monet, D. G., Levine, S. E., Urban, S. E., Gaume, R., & Wycoff, G. L. 2005, VizieR Online Data Catalog, 1297, 0

Zhu, Z., Nelson, R. P., Dong, R., Espaillat, C., & Hartmann, L. 2012, ApJ, 755, 6

Zhu, Z., Nelson, R. P., Hartmann, L., Espaillat, C., & Calvet, N. 2011, ApJ, 729, 47

Zuckerman, B. & Song, I. 2004, ApJ, 603, 738

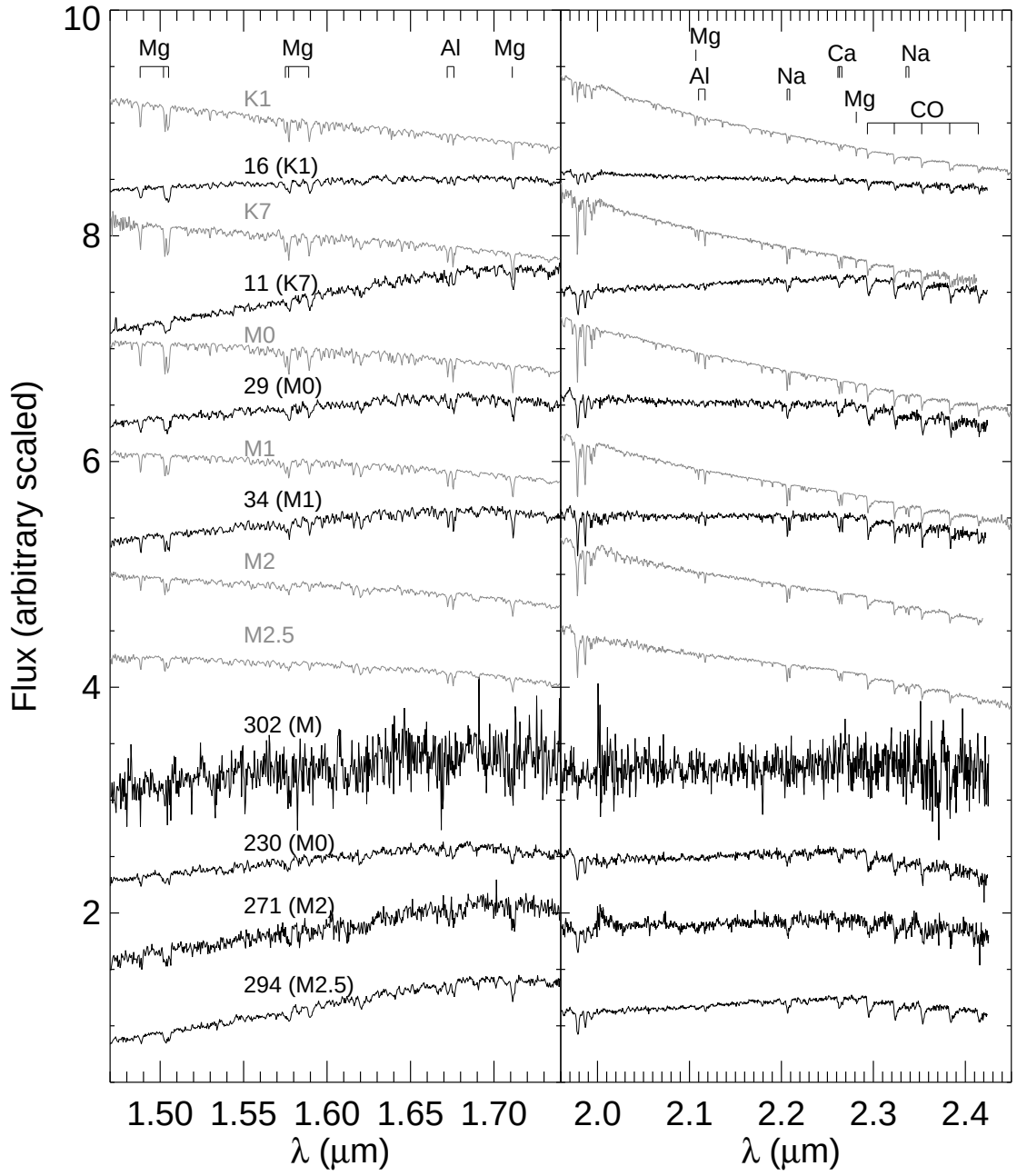

Fig. 1.— Spectral typing from SpeX spectra. The gray spectra with spectral type are the standard spectra of the spectral types (Rayner et al. 2009b). The black spectra with number and spectra type are the SpeX spectra of the objects with the ID number. We estimated their spectral type as the spectral type next to the object's number.

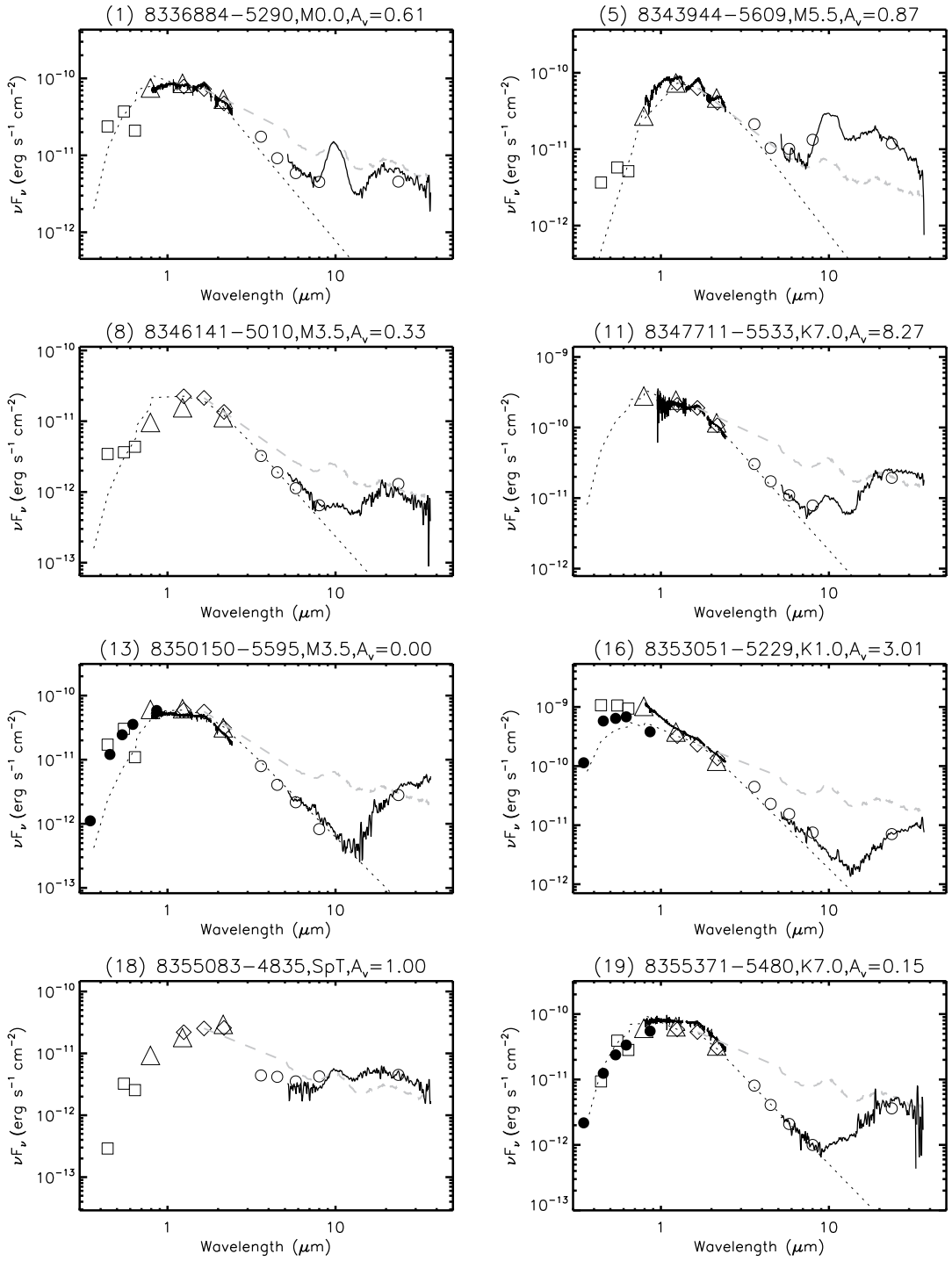

Fig. 2.— De-reddened SEDs of transitional disks in Orion A. The SEDs are composed of the following components: IRS (black line in the wavelength range of 5.2-35 μm); SpeX (black line in the wavelength range of 0.8-2.4 μm); IRAC and MIPS (open circles); 2MASS JHK (open diamonds); DENIS IJH(open triangles); UBVRI from Da Rio et al. (2010) (filled circles); BVR from NOMAD (open squares); photosphere (black short dashed line); the median spectrum of protoplanetary disks in Taurus region (gray long dashed line). The gray line from 0.8 to 2.4 μm in the plots of OriA-26, 38, 47, and 290 is for spectra of their companion resolved in the SpeX observations.

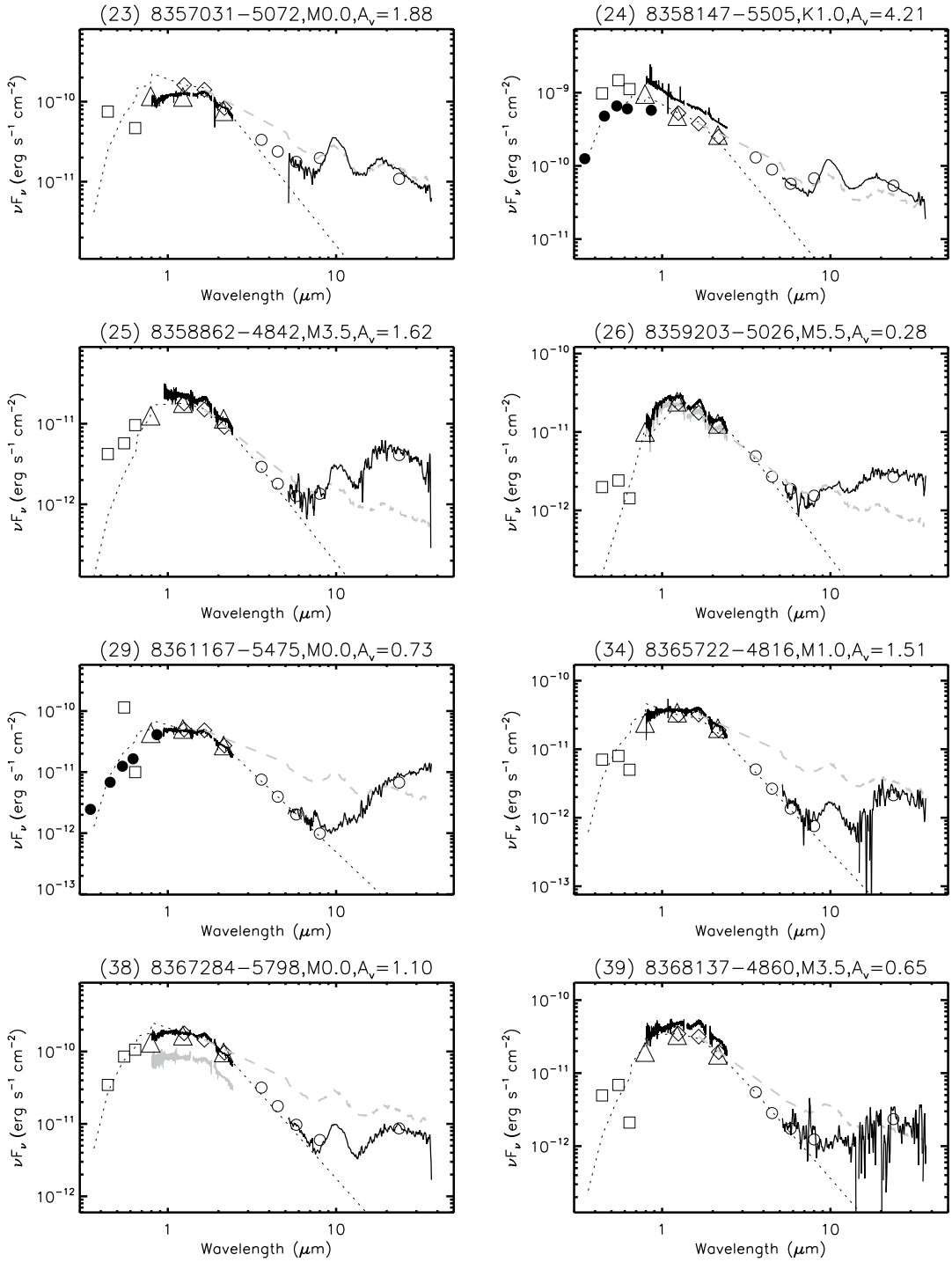

Fig. 2.— Figure 2. continued

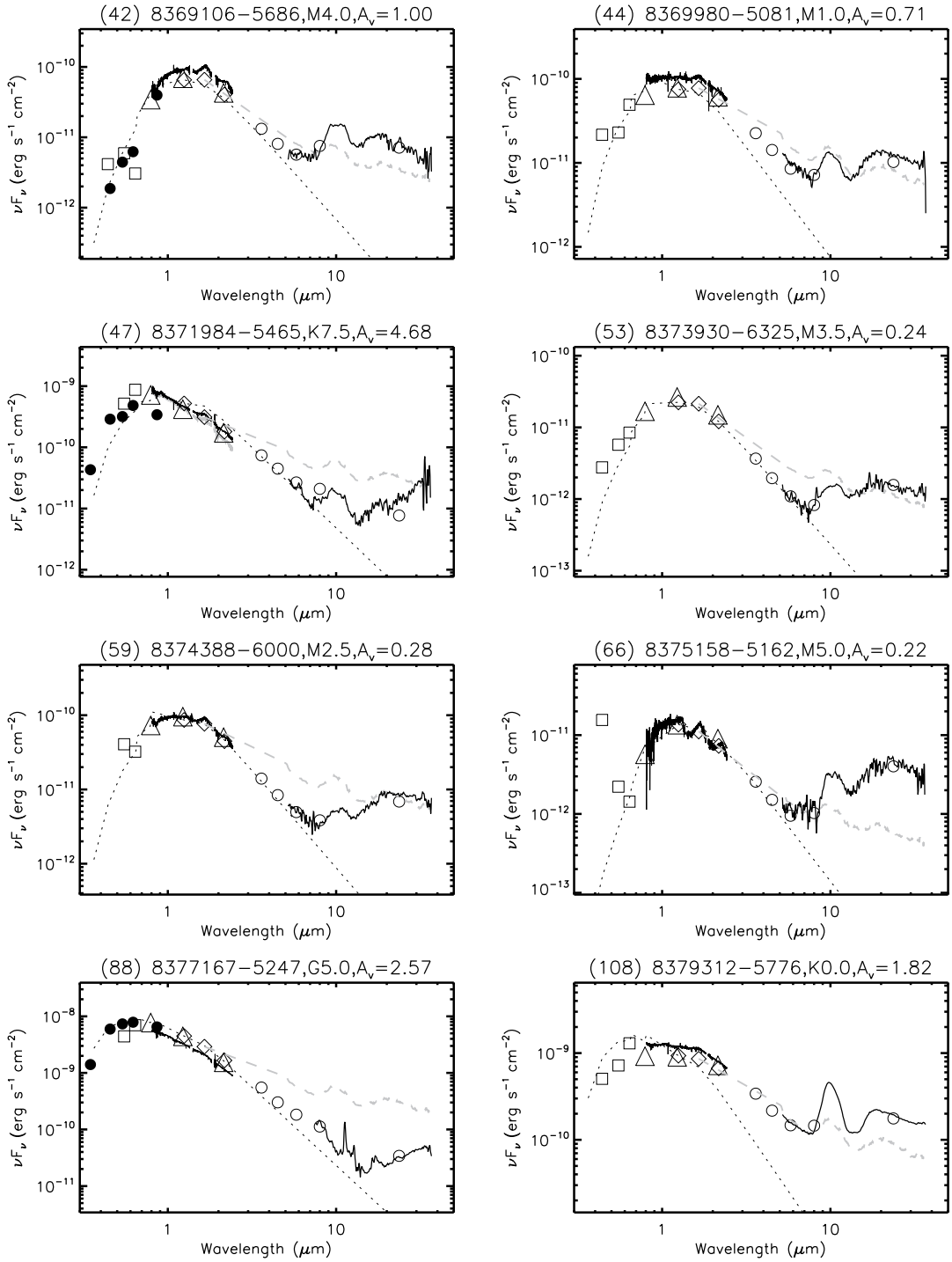

Fig. 2.— Figure 2. continued

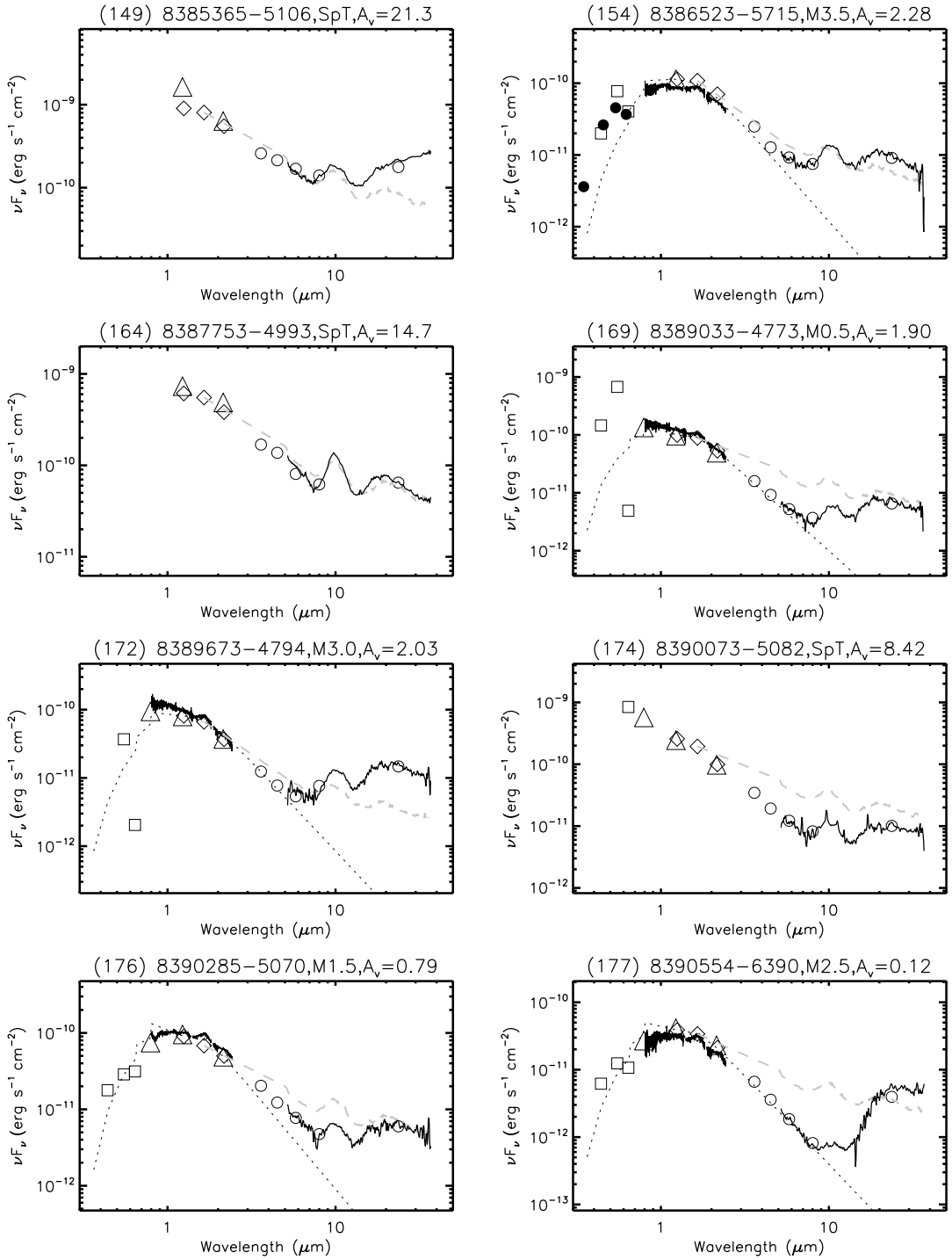

Fig. 2.— Figure 2. continued

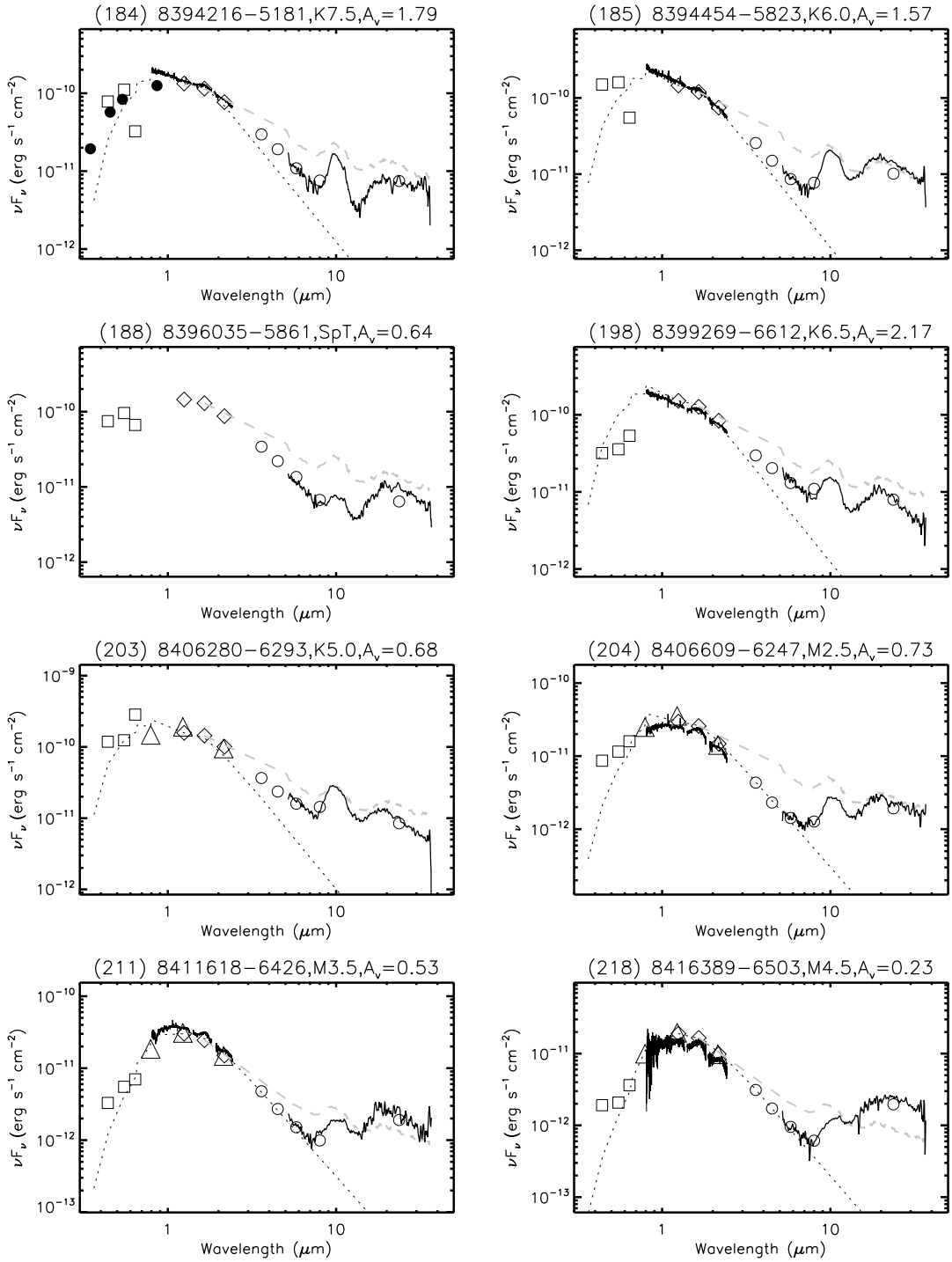

Fig. 2.— Figure 2. continued

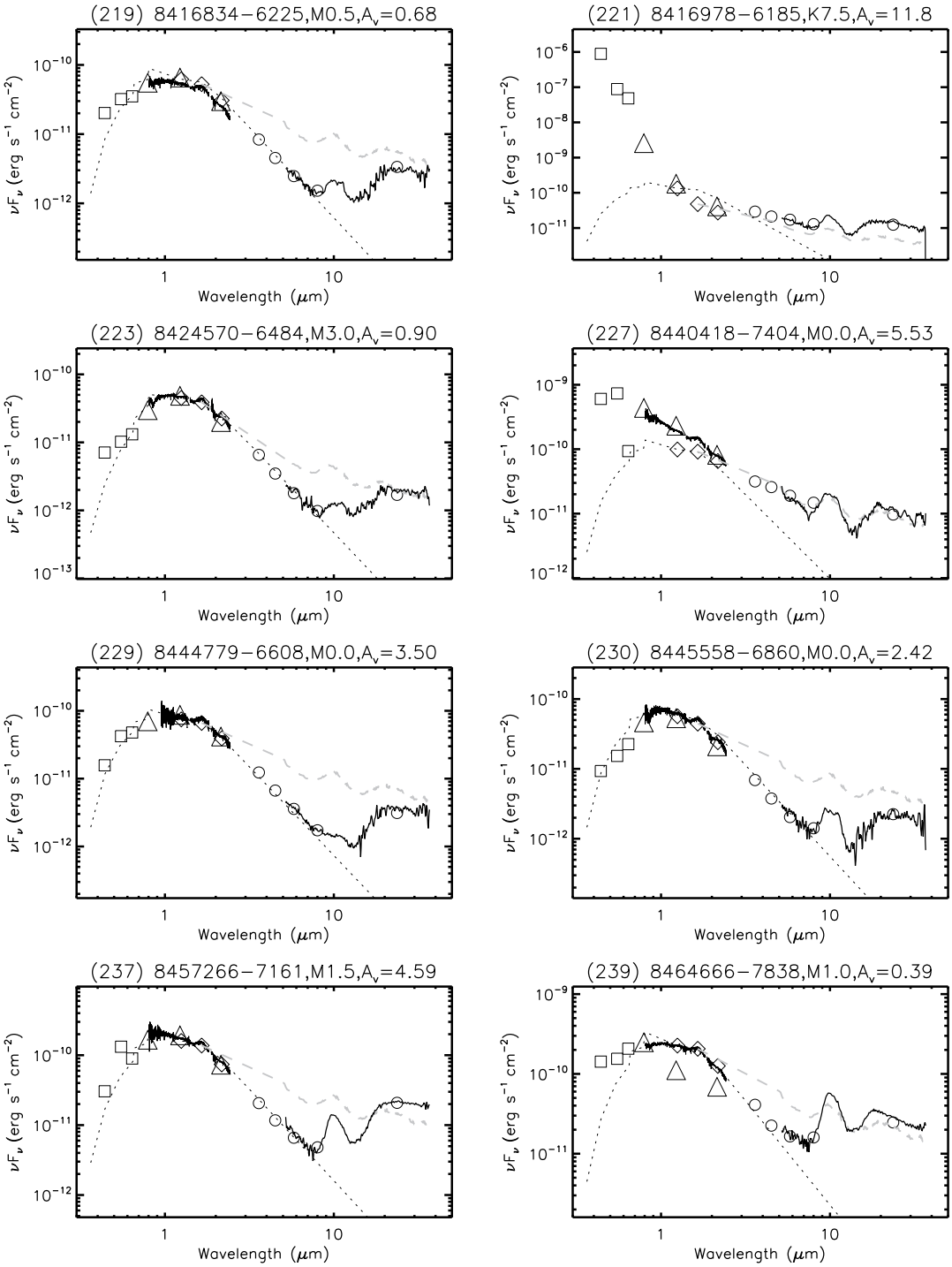

Fig. 2.— Figure 2. continued

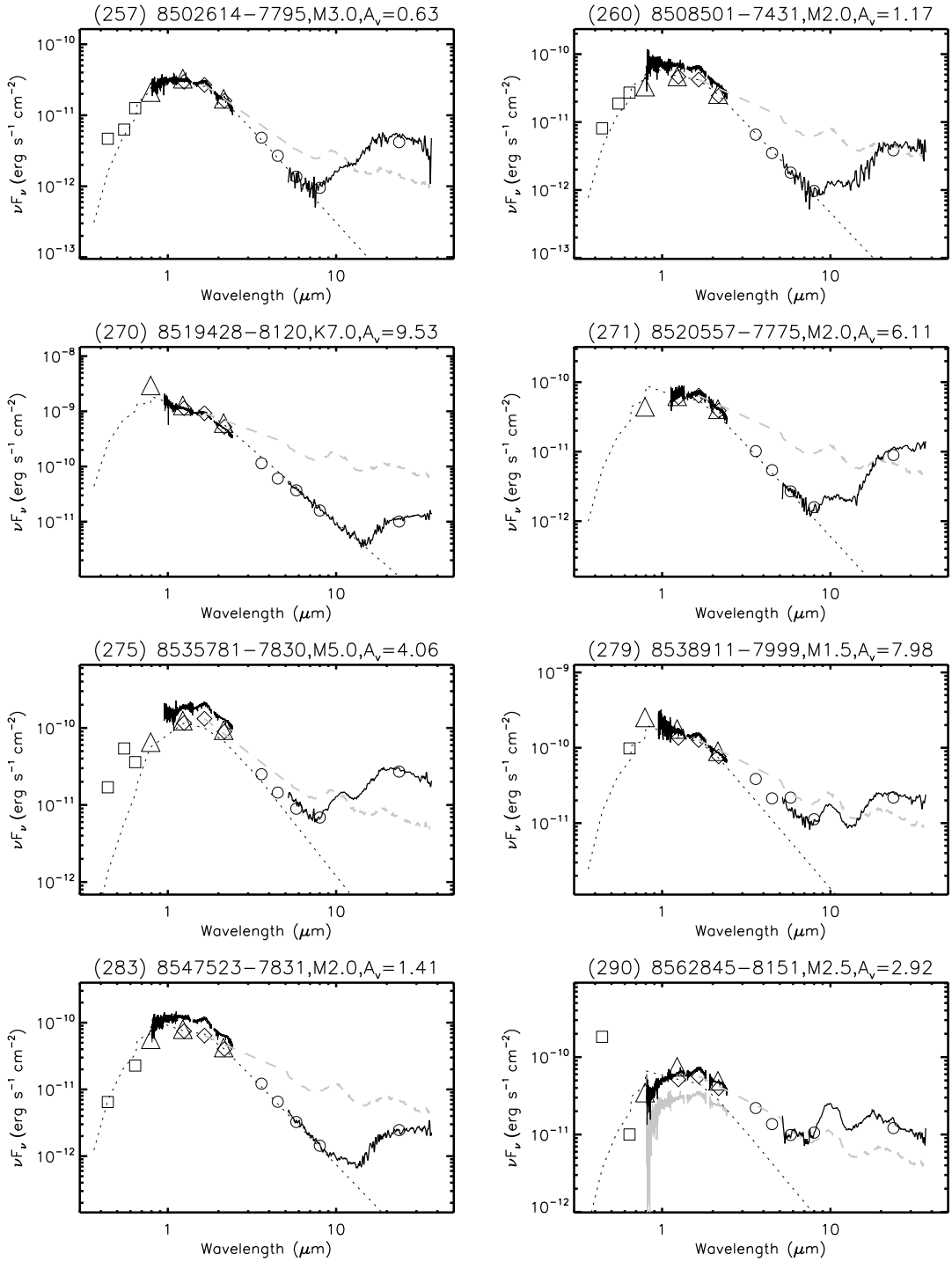

Fig. 2.— Figure 2. continued

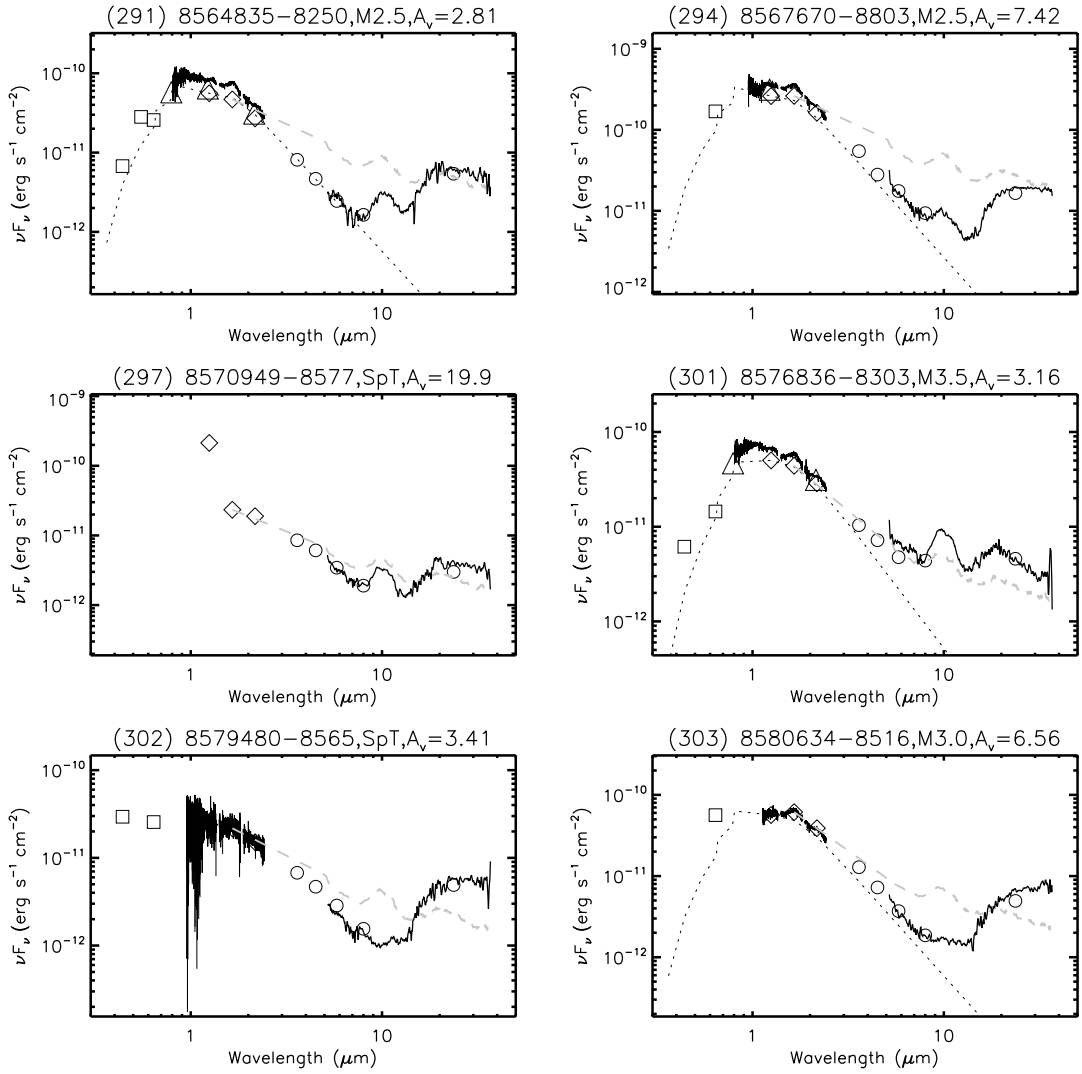

Fig. 2.— Figure 2. continued

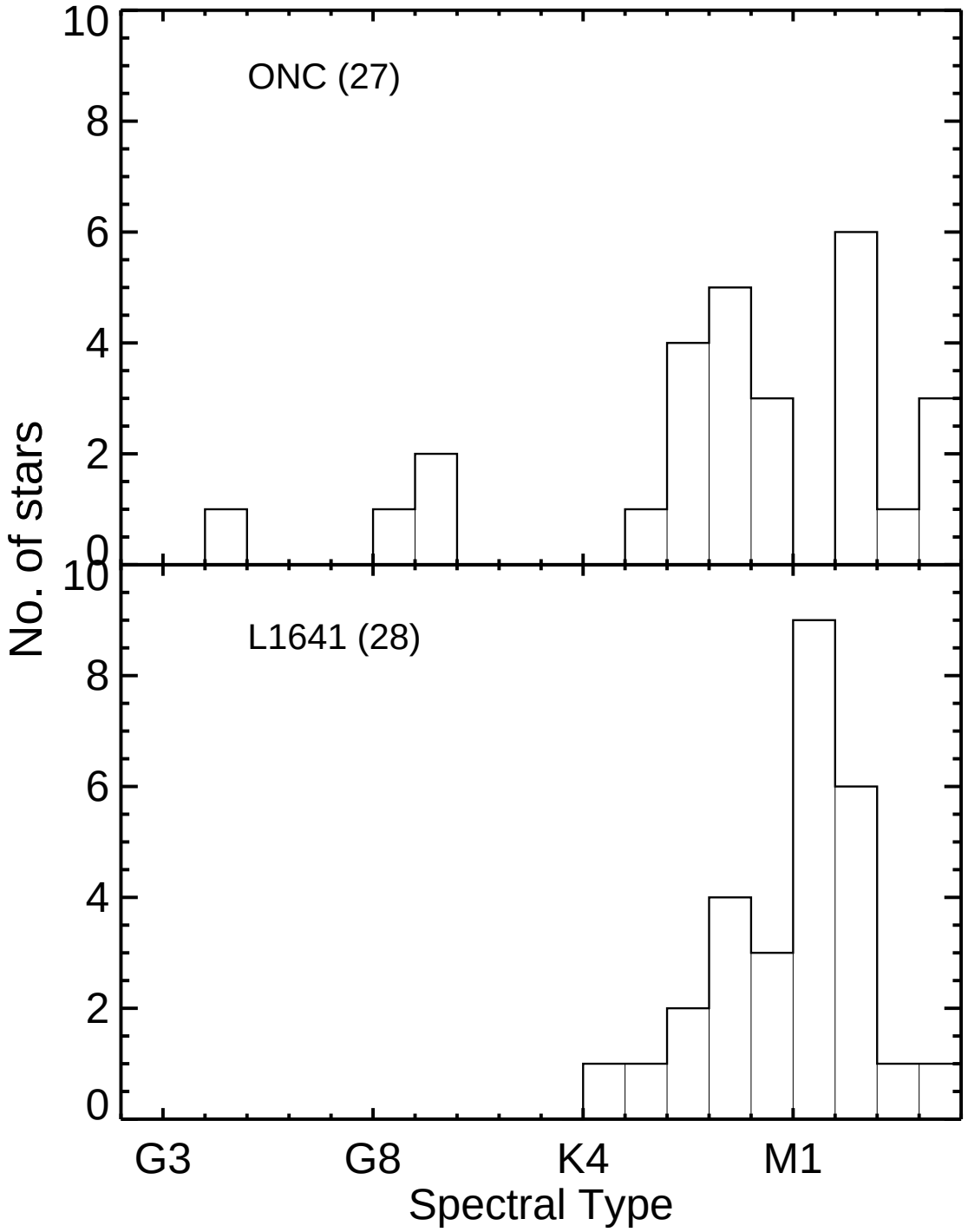

Fig. 3.— Spectral type distribution for host stars of transitional disks in Orion A.

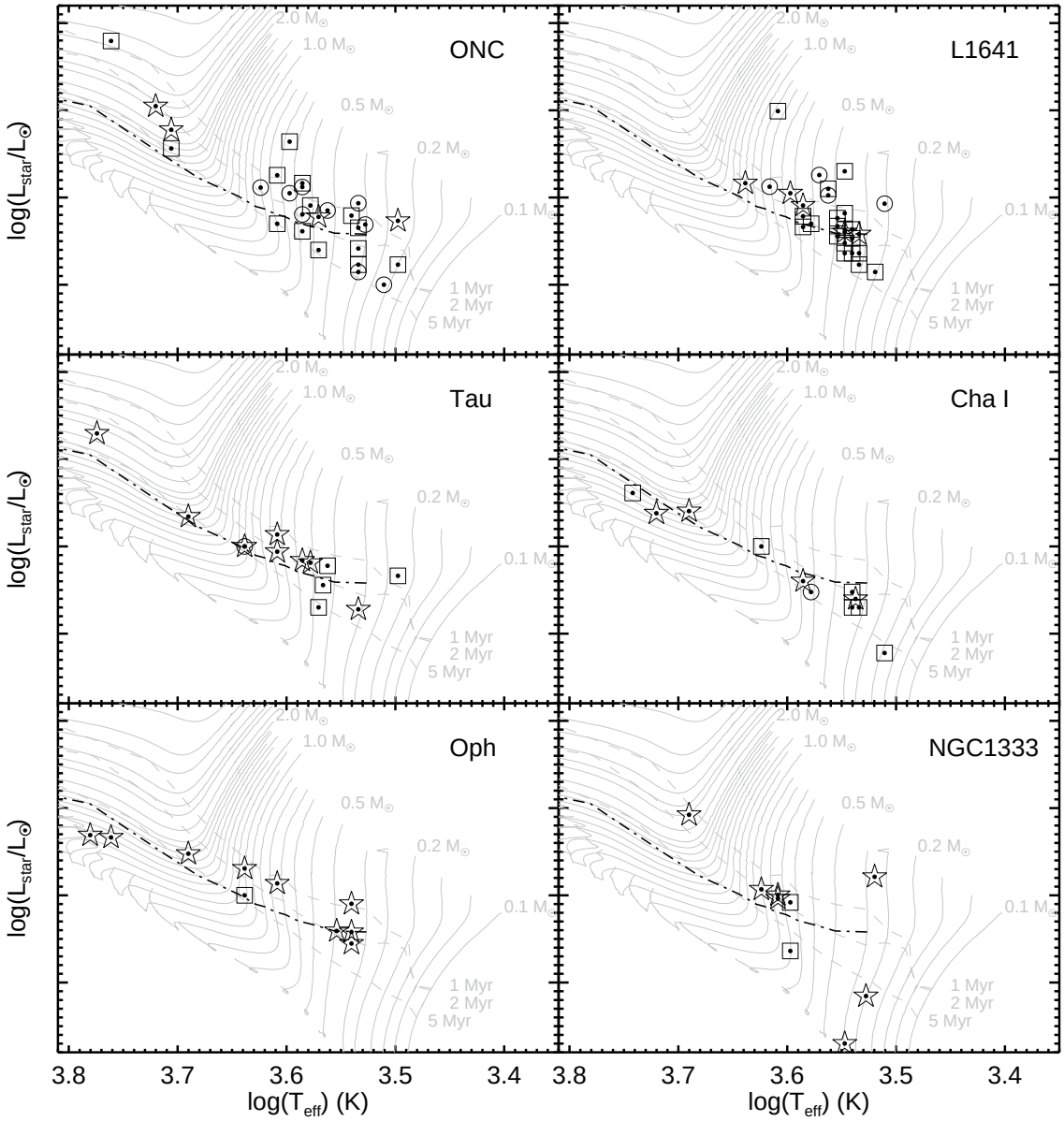

Fig. 4.— HR diagrams for host stars of transitional disks in this paper. Squares are for CTDs; circles are for WTDs; stars are for PTDs. Evolutionary tracks and isochrones are from Siess et al. (2000) (Z=0.02). Isochrone ages of various types of transitional-disk systems range from < 1 Myr to > 5 Myr. The average disk life time in Tau-Aur (Bertout et al. 2007) is also shown as a dash-dotted line for reference.

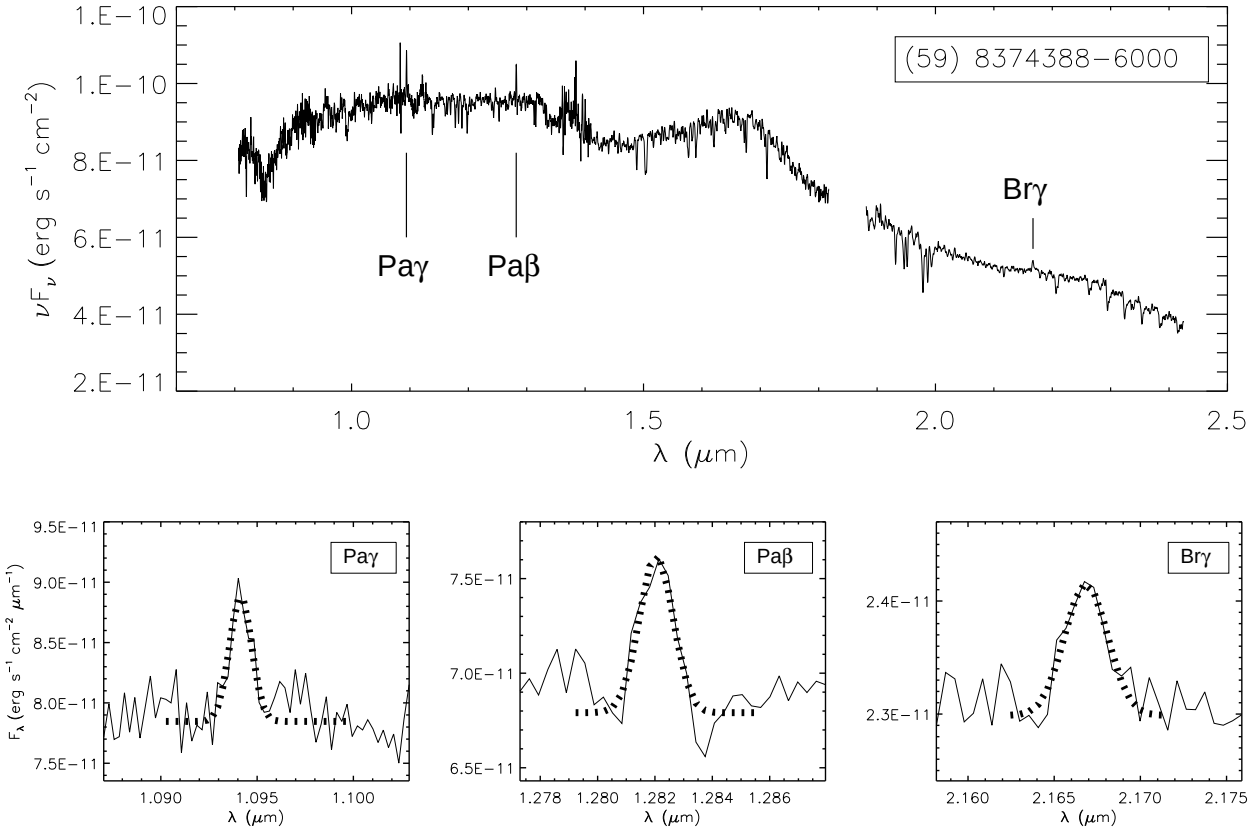

Fig. 5.— Example of mass accretion rate measurement from hydrogen recombination lines.

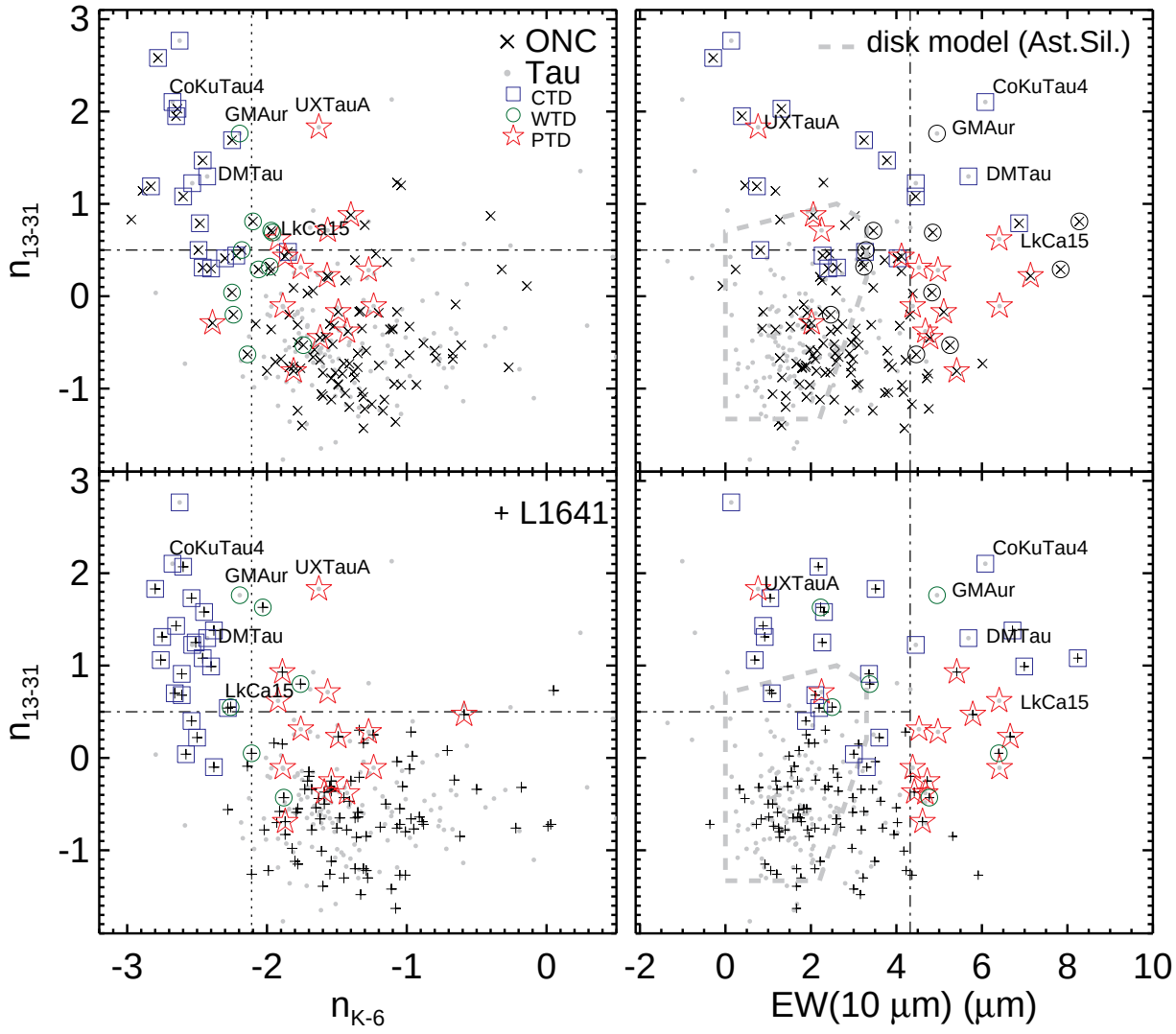

Fig. 6.— Selection of OriA TDs by n_{13-31} vs. n_{K-6} (the left panels) and n_{13-31} vs. $EW(10\mu\mathrm{m})$ (the right panels). In the right panels, the polygon with thick dashed line indicates the coverage area by a typical accretion disks model (D'Alessio et al. 2006). The upper panels are for the TD selection in ONC, and the lower panels are for the TD selection in L1641. In each plot, samples in Tau (Furlan et al. 2011) are also included for comparison. The dash-dotted lines indicate the upper octile; the dotted lines indicate the lower octile. (A color version of this figure is available in the online journal.)

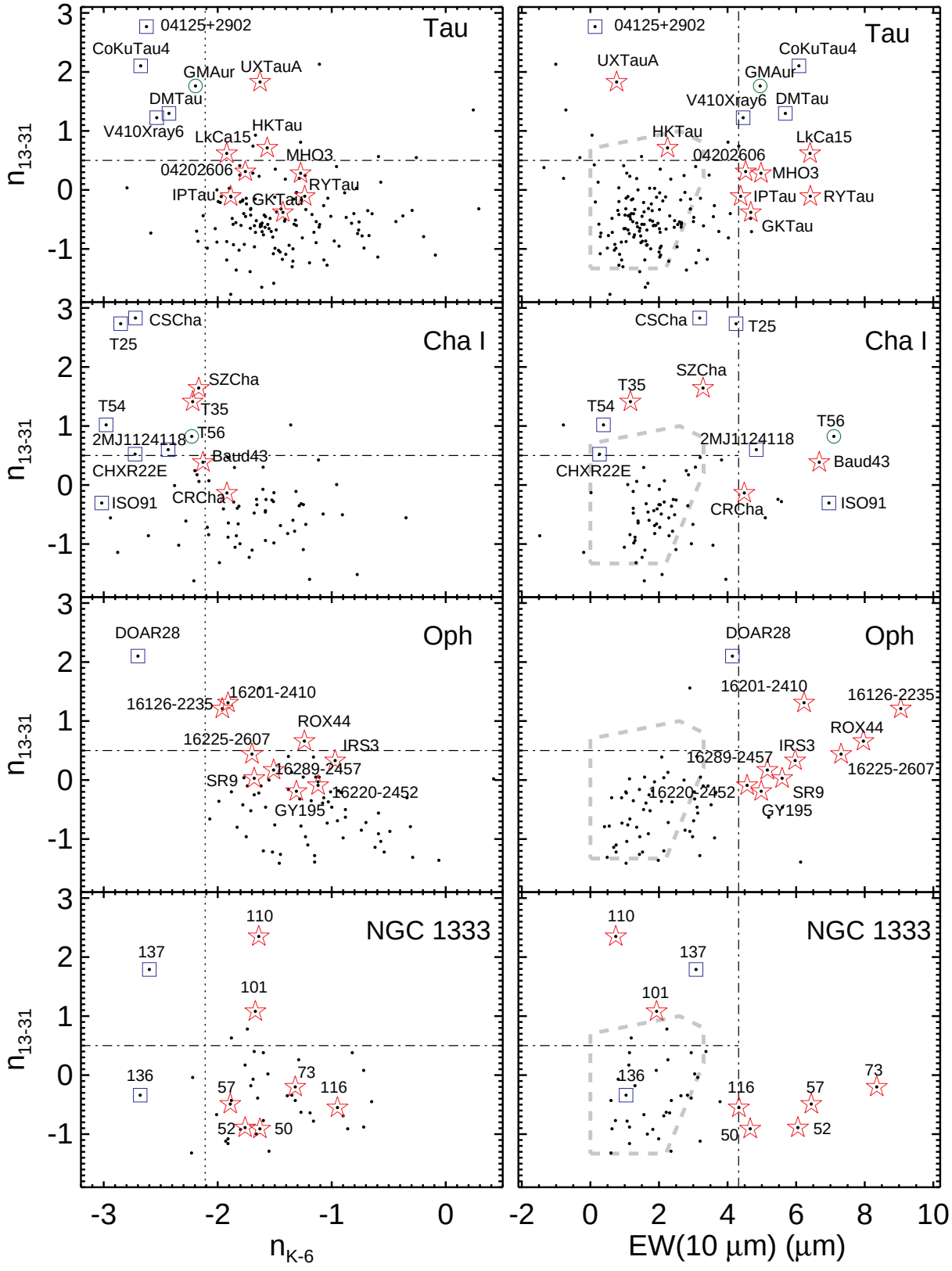

Fig. 7.— Selection of TDs in other star-forming regions, Tau, Cha I, Oph, and NGC 1333, by the criteria in n_{13-31} vs. n_{K-6} (the left panels) and n_{13-31} vs. $EW(10\mu m)$ (the right panels). The meanings of different symbols and lines are same as Figure 6. (A color version of this figure is available in the online journal.)

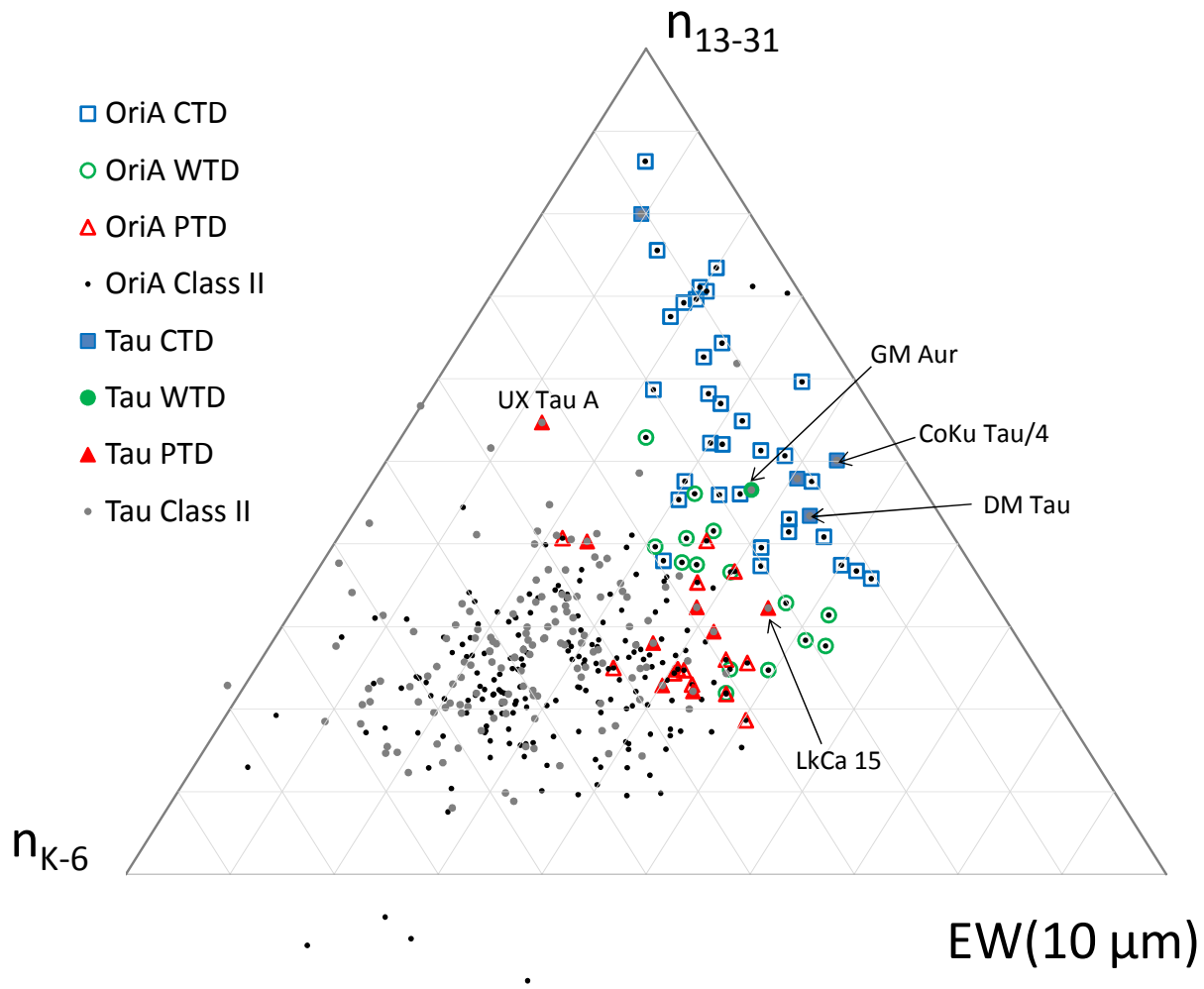

Fig. 8.— Disks samples of Orion A (black dots) and Tau (gray dots) are plotted in the spaces of three parameters. TDs are indicated by subtypes: CTDs (squares), WTDs (circles), and PTDs (triangles). Orion A TDs are open symbols and Tau TDs are filled symbols. The center of this plot is corresponding to the projected origin of the three axes. The three axes values are from 0 to 100, which are linearly transformed from their original values of [-3, 0] for n_{K-6}, [-2, 3] for n_{13-31}, and [-1, 9] for $EW(10\mu\mathrm{m})$. (A color version of this figure is available in the online journal.)

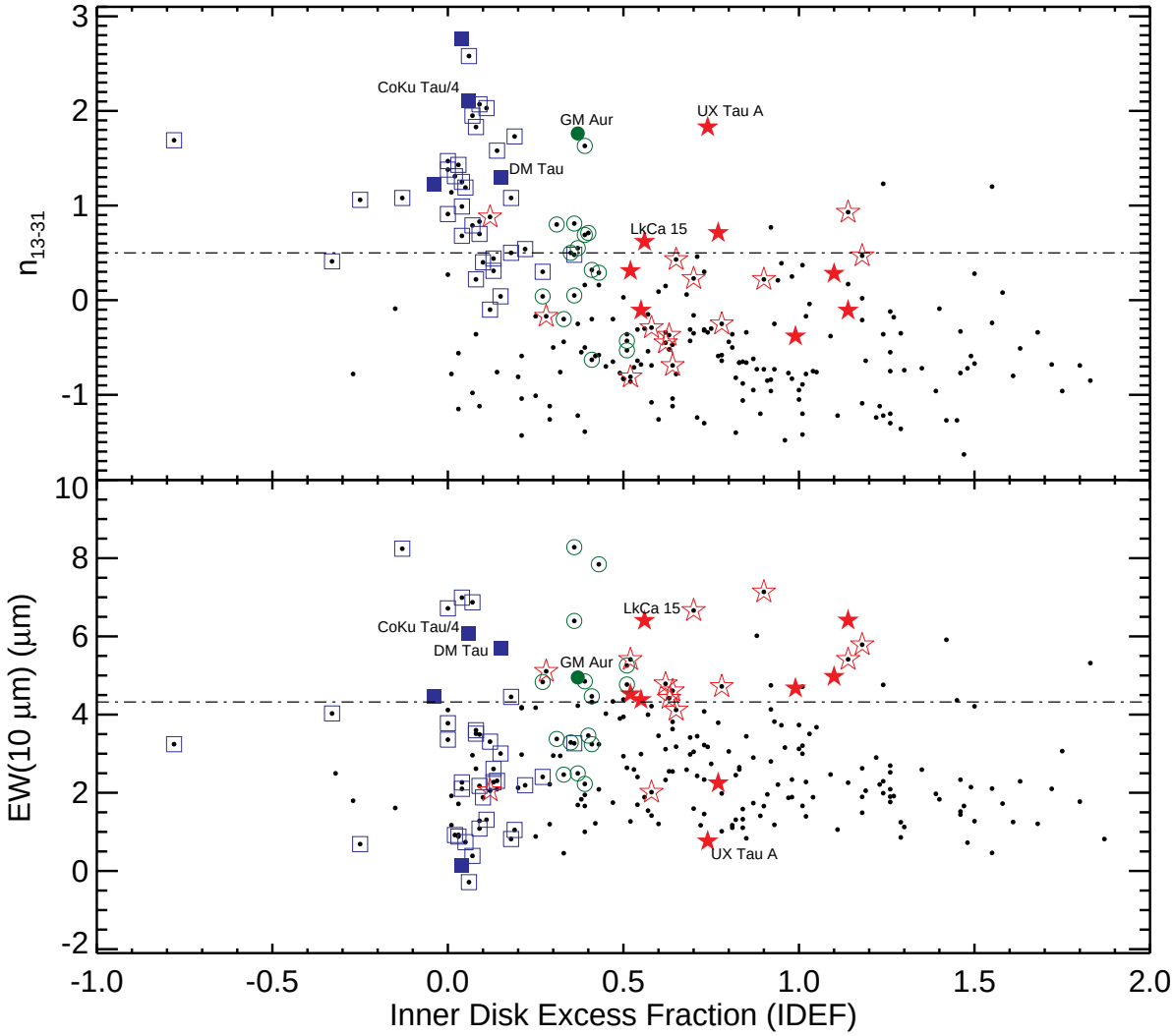

Fig. 9.— n_{13-31} and $EW(10\mu\mathrm{m})$ plotted against IDEF (Inner Disk Excess Fraction). TDs of Orion A and Tau are indicated in open and filled symbols: CTDs (squares), WTDs (circles) and PTDs (stars). The dots indicate radially-continuous disks of Orion A. (A color version of this figure is available in the online journal.)

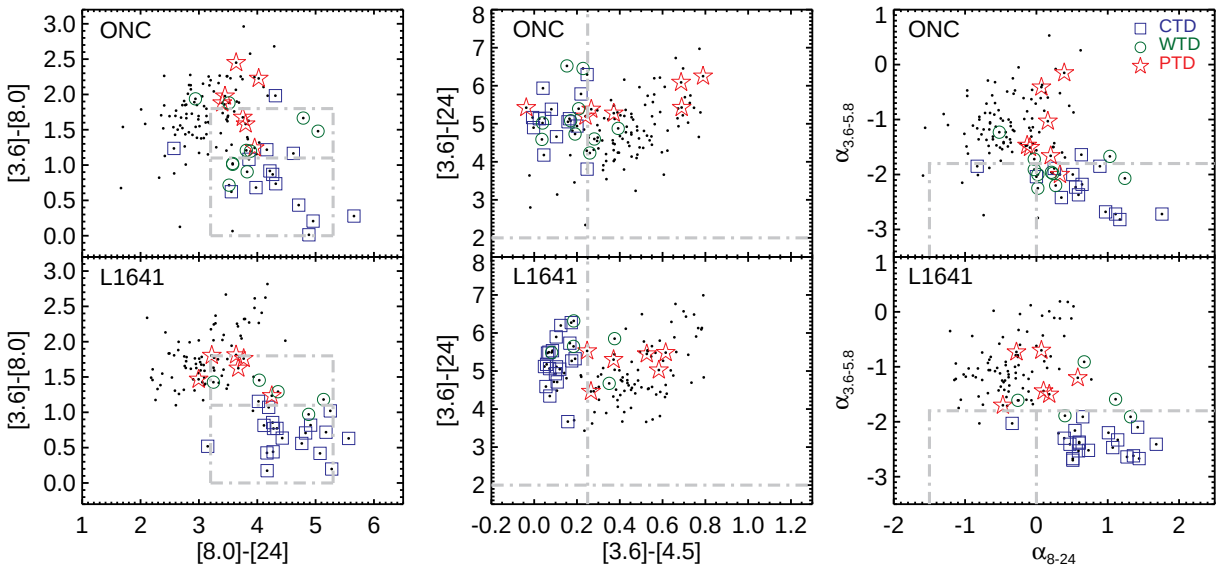

Fig. 10.— TDs of Orion A under other selection criteria. In each panel, the data points are our Orion A samples: the upper panels for ONC and the lower panels for L1641. Each selection criteria is indicated with the dot-dash lines. The left panel is for the selection criteria from Merín et al. (2010). The middle panel shows the selection criteria of Cieza et al. (2010). The right panel is the selection criteria from Muzerolle et al. (2010). (A color version of this figure is available in the online journal.)

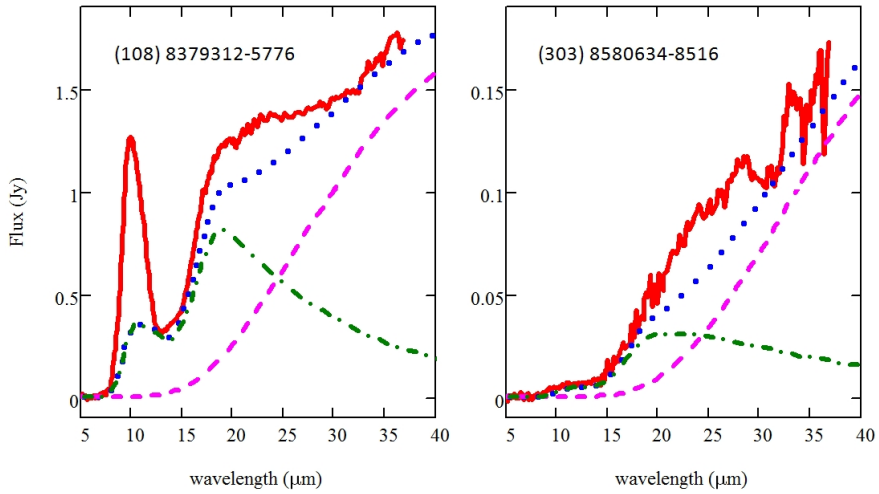

Fig. 11.— Example of fits using the simple model to estimate R_{wall} of transitional disks in Orion A and other star-forming regions included in this paper. The thick solid line: a residuum of IRS spectra after subtracting a power-law fitted to 5-8 μm of IRS spectra, representing emission from the photosphere or a part of the inner disk. The dash-dotted line: astronomical silicate model to account for some contribution of emission from small dust grains in the atmosphere of wall and disk upper layers. The dashed line: a single blackbody profile with the wall temperature T. The dotted line: the continuum fit as the combination of the dash-dotted line and the dashed line. (A color version of this figure is available in the online journal.)

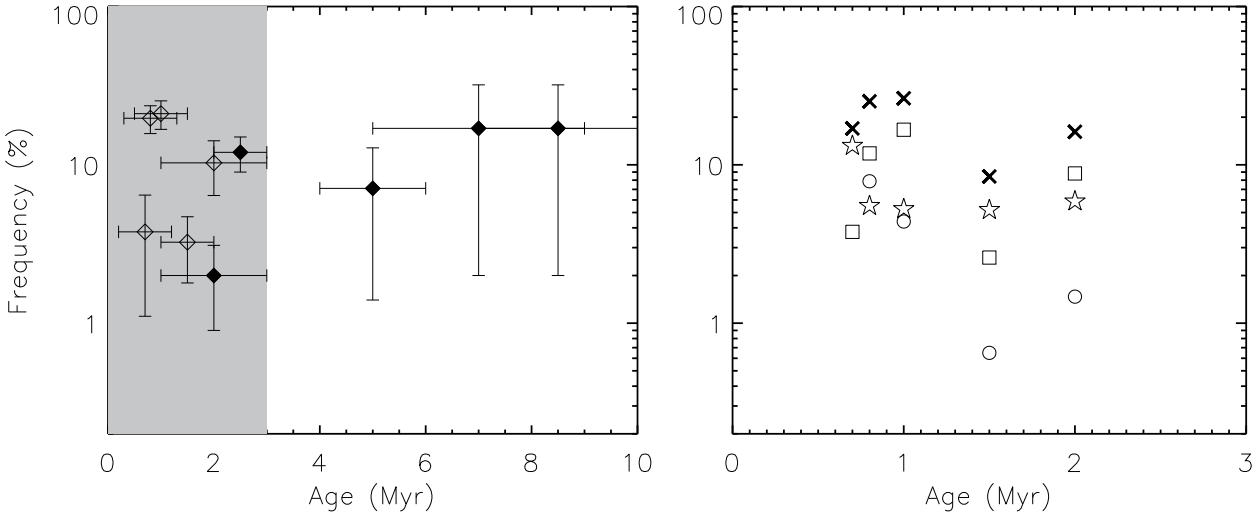

Fig. 12.— The fraction of transitional disks plotted against the estimated age of the association. The solid diamonds in the left panel are from the fraction of classical transitional disks defined by Muzerolle et al. (2010). The empty diamonds in the left panel are the fraction of CTD plus WTD from this work. The right panel is for the shaded region covering ages of 0-3 Myr in the left panel, and it shows fractions of TD (=CTDs+WTDs+PTDs) types in N1333, ONC, L1641, Tau, and ChaI from younger ages to older ages of star-forming regions. The symbols in the right panel indicate the TD fraction (cross), the CTD fraction (square), the WTD fraction (circle), and the PTD fraction (star).

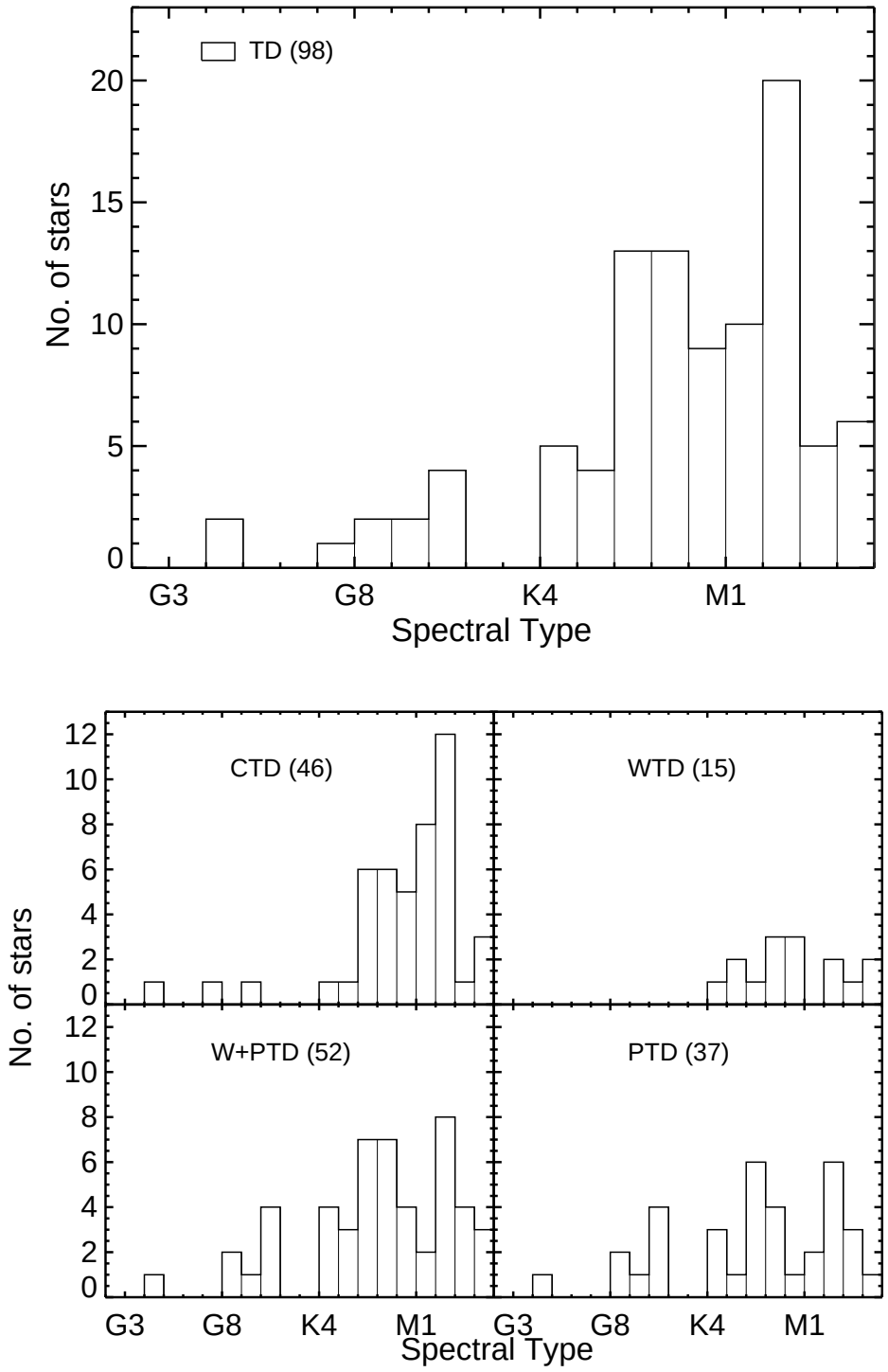

Fig. 13.— Spectral type distribution of transitional disks. The upper bigger panel shows the spectral type distribution of all TDs with known spectral types. The lower multiple panels show the spectral type distributions divided by TD subtypes. The results from K-S tests: (1) CTD vs. WTD: $D = 0.20$, $p = 0.69$; (2) WTD vs. PTD: $D = 0.32$, $p = 0.17$; (3) CTD vs. PTD: $D = 0.30$, $p = 0.04$; (4) CTD vs. WTD+PTD: $D = 0.24$, $p = 0.10$.

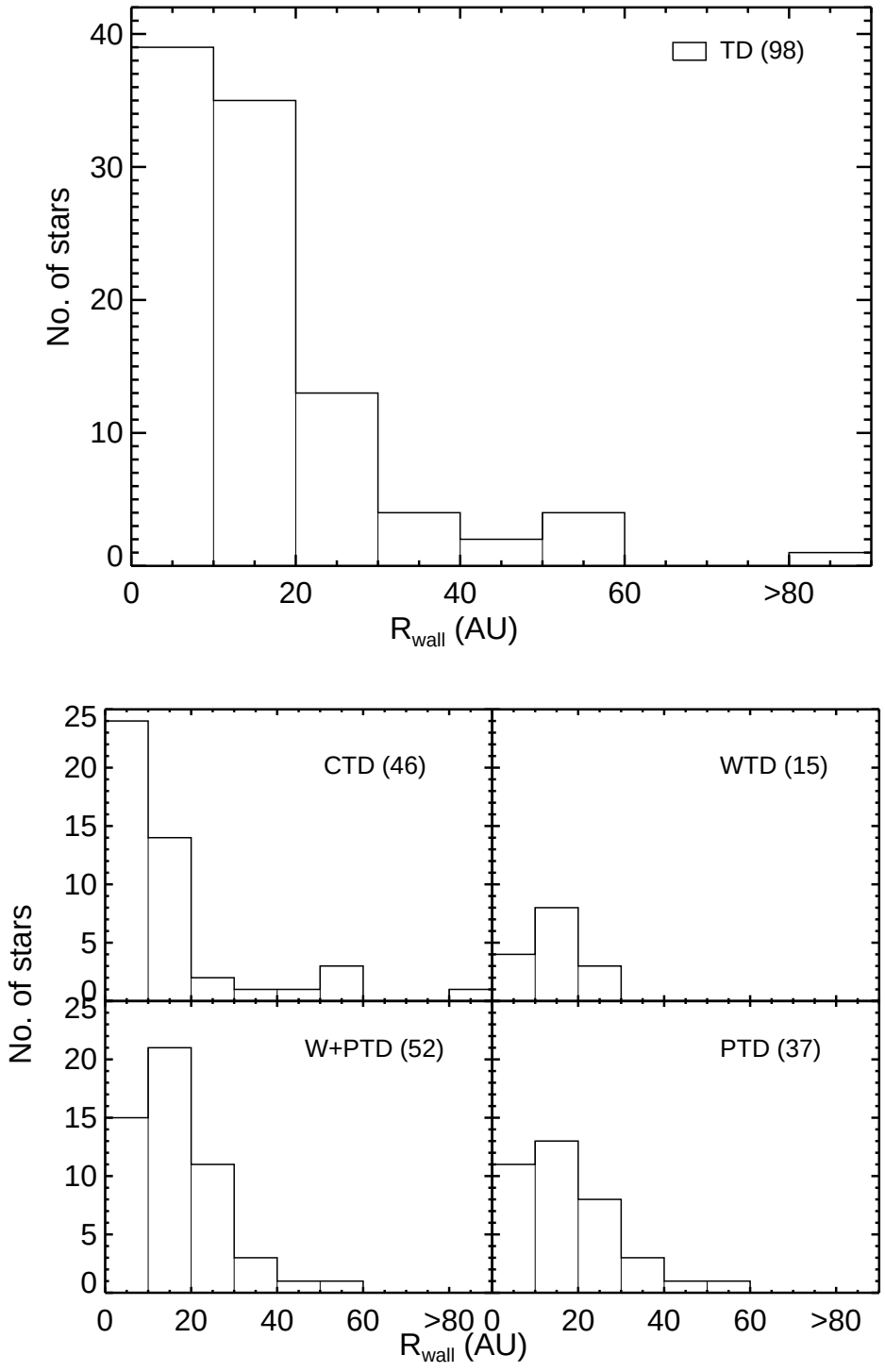

Fig. 14.— R_{wall} distribution of transitional disks. The upper bigger panel shows the R_{wall} distribution of all TDs with known spectral types. The lower multiple panels show the R_{wall} distributions divided by TD subtypes. The results from K-S tests: (1) CTD vs. WTD: $D = 0.32$, $p = 0.15$; (2) WTD vs. PTD: $D = 0.27$, $p = 0.36$; (3) CTD vs. PTD: $D = 0.29$, $p = 0.05$; (4) CTD vs. WTD+PTD: $D = 0.29$, $p = 0.02$.

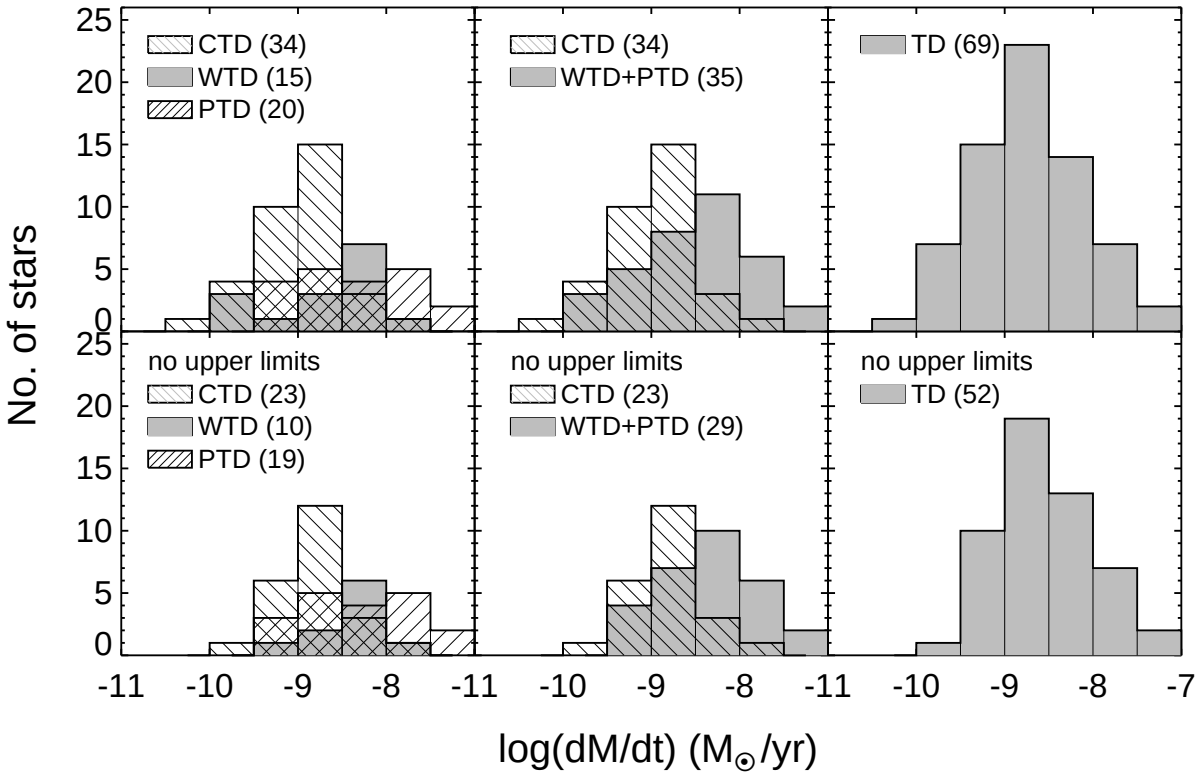

Fig. 15.— $\dot{M}$ distributions. The upper panels include upper limits of $\dot{M}$; the lower panels do not include upper limits of $\dot{M}$. The left panels show $\dot{M}$ distributions separated by three different TD types; the middle panels compare the $\dot{M}$ distribution of disks with central clearings (CTD) and to those with gaps (WTD and PTD); the right panels result from adding all types of TDs. The results of K-S tests of $\dot{M}$ distributions between CTD and WTD+PTD in the middle panels: $D = 0.46$, $p = 0.001$ (upper middle); $D = 0.5$, $p = 0.002$ (lower middle).

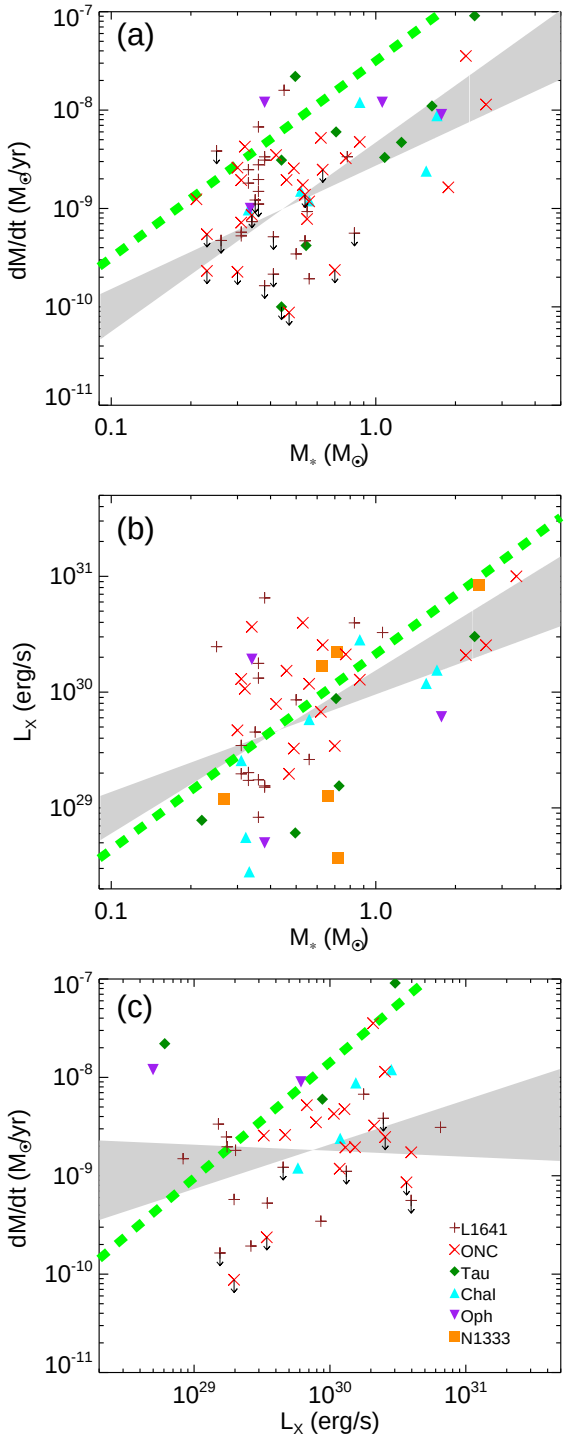

Fig. 16.— Trends among $M_\star$, $\dot{M}$ and L_X. In each plot, different symbols indicate TDs in different star-forming regions (plus: L1641; cross: ONC; solid diamond: Tau; solid triangle: ChaI; solid inverse-triangle: Oph; solid square: N1333). In each plot, the shaded area indicates the 1σ uncertainty of the linear regression (of the logarithms). If a shaded area is narrow with high slope (e.g., $\dot{M}$-$M_\star$), one can tell two properties in a panel is tightly correlated. If a shaded area is broad with very low slope (e.g., $\dot{M}$-L_X), two properties in a panel is not correlated. The thick dashed line indicates a correlation expected/observed among T Tau disks in Tau: $\dot{M} \propto {M_\star}^2$ from Muzerolle et al. (2003) in the upper panel; $L_X \propto {M_\star}^{1.69}$ from Telleschi et al. (2007) in the middle panel; $\dot{M} \propto {L_X}^{1.2}$ in the lower panel from above two relations. The down arrows indicate $\dot{M}$ upper limits. (A color version of this figure is available in the online journal.)

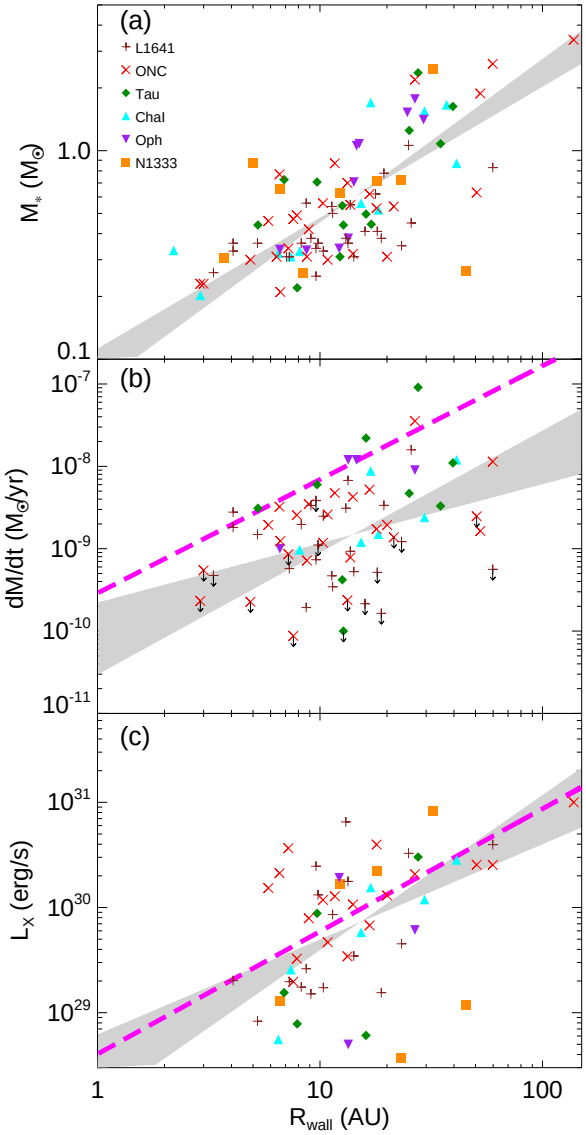

Fig. 17.— Trends related to R_{wall} with other stellar properties. Lines, shadow, and symbols have same meaning as in Figure 16. The thick long-dashed line indicates an expected trend derived from the relationship of a property in y-axis with $M_\star$ shown in Figure 16 and the strong $M_\star$-R_{wall} correlation shown in the panel (a): $\dot{M} \propto {R_{wall}}^{1.4}$ in the panel (b); $L_X \propto {R_{wall}}^{1.2}$ the panel (c). (A color version of this figure is available in the online journal.)

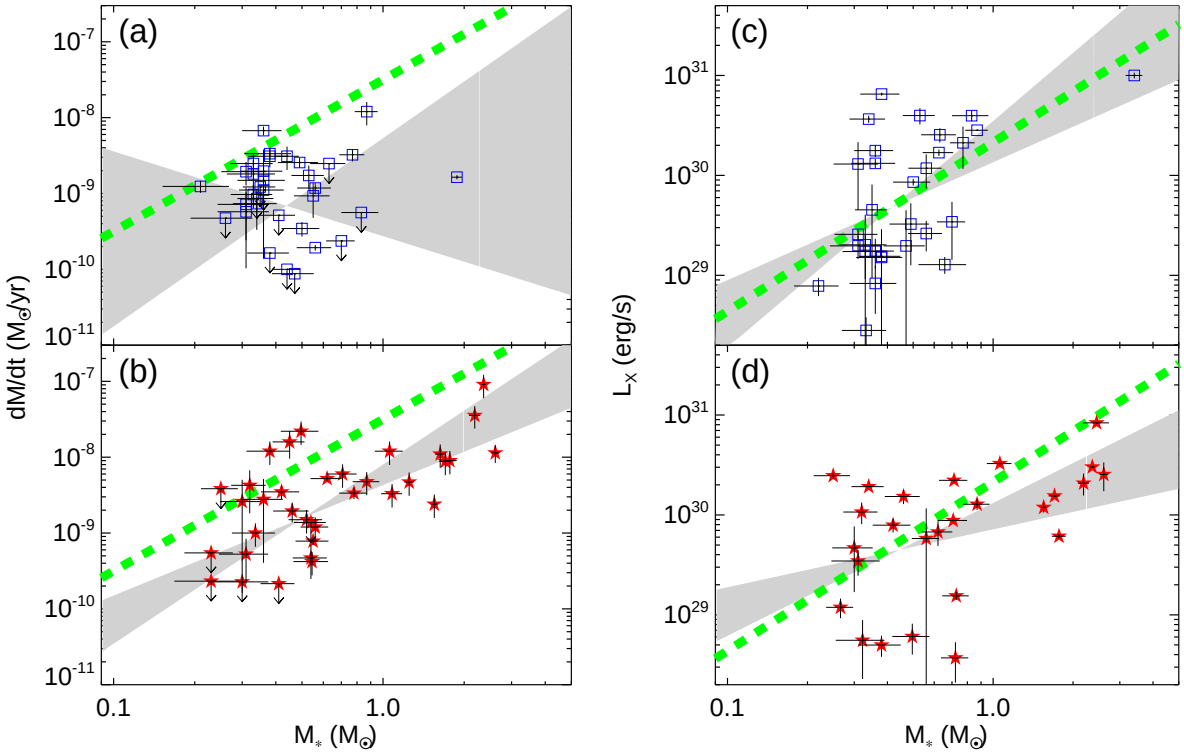

Fig. 18.— Detailed Trends of $\dot{M}$-$M_\star$ (the left panels) and L_X-$M_\star$ (the right panels) separated by subtypes of TDs. The upper panels (a and c) show the correlation of CTDs (open square). The lower panels (b and d) show the correlation of WTDs+PTDs (solid star). The meanings of lines and shade are same as defined in the caption of Figure 16. (A color version of this figure is available in the online journal.)

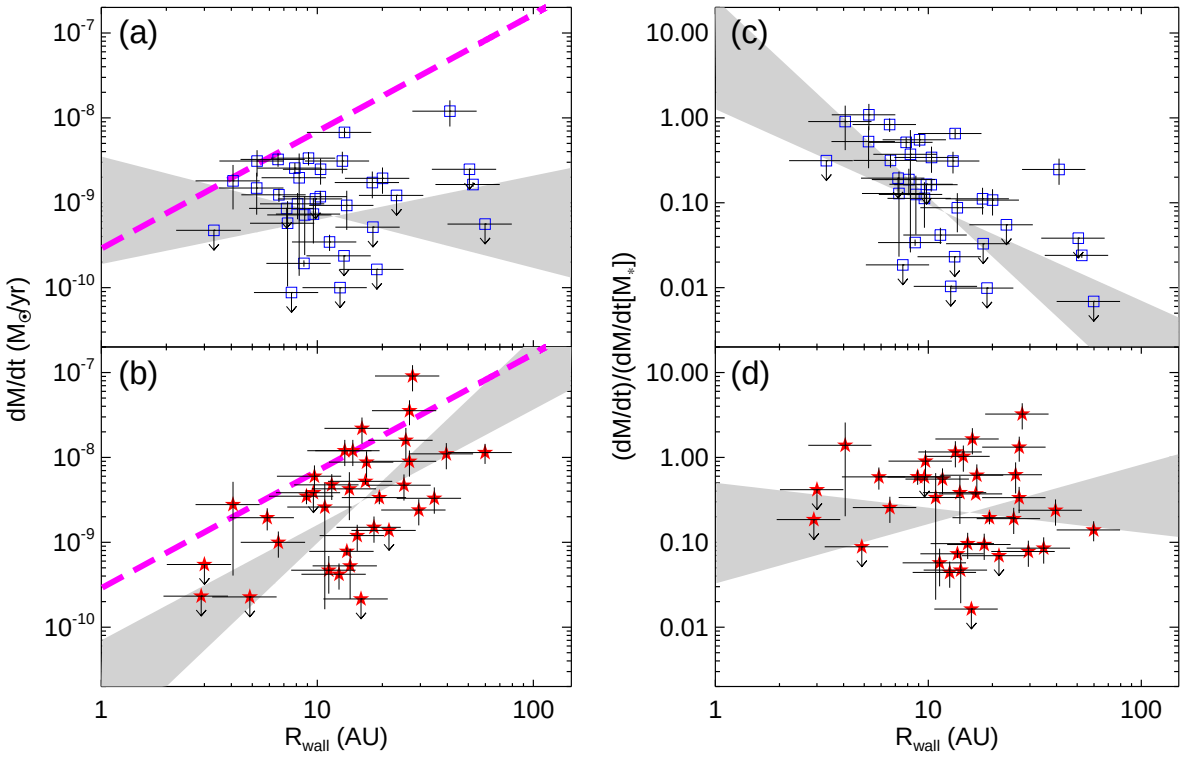

Fig. 19.— Detailed trends of $\dot{M}$-R_{wall}: correlations separated in two sub-groups, CTDs (open square) and WTDs+PTDs (solid star). The symbol in each panel is same as Figure 18. The thick long-dashed line in the panel (a) and (b) is same in Figure 17 (b). The right panels show the trend at no $M_\star$ dependence by presenting the deviation of $\dot{M}$ from the thick long-dashed line of $\dot{M}(M_\star)$-R_{wall}. (A color version of this figure is available in the online journal.)

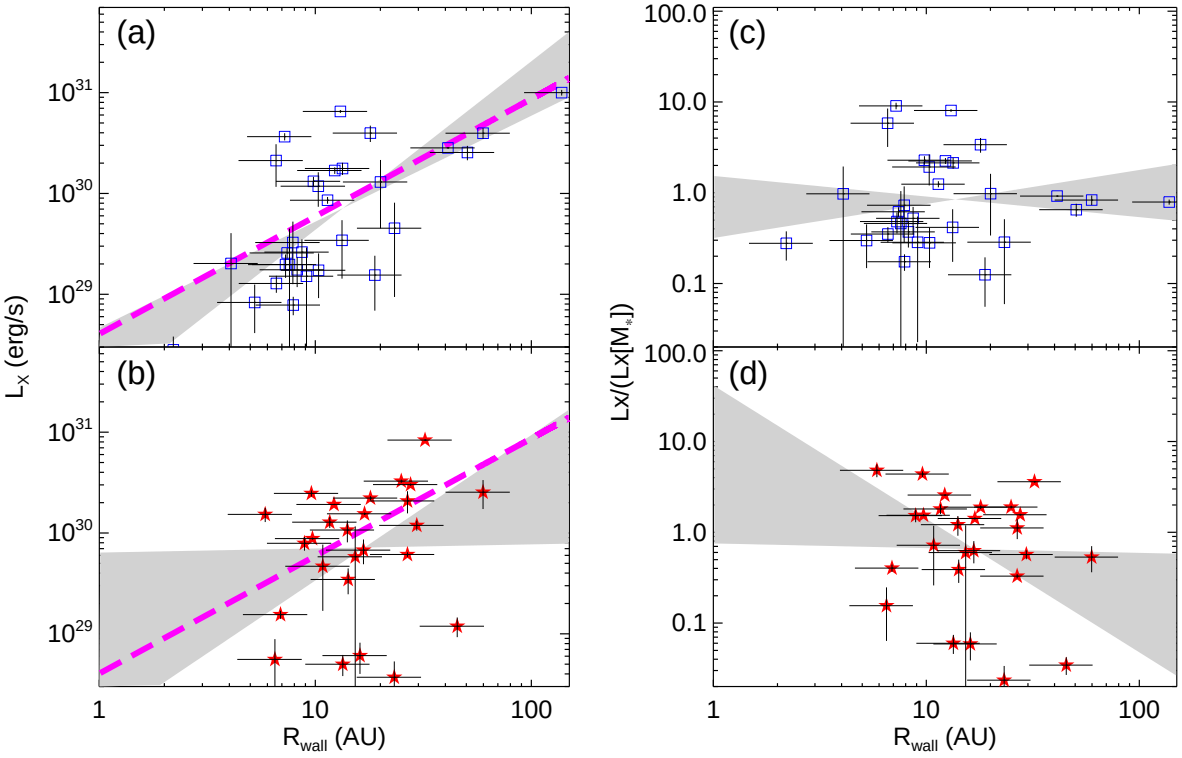

Fig. 20.— Detailed trends of L_X-R_{wall}: correlations separated in two sub-groups, CTDs (open square) and WTDs+PTDs (solid star). The symbol in each panel is same as in Figure 18. The thick long-dashed line in the panel (a) and (b) is same as in Figure 17 (c). The right panels show the trend at no $M_\star$ dependence by presenting the deviation of L_X from the thick long-dashed line of $L_X(M_\star)$-R_{wall}. (A color version of this figure is available in the online journal.)

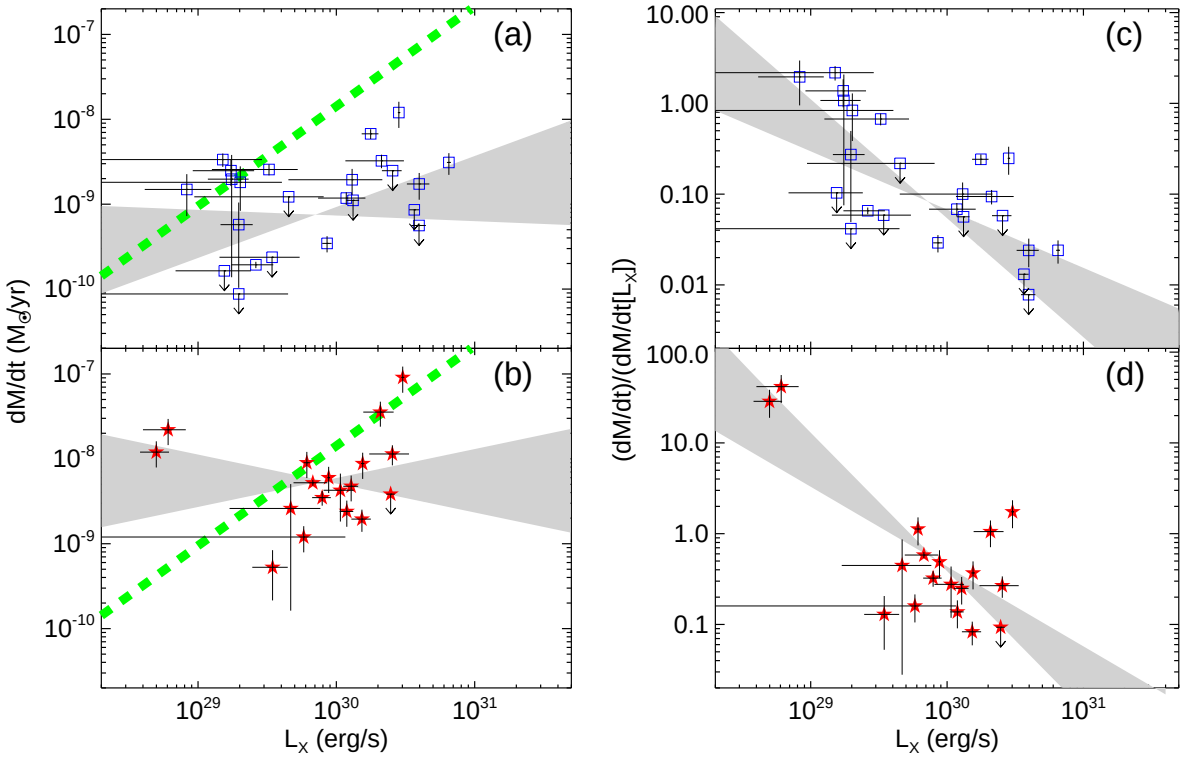

Fig. 21.— Detailed trends of $\dot{M}$-L_X: correlations separated in two sub-groups, CTDs (open square) and WTDs+PTDs (solid star). The symbol in each panel is same as in Figure 18. The thick dashed line represent $\dot{M}$-L_X relation of T Tauri star in Tau as explained in §6.2.1 and Figure 16. (A color version of this figure is available in the online journal.)

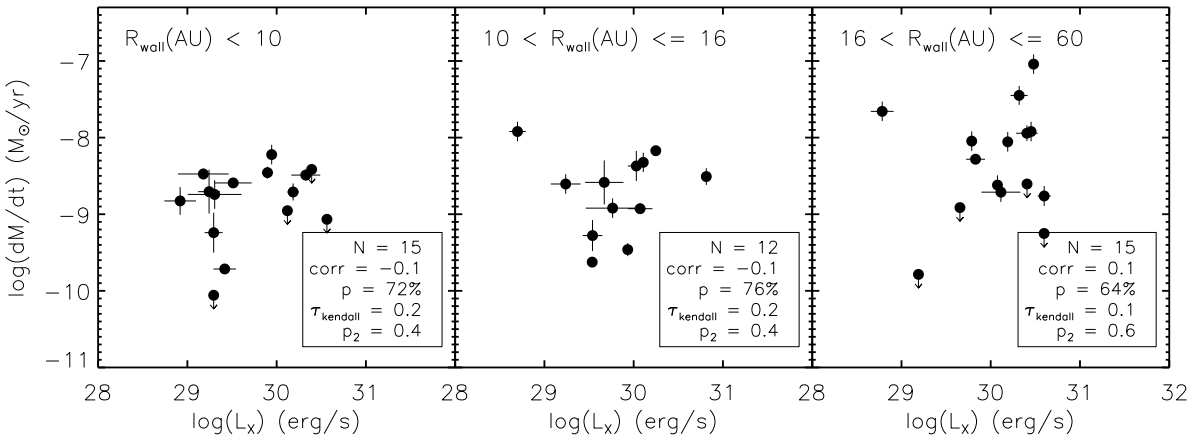

Fig. 22.— The tests to find the relationship between $\dot{M}$ and R_{wall} under a constant R_{wall} condition. We present the sub-groups separated by three R_{wall} bins. The coverage of R_{wall} of each bin is indicated on each panel with the number of sub-sample (N), a linear correlation coefficient (corr) between $log\dot{M}$ and $logL_X$, and a probability (p) of getting corr from random distribution. $\tau_{kentall}$ is Kendall's tau which indicates the degree of correlation between two variables; closer to 1, tighter correlation. p_2 indicate the two-sided p value of $\tau_{kentall}$; if p_2=1, the probability of no correlation is 100%.

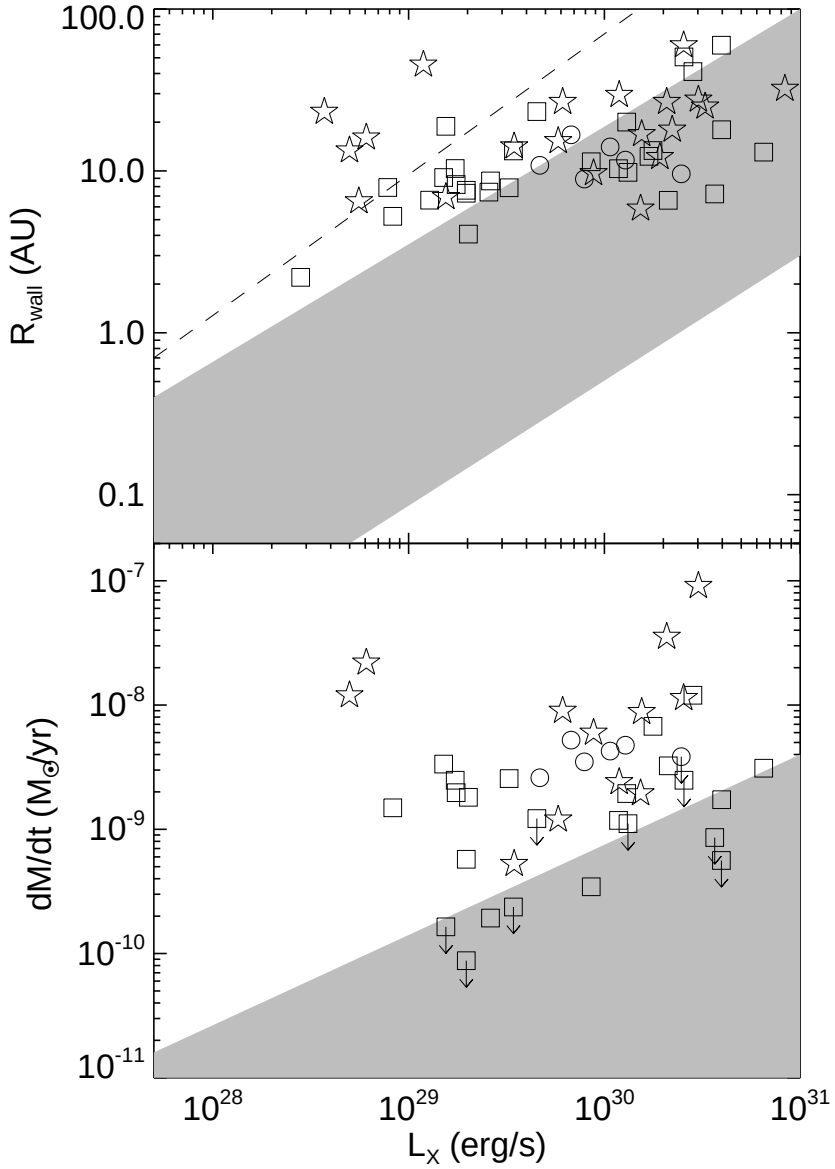

Fig. 23.— Comparison of the predictions by X-ray photoevaporation (Owen et al. (2012), Fig 18 in their paper) to the properties of observed TDs. The gray shadows are the domains in which X-ray photoevaporation is dominant. The dashed line adopted from Fig 18. in Owen et al. (2012) represents the maximum radius a TD may reach before thermal sweeping sets in and a disk dissipates beyond TD stage. The model domains are derived with $R_g \propto M_\star$ and the positive correlation between $M_\star$ and L_X (Owen et al. 2012), similar to our finding, so the photoevaporation prediction and the observed TDs properties generally show positive correlations.

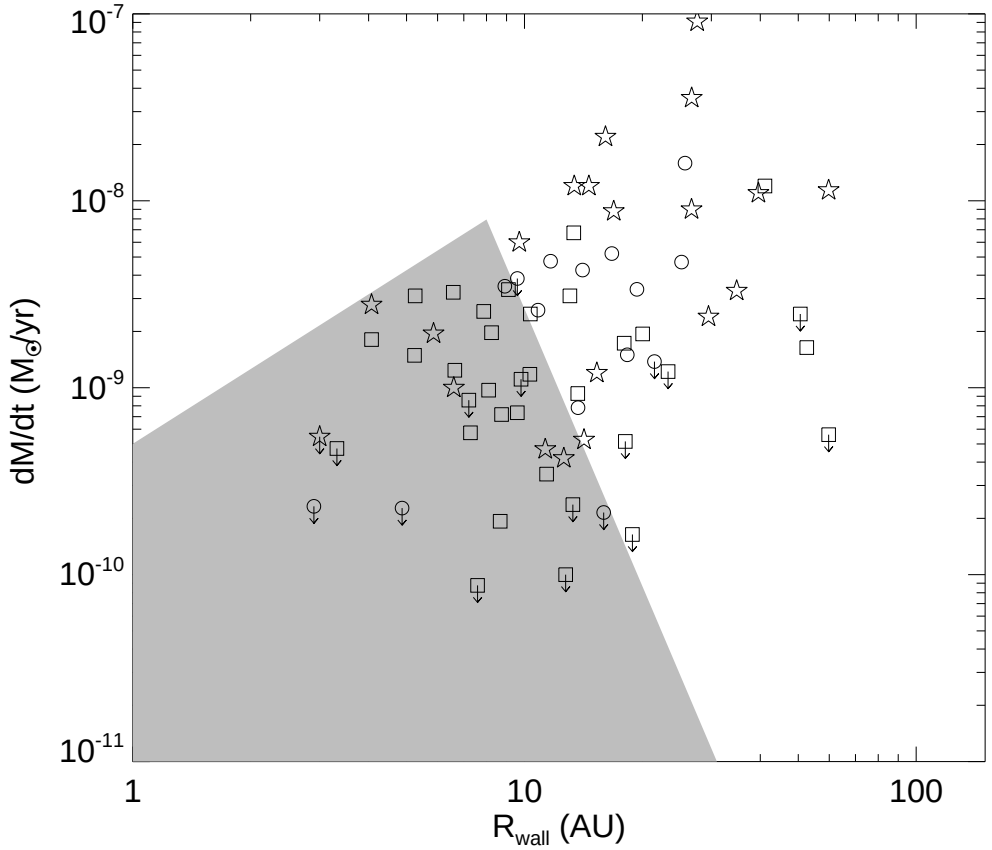

Fig. 24.— Comparison of $\dot{M}$ vs. R_{wall} to the predictions by X-ray photoevaporation (gray shadow region: Owen et al. (2012)). Each symbol indicate different subtype of TDs: square (CTD); circle (WTD); star (PTD).

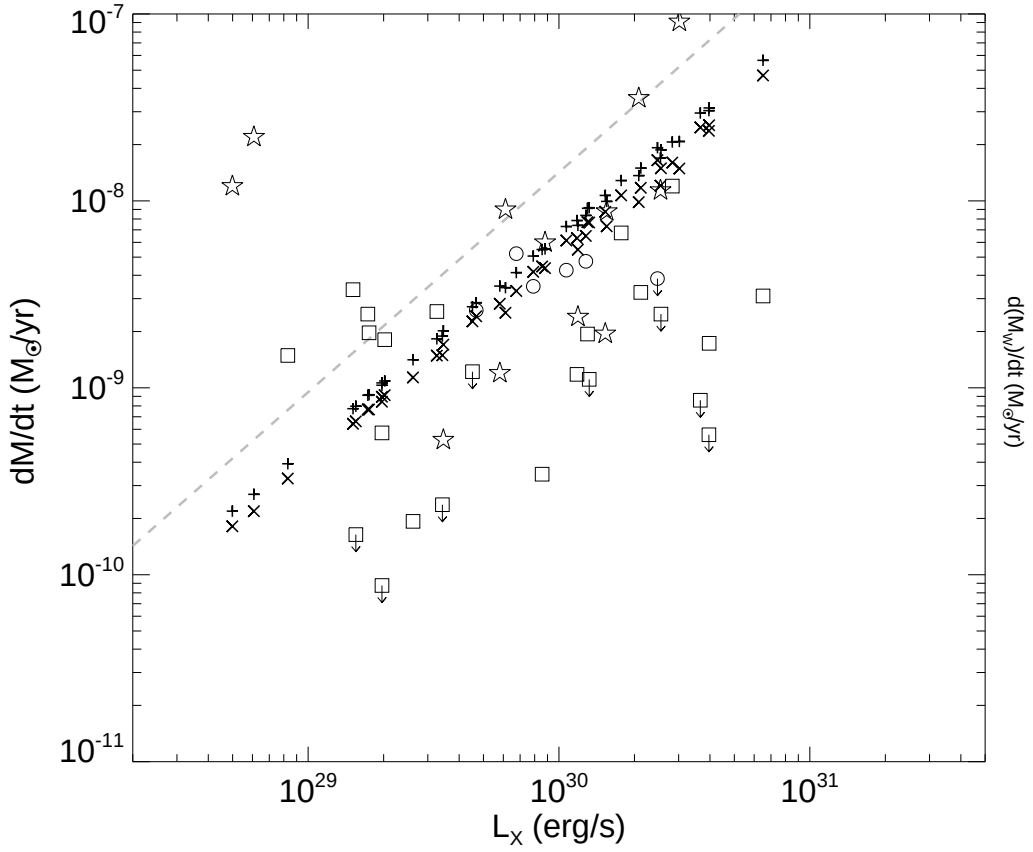

Fig. 25.— Comparison of $\dot{M}$ vs. L_X of transitional disks to M_W vs. L_X expected by the X-ray photoevaporation model (Owen et al. 2012). The plus signs are for the expected X-ray photoevaporation wind rates in case of a radially continuous primordial disk with TDs $M_\star$ and L_X, and the cross signs are for that in case of transitional disks with inner hole. The squares, circles, and stars are CTDs, WTDs, and PTDs of our sample. The gray dashed line indicate the expected $\dot{M}$-L_X of CTTS, which is derived from $\dot{M}$-$M_\star$ and $L_\star$-$M_\star$ of CTTS in Figure 16. Detail discussion is in Appendix B.

Table 1. Observation and reduction log of IRS spectra

Num. (1)	IRS name (2)	2MASS name (3)	RA (J2000) (4)	DEC (J2000) (5)	AORID (6)	IRS Camp. (7)	Date observed (8)	region (9)	reduction (10)
1	8336884-5290	05332852-0517262	05 33 28.52	-05 17 26.2	18804224	39	3/12/2007	ONC	AdOpt
5	8343944-5609	05334545-0536323	05 33 45.47	-05 36 32.5	18833152	39	3/12/2007	ONC	opse/AdOpt[a]
8	8346141-5010	05335074-0500394	05 33 50.74	-05 00 39.5	18781952	39	3/22/2007	ONC	AdOpt
11	8347711-5533	05335450-0532003	05 33 54.51	-05 32 00.4	18844416	39	3/12/2007	ONC	AdOpt
13	8350150-5595	05340034-0535434	05 34 00.36	-05 35 43.5	18778880	39	3/12/2007	ONC	man
16	8353051-5229	05340731-0513454	05 34 07.32	-05 13 45.1	18801408	39	3/22/2007	ONC	AdOpt
18	8355083-4835	05341221-0450072	05 34 12.20	-04 50 07.1	18810624	39	3/24/2007	ONC	AdOpt
19	8355371-5480	05341289-0528482	05 34 12.89	-05 28 48.3	18779904	44	10/5/2007	ONC	AdOpt/opse[b]
23	8357031-5072	05341687-0504210	05 34 16.88	-05 04 21.1	18836736	39	3/22/2007	ONC	man
24	8358147-5505	05341954-0530198	05 34 19.55	-05 30 19.8	18812928	39	3/24/2007	ONC	AdOpt
25	8358862-4842	05342125-0450326	05 34 21.27	-04 50 32.7	18776576	44	10/11/2007	ONC	AdOpt
26	8359203-5026	05342207-0501342	05 34 22.09	-05 01 34.2	18776320	39	3/22/2007	ONC	AdOpt
29	8361167-5475	05342679-0528321	05 34 26.80	-05 28 32.1	18778624	44	10/5/2007	ONC	AdOpt
34	8365722-4816	05343772-0448577	05 34 37.73	-04 48 57.9	18781440	44	10/11/2007	ONC	man
38	8367284-5798	05344146-0547561	05 34 41.48	-05 47 55.5	18838528	39	3/24/2007	ONC	AdOpt
39	8368137-4860	05344351-0451364	05 34 43.53	-04 51 36.3	18778368	44	10/5/2007	ONC	AdOpt
42	8369106-5686	05344587-0541097	05 34 45.86	-05 41 09.8	18840832	39	3/12/2007	ONC	AdOpt
44	8369980-5081	05344794-0504550	05 34 47.95	-05 04 54.9	18817792	39	3/22/2007	ONC	AdOpt
47	8371984-5465	05345275-0527545	05 34 52.76	-05 27 54.9	18843648	39	3/9/2007	ONC	AdOpt
53	8373930-6325	05345744-0619331	05 34 57.43	-06 19 33.0	18781696	39	3/9/2007	L1641	man
59	8374388-6000	05345852-0600004	05 34 58.53	-06 00 00.4	18820864	44	10/5/2007	L1641	man
66	8375158-5162	05350039-0509441	05 35 00.38	-05 09 44.0	18779648	44	10/5/2007	ONC	AdOpt
88	8377167-5247	05350519-0514503	05 35 05.20	-05 14 50.3	18802176	39	3/24/2007	ONC	AdOpt
108	8379312-5776	05351033-0546335	05 35 10.35	-05 46 33.8	18850560	39	3/12/2007	ONC	man
149	8385365-5106	05352486-0506216	05 35 24.88	-05 06 21.6	18798592	39	3/25/2007	ONC	AdOpt
154	8386523-5715	05352765-0542551	05 35 27.65	-05 42 55.1	18801664	39	3/12/2007	ONC	AdOpt
164	8387753-4993	05353060-0459360	05 35 30.61	-04 59 36.0	18835200	39	3/26/2007	ONC	opse/AdOpt[c]
169	8389033-4773	05353369-0446237	05 35 33.68	-04 46 23.5	18775040	39	3/24/2007	ONC	AdOpt
172	8389673-4794	05353522-0447396	05 35 35.21	-04 47 39.5	18810368	39	3/24/2007	ONC	man
174	8390073-5082	05353620-0504559	05 35 36.17	-05 04 56.0	18826752	39	3/26/2007	ONC	AdOpt
176	8390285-5070	05353668-0504145	05 35 36.68	-05 04 14.6	18815744	39	3/26/2007	ONC	AdOpt
177	8390554-6390	05353733-0623263	05 35 37.33	-06 23 26.2	18780928	39	3/12/2007	L1641	AdOpt
184	8394216-5181	05354612-0510517	05 35 46.12	-05 10 51.7	18825984	39	3/27/2007	ONC	AdOpt
185	8394454-5823	05354669-0549262	05 35 46.69	-05 49 26.1	18818048	39	3/25/2007	ONC	AdOpt

Table 1—Continued

Num. (1)	IRS name (2)	2MASS name (3)	RA (J2000) (4)	DEC (J2000) (5)	AORID (6)	IRS Camp. (7)	Date observed (8)	region (9)	reduction (10)
188	8396035-5861	05355047-0551422	05 35 50.48	-05 51 42.3	18838016	44	10/5/2007	ONC	AdOpt
198	8399269-6612	05355825-0636431	05 35 58.25	-06 36 43.2	18798336	39	3/12/2007	L1641	man
203	8406280-6293	05361506-0617369	05 36 15.07	-06 17 36.8	18845696	39	3/12/2007	L1641	AdOpt
204	8406609-6247	05361584-0614507	05 36 15.86	-06 14 50.6	18777088	39	3/12/2007	L1641	AdOpt
211	8411618-6426	05362788-0625360	05 36 27.88	-06 25 35.9	18780160	39	3/12/2007	L1641	man
218	8416389-6503	05363933-0630111	05 36 39.33	-06 30 11.3	18781184	39	3/12/2007	L1641	man
219	8416834-6225	05364039-0613334	05 36 40.40	-06 13 33.3	18775808	39	3/9/2007	L1641	man
221	8416978-6185	05364075-0611082	05 36 40.75	-06 11 08.2	18804992	39	3/11/2007	L1641	AdOpt
223	8424570-6484	05365897-0629049	05 36 58.97	-06 29 04.8	18780416	39	3/12/2007	L1641	AdOpt
227	8440418-7404	05373700-0724167	05 37 37.00	-07 24 16.6	18814464	39	3/9/2007	L1641	AdOpt/auto[d]
229	8444779-6608	05374746-0636298	05 37 47.47	-06 36 29.6	18776064	39	3/12/2007	L1641	AdOpt
230	8445558-6860	05374934-0651373	05 37 49.34	-06 51 37.3	18777600	44	10/6/2007	L1641	AdOpt
237	8457266-7161	05381743-0709395	05 38 17.44	-07 09 39.7	18831360	39	3/9/2007	L1641	man
239	8464666-7838	05383519-0750197	05 38 35.20	-07 50 19.7	18817536	39	3/9/2007	L1641	man
257	8502614-7795	05400626-0747445	05 40 06.27	-07 47 44.6	18779136	44	10/7/2007	L1641	man
260	8508501-7431	05402040-0725540	05 40 20.40	-07 25 54.2	18779392	44	10/7/2007	L1641	man
270	8519428-8120	05404661-0807128	05 40 46.63	-08 07 12.8	18821376	36	11/10/2006	L1641	man
271	8520557-7775	05404931-0746327	05 40 49.34	-07 46 32.6	18777856	44	10/7/2007	L1641	man
275	8535781-7830	05412586-0749506	05 41 25.87	-07 49 50.9	18806528	36	11/13/2006	L1641	man
279	8538911-7999	05413338-0759562	05 41 33.39	-07 59 56.5	18820352	36	11/13/2006	L1641	man
283	8547523-7831	05415405-0749534	05 41 54.05	-07 49 53.2	18777344	36	11/13/2006	L1641	man
290	8562845-8151	05423081-0809055	05 42 30.83	-08 09 05.5	18822912	36	11/13/2006	L1641	AdOpt
291	8564835-8250	05423560-0815020	05 42 35.60	-08 15 01.8	18775296	44	10/7/2007	L1641	man
294	8567670-8803	05424242-0848140	05 42 42.41	-08 48 13.8	18830336	36	11/9/2006	L1641	man
297	8570949-8577	05425027-0834378	05 42 50.28	-08 34 38.1	18782208	36	11/9/2006	L1641	man
301	8576836-8303	05430440-0818105	05 43 04.41	-08 18 11.0	18850304	36	11/15/2006	L1641	man
302	8579480-8565	NA	05 43 10.75	-08 33 55.2	18775552	36	11/9/2006	L1641	man
303	8580634-8516	05431353-0831004	05 43 13.52	-08 31 00.0	18776832	39	3/12/2007	L1641	man

Note. — Column (1) Num.: the numbers are from the number sequence of 303 Class II objects observed in the IRS program number 30706. We use these numbers to identify objects easily. This number sequence will be used consistently in other future papers dealing with the objects in the PID 30706.
Column (2) IRS name: sometimes IRS name indicated as in the column used to identify objects.

Column (10) reduction: it indicate the methods of source extraction to get the SEDs in Figure 2. auto: an automated tapered column extraction in SMART with off-nod or off-order sky subtraction; man: a manual tapered column extraction in SMART with a polynomial sky subtraction; AdOpt: an optimal source extraction using an empirical point response function (PRF) in SMART; opse: an optimal source extraction using an analytical PRF.

[a]SL & LL1: opsew7p; LL2: AdOpt.

[b]SL: AdOpt; LL: opse.

[c]SL: opse, LL:AdOpt.

[d]SL: AdOpt; LL:auto onss.

Table 2. Observation log of SpeX spectra

Num.	IRS name	obs. semester	obs. date (UT)	slit width (")	total int. time (sec)	comment
1	8336884-5290	2011B	11/6/2011	0.5	480	
5	8343944-5609	2011A	2/28/2011	0.8	400	
11	8347711-5533	2010A	2/18/2010	0.8	480	
13	8350150-5595	2010A	2/17/2010	0.8	480	
16	8353051-5229	2010A	2/18/2010	0.8	240	
19	8355371-5480	2010A	2/17/2010	0.8	720	a
23	8357031-5072	2011B	11/7/2011	0.8	240	
24	8358147-5505	2011A	2/27/2011	0.8	240	
25	8358862-4842	2010A	2/16/2010	0.5	480	a
26	8359203-5026	2011B	11/10/2011	0.8	480	b, c
29	8361167-5475	2010A	2/18/2010	0.8	480	
34	8365722-4816	2010A	2/16/2010	0.3	2520	
38	8367284-5798	2010A	2/18/2010	0.8	240	b, d
39	8368137-4860	2011B	11/6/2011	0.5	480	
42	8369106-5686	2011B	11/6/2011	0.5	720	e
44	8369980-5081	2010A	2/16/2010	0.5	240	
47	8371984-5465	2011B	11/7/2011	0.8	480	b, f
59	8374388-6000	2010A	2/17/2010	0.8	480	
66	8375158-5162	2010A	2/16/2010	0.5	960	
88	8377167-5247	2011A	2/26/2011	0.8	120	
108	8379312-5776	2010A	2/16/2010	0.5	240	
154	8386523-5715	2011A	2/28/2011	0.8	320	
169	8389033-4773	2010A	2/17/2010	0.8	480	
172	8389673-4794	2010A	2/17/2010	0.8	480	
176	8390285-5070	2011B	11/10/2011	0.8	240	
177	8390554-6390	2010A	2/16/2010	0.5	240	
184	8394216-5181	2011B	11/10/2011	0.8	400	
185	8394454-5823	2010A	2/16/2010	0.5	240	
198	8399269-6612	2011A	2/28/2011	0.8	240	
204	8406609-6247	2011A	2/28/2011	0.8	960	
211	8411618-6426	2011B	11/10/2011	0.8	240	
218	8416389-6503	2010A	2/16/2010	0.5	480	
219	8416834-6225	2010A	2/17/2010	0.8	480	
223	8424570-6484	2011A	2/26/2011	0.8	960	
227	8440418-7404	2011A	2/28/2011	0.8	360	
229	8444779-6608	2010A	2/16/2010	0.5	240	
230	8445558-6860	2010A	2/18/2010	0.8	720	
237	8457266-7161	2010A	2/17/2010	0.8	480	
239	8464666-7838	2010A	2/18/2010	0.8	240	
257	8502614-7795	2010A	2/17/2010	0.8	480	
260	8508501-7431	2010A	2/17/2010	0.8	240	
270	8519428-8120	2010A	2/18/2010	0.8	240	
271	8520557-7775	2010A	2/18/2010	0.8	960	g
275	8535781-7830	2010A	2/17/2010	0.8	240	
279	8538911-7999	2010A	2/17/2010	0.8	960	

Table 2—Continued

Num.	IRS name	obs. semester	obs. date (UT)	slit width (")	total int. time (sec)	comment
283	8547523-7831	2010A	2/17/2010	0.8	240	
290	8562845-8151	2011A	2/28/2011	0.8	480	a, b, h
291	8564835-8250	2010A	2/17/2010	0.8	480	
294	8567670-8803	2010A	2/18/2010	0.8	240	
301	8576836-8303	2011A	2/28/2011	0.8	480	
302	8579480-8565	2010A	2/18/2010	0.8	240	
303	8580634-8516	2010A	2/18/2010	0.8	960	g

Note. — (a) The source signal on order 8 is very faint, so that order 8 source extraction failed.; (b) It is a binary system with two sources resolved from SpeX observations. The possible primary source giving the adopted $\dot{M}$ in Table 4 is presented in the black line from 0.8-2.4 μm in Figure 2. The possible secondary is presented in the gray line in the same plot.; (c) The position angle of slit was 27°.; (d) Resolved two sources on the guider image are dominantly displaced in the north-south direction with slight separation in east-west direction.; (e) 4 among 6×120 sec exposures are combined in the spectrum.; (f) The two sources are aligned to N-S direction.; (g) The source signals in orders 6,7, and 8 is very faint so that source extraction for order 6-8 failed.; (h) The position angle of slit was -20°.

Table 3. Spectral Type and Extinction

Num. (1)	IRS name (2)	Spectral type (3)	SpT reference (4)	A_V (5)	A_V method (6)
1	8336884-5290	M0.0	f	0.61	I-J
5	8343944-5609	M5.5	c,f	0.87	I-J
8	8346141-5010	M3.5	f	0.33	I-J
11	8347711-5533	K7.0	SpeX	8.27	H-K
13	8350150-5595	M3.5	c	0	I-J
16	8353051-5229	K1.0	SpeX	3.01	J-H
18	8355083-4835	···	···	1	CTTS J-H
19	8355371-5480	K7.0	b	0.15	H-K
23	8357031-5072	M0.0	f	1.88	J-H
24	8358147-5505	K1.0	c	4.21	J-H
25	8358862-4842	M3.5	f	1.62	CTTS J-H
26	8359203-5026	M5.5	f	0.28	I-J
29	8361167-5475	M0.0	SpeX	0.73	I-J
34	8365722-4816	M1.0	SpeX	1.51	I-J
38	8367284-5798	M0.0	c	1.1	I-J
39	8368137-4860	M3.5	f	0.65	I-J
42	8369106-5686	M4.0	f	1	I-J
44	8369980-5081	M1.0	f	0.71	I-J
47	8371984-5465	K7.5	f	4.68	H-K
53	8373930-6325	M3.5	a	0.24	I-J
59	8374388-6000	M2.5	f	0.28	I-J
66	8375158-5162	M5.0	f	0.22	J-H
88	8377167-5247	G5.0	b	2.57	J-H
108	8379312-5776	K0.0	e	1.82	I-J
149	8385365-5106	···	···	21.3	CTTS J-H
154	8386523-5715	M3.5	g,i′	2.28	H-K
164	8387753-4993	···	···	14.7	CTTS J-H
169	8389033-4773	M0.5	f	1.9	H-K
172	8389673-4794	M3.0	f	2.03	J-H
174	8390073-5082	···	···	8.42	CTTS J-H
176	8390285-5070	M1.5	f	0.79	I-J
177	8390554-6390	M2.5	a	0.12	H-K
184	8394216-5181	K7.5	f	1.79	J-H
185	8394454-5823	K6.0	e	1.57	J-H
188	8396035-5861	···	···	0.64	CTTS J-H
198	8399269-6612	K6.5	a	2.17	J-H
203	8406280-6293	K5.0	d,i	0.68	CTTS J-H
204	8406609-6247	M2.5	d,f,h	0.73	I-J
211	8411618-6426	M3.5	a,f,h	0.53	I-J
218	8416389-6503	M4.5	a,f	0.23	I-J
219	8416834-6225	M0.5	e,f	0.68	I-J
221	8416978-6185	K7.5	a	11.8	H-K
223	8424570-6484	M3.0	e	0.9	I-J
227	8440418-7404	M0.0	a	5.53	CTTS J-H
229	8444779-6608	M0.0	e	3.5	H-K

Table 3—Continued

Num. (1)	IRS name (2)	Spectral type (3)	SpT reference (4)	A_V (5)	A_V method (6)
230	8445558-6860	M0.0	a′, SpeX	2.42	CTTS J-H
237	8457266-7161	M1.5	e	4.59	J-H
239	8464666-7838	M1.0	a	0.39	H-K
257	8502614-7795	M3.0	a	0.63	I-J
260	8508501-7431	M2.0	a	1.17	I-J
270	8519428-8120	K7.0	d,h	9.53	H-K
271	8520557-7775	M2.0	a′, SpeX	6.11	H-K
275	8535781-7830	M5.0	e	4.06	H-K
279	8538911-7999	M1.5	h	7.98	H-K
283	8547523-7831	M2.0	e	1.41	J-H
290	8562845-8151	M2.5	a	2.92	I-J
291	8564835-8250	M2.5	a	2.81	J-H
294	8567670-8803	M2.5	a′, SpeX	7.42	H-K
297	8570949-8577	···	···	19.9	CTTS H-K
301	8576836-8303	M3.5	a	3.16	CTTS J-H
302	8579480-8565	M	SpeX	3.41	CTTS J-H
303	8580634-8516	M3.0	a,e	6.56	H-K

Note. — Spectral type (column 3) and the methods or literature (column 4) from which we adopted the spectral type

[a]Allen & Mosby (2008), private communication; spectral types are measured from HECTOSPEC spectra

[a′]Allen & Mosby (2008), private communication; spectral types are measured from HECTOSPEC spectra, spectral types are highly uncertain

[b]Hillenbrand (1997b)

[c]Rebull et al. (2000)

[d]Allen (1995)

[e]Hernandez (2008), private communication; spectral types measured from MDM spectroscopic data

[f]Hernandez & Tobin (2009), private communication; spectral types are measured from HECTOSPEC spectra

[f′]Hernandez & Tobin (2009); spectral types are measured from FAST spectra.

[g]Da Rio et al. (2010)

[h]Fang et al. (2009)

[i]Parihar et al. (2009)

[i′]It is M3.6 from Parihar et al. (2009), but for our analysis convenience we take it as M3.5

[SpeX]Spectral typing with SpeX spectra in this work

Note. — Column (6) A_V method: the method which derived A_V in the column (5). See the text for details.

Table 4. Stellar and Disk properties

Num	IRS name	T_{eff} (K)	$L_\star$ ($L_\odot$)	$M_\star$ ($M_\odot$)	R_{wall} (AU)	TD type	$\dot{M}$ ($M_\odot/yr$)	L_X (erg/s)	region
1	8336884-5290	3850	0.64	0.55	13.7	WTD	(7.8±0.9)E-10	···	ONC
5	8343944-5609	3145	0.54	0.23	3.0	PTD	<5.5E-10	···	ONC
8	8346141-5010	3420	0.17	0.31	6.4	CTD	···	···	ONC
11	8347711-5533	4060	1.80	0.70	13.3	CTD	<2.37E-10	(3.4±2.0)E+29	ONC
13	8350150-5595	3420	0.45	0.31	20.0	CTD	(1.9±0.7)E-09	(1.3±0.9)E+30	ONC
16	8353051-5229	5080	3.65	1.88	52.6	CTD	(1.6±0.1)E-09	···	ONC
18	8355083-4835	3850	0.18	0.58	3.0	PTD	···	···	ONC
19	8355371-5480	4060	0.50	0.77	6.6	CTD	(3.2±0.6)E-09	(2.1±1.0)E+30	ONC
23	8357031-5072	3850	1.32	0.54	21.5	WTD	<1.38E-09	···	ONC
24	8358147-5505	5080	5.98	2.19	26.7	PTD	(3.6±1.2)E-08	(2.1±0.5)E+30	ONC
25	8358862-4842	3420	0.14	0.30	4.9	WTD	<2.3E-10	···	ONC
26	8359203-5026	3145	0.17	0.21	6.6	CTD	(1.2±0.2)E-09	···	ONC
29	8361167-5475	3850	0.41	0.56	10.3	CTD	(1.2±0.2)E-09	(1.2±0.4)E+30	ONC
34	8365722-4816	3720	0.25	0.47	7.6	CTD	<8.8E-11	(2.0±2.5)E+29	ONC
38	8367284-5798	3850	1.46	0.53	18.0	CTD	(1.7±0.6)E-09	(4.0±0.7)E+30	ONC
39	8368137-4860	3420	0.26	0.31	8.7	CTD	(7.2±4.8)E-10	···	ONC
42	8369106-5686	3370	0.49	0.30	10.8	WTD	(2.6±2.4)E-09	(4.7±3.0)E+29	ONC
44	8369980-5081	3720	0.60	1.21	5.9	PTD	(2.0±0.6)E-09	(1.5±0.2)E+30	ONC
47	8371984-5465	3955	4.37	0.63	50.6	CTD	<2.5E-09	(2.6±0.4)E+30	ONC
53	8373930-6325	3420	0.17	0.31	7.1	CTD	···	···	L1641
59	8374388-6000	3525	0.66	0.36	13.4	CTD	(6.7±0.9)E-09	(1.8±0.2)E+30	L1641
66	8375158-5162	3240	0.10	0.23	2.9	WTD	<2.3E-10	···	ONC
88	8377167-5247	5770	62.34	3.40	138.2	CTD	···	(1.0±0.1)E+31	ONC
108	8379312-5776	5250	11.16	2.01	59.8	PTD	(1.1±0.3)E-08	(2.5±0.8)E+30	ONC
149	8385365-5106	3850	7.40	0.60	61.2	PTD	···	···	ONC
154	8386523-5715	3420	0.86	0.32	14.1	WTD	(4.3±2.4)E-09	(1.1±0.3)E+30	ONC
164	8387753-4993	3850	5.02	0.56	18.5	PTD	···	(3.3±1.4)E+29	ONC
169	8389033-4773	3785	0.81	0.49	7.9	CTD	(2.6±0.4)E-09	(3.3±2.0)E+29	ONC
172	8389673-4794	3470	0.62	0.34	7.2	CTD	<8.58E-10	(3.7±0.3)E+30	ONC
174	8390073-5082	3850	2.11	0.53	11.5	CTD	···	···	ONC
176	8390285-5070	3650	0.71	0.42	8.9	WTD	(3.5±0.7)E-09	(7.9±1.2)E+29	ONC
177	8390554-6390	3525	0.30	0.36	9.8	CTD	<1.1E-09	(1.3±0.1)E+30	L1641
184	8394216-5181	3955	1.12	0.62	16.7	WTD	(5.2±0.4)E-09	(6.8±1.9)E+29	ONC
185	8394454-5823	4205	1.30	0.87	11.7	WTD	(4.8±1.6)E-09	(1.3±0.2)E+30	ONC
188	8396035-5861	3850	1.19	0.54	9.3	WTD	···	(2.3±0.1)E+30	ONC
198	8399269-6612	4132	1.33	0.78	19.4	WTD	(3.4±0.6)E-09	···	L1641
203	8406280-6293	4350	1.46	1.06	25.0	PTD	···	(3.3±0.1)E+30	L1641
204	8406609-6247	3525	0.23	0.36	5.2	CTD	(1.5±0.8)E-09	(8.3±4.2)E+28	L1641
211	8411618-6426	3420	0.23	0.31	7.3	CTD	(5.7±4.7)E-10	(2.0±0.5)E+29	L1641
218	8416389-6503	3305	0.14	0.26	3.3	CTD	<4.73E-10	···	L1641
219	8416834-6225	3785	0.50	0.50	11.4	CTD	(3.5±0.7)E-10	(8.6±0.7)E+29	L1641
221	8416978-6185	3955	1.12	0.62	17.8	PTD	···	···	L1641
223	8424570-6484	3470	0.34	0.34	9.6	CTD	(7.4±4.0)E-10	···	L1641
227	8440418-7404	3850	0.81	0.54	11.3	PTD	(4.7±2.2)E-10	···	L1641
229	8444779-6608	3850	0.61	0.55	13.7	CTD	(9.3±4.5)E-10	···	L1641

Table 4—Continued

Num	IRS name	T_{eff} (K)	$L_\star$ ($L_\odot$)	$M_\star$ ($M_\odot$)	R_{wall} (AU)	TD type	$\dot{M}$ ($M_\odot/yr$)	L_X (erg/s)	region
230	8445558-6860	3850	0.46	0.56	8.7	CTD	(1.9±0.2)E-10	(2.6±0.9)E+29	L1641
237	8457266-7161	3650	1.26	0.41	18.1	CTD	<5.16E-10	···	L1641
239	8464666-7838	3720	1.81	0.45	25.7	WTD	(1.6±0.6)E-08	···	L1641
257	8502614-7795	3470	0.23	0.33	4.1	CTD	(1.8±1.0)E-09	(2.0±2.0)E+29	L1641
260	8508501-7431	3580	0.36	0.38	9.1	CTD	(3.4±0.6)E-09	(1.5±1.4)E+29	L1641
270	8519428-8120	4060	9.78	0.83	59.8	CTD	<5.61E-10	(4.0±0.5)E+30	L1641
271	8520557-7775	3580	0.47	0.38	18.9	CTD	<1.64E-10	(1.6±0.9)E+29	L1641
275	8535781-7830	3240	0.85	0.25	9.6	WTD	<3.84E-09	(2.5±0.2)E+30	L1641
279	8538911-7999	3650	1.06	0.41	15.9	WTD	<2.15E-10	···	L1641
283	8547523-7831	3580	0.58	0.38	13.1	CTD	(3.1±0.9)E-09	(6.5±0.2)E+30	L1641
290	8562845-8151	3525	0.40	0.36	4.1	PTD	(2.8±2.4)E-09	···	L1641
291	8564835-8250	3525	0.43	0.36	8.2	CTD	(2.0±2.8)E-09	(1.8±0.6)E+29	L1641
294	8567670-8803	3525	2.00	0.35	23.3	CTD	<1.22E-09	(4.5±3.6)E+29	L1641
297	8570949-8577	3850	1.75	0.53	22.7	PTD	···	···	L1641
301	8576836-8303	3420	0.38	0.31	14.2	PTD	(5.3±3.1)E-10	(3.5±1.0)E+29	L1641
302	8579480-8565	3850	0.20	0.58	6.7	WTD	(5.3±1.7)E-10	···	L1641
303	8580634-8516	3470	0.43	0.33	10.4	CTD	(2.9±0.8)E-09	(1.7±0.8)E+29	L1641
.	04202606	3420	0.19	0.31	12.3	PTD	···	···	Tau
.	04125+2902	3685	0.36	0.44	17.0	CTD	···	···	Tau
.	CoKuTau4	3650	0.60	0.44	9.4	CTD	<1.0E-10[a]	···	Tau
.	DMTau	3720	0.20	0.44	3.9	CTD	(3.1±1.1)E-09[b]	···	Tau
.	GKTau	4060	1.37	0.71	9.7	PTD	(6.0±2.1)E-09[c]	(8.8±0.2)E+29	Tau
.	GMAur	4350	1.00	1.25	26.9	WTD	(4.7±1.6)E-09[b]	···	Tau
.	HKTau	3785	0.65	0.50	16.1	PTD	(2.2±0.8)E-08[c]	(6.1±2.1)E+28	Tau
.	IPTau	3850	0.69	0.55	12.6	PTD	(4.2±1.4)E-10[b]	···	Tau
.	LkCa15	4350	1.00	1.08	47.6	PTD	(3.3±1.1)E-09[b]	···	Tau
.	MHO3	4060	0.87	0.73	6.9	PTD	···	(1.6±0.1)E+29	Tau
.	RYTau	5945	19.75	2.36	27.6	PTD	(9.1±3.1)E-08[b]	(3.0±0.1)E+30	Tau
.	UXTauA	4900	2.20	1.63	59.8	PTD	(1.1±0.4)E-08[b]	···	Tau
.	V410 Xray6	3145	0.46	0.22	7.9	CTD	···	(7.8±1.6)E+28	Tau
.	2MJ1124118	3240	0.06	0.20	2.9	CTD	···	···	ChaI
.	Baud43	3445	0.25	0.32	6.5	PTD	···	(5.6±0.3)E+28	ChaI
T54	CHX22	5520	4.10	1.66	37.1	CTD	···	···	ChaI
.	CHXR22E	3420	0.20	0.31	7.4	CTD	···	(2.6±0.3)E+29	ChaI
.	CRCha	4900	2.54	1.70	16.9	PTD	(8.8±3.0)E-09[b]	(1.6±0.0)E+30	ChaI
T11	CSCha	4205	1.00	0.87	41.1	CTD	(1.2±0.4)E-08[b]	(2.8±0.1)E+30	ChaI
.	ISO91	3470	0.30	0.33	2.2	CTD	···	(2.8±1.0)E+28	ChaI
T25	Sz18	3470	0.20	0.33	8.1	CTD	(9.7±3.3)E-10[b]	···	ChaI
T35	Sz27	3850	0.40	0.56	15.3	PTD	(1.2±0.4)E-09[b]	(5.8±5.8)E+29	ChaI
T56	Sz45	3785	0.30	0.52	18.3	WTD	(1.5±0.5)E-09[b]	···	ChaI
T6	SZCha	5250	2.40	1.55	29.5	PTD	(2.4±0.1)E-09[b]	(1.2±0.1)E+30	ChaI
.	16126-2235	3470	0.80	0.34	12.2	PTD	···	(1.9±0.0)E+30	Oph off
.	16201-2410	6030	4.90	1.41	29.2	PTD	···	···	Oph off
.	16220-2452	3470	0.28	0.33	8.7	PTD	···	···	Oph core
.	16225-2607	4060	1.37	0.71	14.2	PTD	···	···	Oph off

Table 4—Continued

Num	IRS name	T_{eff} (K)	$L_\star$ $(L_\odot)$	$M_\star$ $(M_\odot)$	R_{wall} (AU)	TD type	$\dot{M}$ $(M_\odot/yr)$	L_X (erg/s)	region
.	16289-2457	5770	4.61	1.53	24.7	PTD	···	···	Oph off
.	DOAR28	4350	1.00	1.08	15.0	CTD	···	···	Oph off
.	GY195	3470	0.38	0.34	6.6	PTD	(1.0±0.5)E-09[d]	···	Oph core
.	IRS3	3580	0.39	0.38	13.4	PTD	(1.2±0.4)E-08[d]	(5.0±1.2)E+28	Oph core
.	Rox44	4900	3.00	1.77	26.7	PTD	(9.0±3.1)E-09[b]	(6.1±0.3)E+29	Oph off
.	SR9	4350	2.03	1.06	14.6	PTD	(1.2±0.4)E-08	···	Oph core
spID 50	LAL 106	3309	1.63	0.27	45.4	PTD	···	(1.2±0.3)E+29	N1333
spID 52	LAL 110	4060	1.01	0.71	18.0	PTD	···	(2.2±0.1)E+30	N1333
spID 57	LAL 129	4060	0.92	0.72	23.2	PTD	···	(3.7±1.6)E+28	N1333
spID 73	LAL 171	4900	8.38	2.45	32.2	PTD	···	(8.4±0.2)E+30	N1333
spID 101	LAL 245	3370	0.07	0.26	8.4	PTD	···	···	N1333
spID 110	LAL 279	3525	0.02	0.31	3.7	PTD	···	···	N1333
spID 116	LAL 300	4205	1.17	0.87	5.0	PTD	···	···	N1333
spID 136	LAL 321	3955	0.83	0.63	12.3	CTD	···	(1.7±0.1)E+30	N1333
spID 137	LAL 331	3955	0.23	0.66	6.6	CTD	···	(1.3±0.2)E+29	N1333

Note. — The calculation of R_{wall} is explained in Section 4.2, and the values listed in the column have an uncertainty of about 33 %. $\dot{M}$ of ONC and L1641 is from this work. $\dot{M}$ for other regions are from the literatures. L_X are all from XMM-Newton Serendipitous Source Catalog (Watson et al. 2009b). The energy band is total energy band of XMM-Newton (0.2-12 keV).

[a]Najita et al. (2007)

[b]Espaillat et al. (2011)

[c]Güdel et al. (2007)

[d]Natta et al. (2006)

Table 5. Sub-classification of TDs

ID (1)	name (2)	region (3)	n_{K-6} (4)	n_{13-31} (5)	$EW(10\mu m)$ (6)	subtype (7)	$IDEF$ (8)
1	8336884-5290	ONC	N	N	Y	WTD	0.43
5	8343944-5609	ONC	N	N	Y	PTD	0.52[f]
8	8346141-5010	ONC	Y	Y	N	CTD	0.27[c]
11	8347711-5533	ONC	Y	Y	N	CTD	0.00
13	8350150-5595	ONC	Y	Y	N	CTD	0.06
16	8353051-5229	ONC	Y	Y	N	CTD	0.07
18	8355083-4835	ONC	Y	N	N	PTD	0.58
19	8355371-5480	ONC	Y	Y	N	CTD	0.05
23	8357031-5072	ONC	N	N	Y	WTD	0.51[d]
24	8358147-5505	ONC	N	N	Y	PTD	0.62
25	8358862-4842	ONC	N	Y	Y	WTD	0.39
26	8359203-5026	ONC	Y	N	N	CTD	0.13
29	8361167-5475	ONC	Y	Y	N	CTD	0.11
34	8365722-4816	ONC	Y	Y	Y	CTD	0.18
38	8367284-5798	ONC	Y	Y	Y	CTD	0.07
39	8368137-4860	ONC	Y	N	N	CTD	0.18
42	8369106-5686	ONC	Y	N	Y	WTD	0.41
44	8369980-5081	ONC	N	N	N	PTD[a]	0.65
47	8371984-5465	ONC	Y	Y	N	CTD	-0.78
53	8373930-6325	L1641	Y	N	N	CTD	0.15
59	8374388-6000	L1641	Y	Y	N	CTD	0.22
66	8375158-5162	ONC	N	Y	N	WTD	0.40
88	8377167-5247	ONC	n/a	n/a	n/a	CTD[b]	0.22
108	8379312-5776	ONC	N	N	Y	PTD	0.90
149	8385365-5106	ONC	N	Y	N	PTD	0.12[e1]
154	8386523-5715	ONC	Y	N	N	WTD	0.33
164	8387753-4993	ONC	N	N	Y	PTD	0.28[e1]
169	8389033-4773	ONC	Y	N	N	CTD	0.13
172	8389673-4794	ONC	N	N	N	CTD	0.36[c]
174	8390073-5082	ONC	Y	N	N	CTD	-0.33
176	8390285-5070	ONC	N	N	N	WTD[a]	0.41
177	8390554-6390	L1641	Y	Y	N	CTD	0.09
184	8394216-5181	ONC	Y	Y	N	WTD	0.36
185	8394454-5823	ONC	Y	N	Y	WTD	0.27
188	8396035-5861	ONC	Y	N	N	WTD	0.35
198	8399269-6612	L1641	N	N	Y	WTD	0.51[d]
203	8406280-6293	L1641	N	N	Y	PTD	0.64
204	8406609-6247	L1641	Y	N	N	CTD	0.08
211	8411618-6426	L1641	Y	N	N	CTD	0.12
218	8416389-6503	L1641	Y	N	N	CTD	0.10
219	8416834-6225	L1641	Y	Y	N	CTD	0.00
221	8416978-6185	L1641	N	N	Y	PTD	1.18
223	8424570-6484	L1641	Y	Y	N	CTD	0.04
227	8440418-7404	L1641	N	N	Y	PTD	0.70
229	8444779-6608	L1641	Y	Y	N	CTD	0.04

Table 5—Continued

ID (1)	name (2)	region (3)	n_{K-6} (4)	n_{13-31} (5)	$EW(10\mu\mathrm{m})$ (6)	subtype (7)	$IDEF$ (8)
230	8445558-6860	L1641	Y	Y	Y	CTD	-0.13
237	8457266-7161	L1641	Y	Y	Y	CTD	0.00
239	8464666-7838	L1641	Y	N	Y	WTD	0.36
257	8502614-7795	L1641	Y	Y	N	CTD	0.09
260	8508501-7431	L1641	Y	Y	N	CTD	0.02
270	8519428-8120	L1641	Y	Y	N	CTD	-0.25
271	8520557-7775	L1641	Y	Y	N	CTD	0.08
275	8535781-7830	L1641	Y	Y	N	WTD	0.37
279	8538911-7999	L1641	N	Y	N	WTD	0.31
283	8547523-7831	L1641	Y	Y	N	CTD	0.03
290	8562845-8151	L1641	N	N	Y	PTD	0.78
291	8564835-8250	L1641	Y	Y	N	CTD	0.04
294	8567670-8803	L1641	Y	Y	N	CTD	0.14
297	8570949-8577	L1641	N	Y	Y	PTD	1.14
301	8576836-8303	L1641	N	N	Y	PTD	0.63[f]
302	8579480-8565	L1641	N	Y	N	WTD	0.39
303	8580634-8516	L1641	Y	Y	N	CTD	0.19
.	04202606	Tau	N	N	Y	PTD	0.52[f]
.	04125+2902	Tau	Y	Y	N	CTD	0.04
.	CoKuTau 4	Tau	Y	Y	Y	CTD	0.06
.	DMTau	Tau	Y	Y	Y	CTD	0.15
.	GKTau	Tau	N	N	Y	PTD	0.99
.	GMAur	Tau	Y	Y	Y	WTD	0.37
.	HKTau	Tau	N	Y	N	PTD	0.77
.	IPTau	Tau	N	N	Y	PTD	0.55
.	LkCa15	Tau	N	Y	Y	PTD	0.56
.	MHO3	Tau	N	N	Y	PTD	1.10
.	RYTau	Tau	N	N	Y	PTD	1.14
.	UXTauA	Tau	N	Y	N	PTD	0.74
.	V410 Xray6	Tau	Y	Y	Y	CTD	-0.04
.	2MJ1124118	Cha I	Y	Y	Y	CTD	-0.50
.	Baud43	Cha I	N	N	Y	PTD	0.45[e3]
T54	CHX22	Cha I	Y	Y	N	CTD	-0.03
.	CHXR22E	Cha I	Y	Y	N	CTD	0.18
.	CRCha	Cha I	N	N	Y	PTD	0.71
T11	CSCha	Cha I	Y	Y	N	CTD	0.15
.	ISO91	Cha I	Y	N	Y	CTD	-0.22
T25	Sz18	Cha I	Y	Y	N	CTD	0.06
T35	Sz27	Cha I	Y	Y	N	PTD	0.44[e2]
T56	Sz45	Cha I	Y	Y	Y	WTD	0.35
T6	SZCha	Cha I	Y	Y	N	PTD	0.61
.	16126-2235	Oph	N	Y	Y	PTD	0.49[e3]
.	16201-2410	Oph	N	Y	Y	PTD	0.54
.	16220-2452	Oph	N	N	Y	PTD	1.10
.	16225-2607	Oph	N	N	Y	PTD	0.47[e2]

Table 5—Continued

ID (1)	name (2)	region (3)	n_{K-6} (4)	n_{13-31} (5)	$EW(10\mu m)$ (6)	subtype (7)	*IDEF* (8)
.	16289-2457	Oph	N	N	Y	PTD	0.63
.	DOAR28	Oph	Y	Y	N	CTD	0.07
.	GY195	Oph	N	N	Y	PTD	0.65[f]
.	IRS3	Oph	N	N	Y	PTD	1.38
.	Rox44	Oph	N	Y	Y	PTD	0.90
.	SR9	Oph	N	N	Y	PTD	0.53
spID 50	LAL 106	N1333	N	N	Y	PTD	0.80[f]
spID 52	LAL 110	N1333	N	N	Y	PTD	0.55
spID 57	LAL 129	N1333	N	N	Y	PTD	0.57
spID 73	LAL 171	N1333	N	N	Y	PTD	0.72
spID 101	LAL 245	N1333	N	Y	N	PTD	0.75[f]
spID 110	LAL 279	N1333	N	Y	N	PTD	0.81
spID 116	LAL 300	N1333	N	N	Y	PTD	1.71
spID 136	LAL 321	N1333	Y	N	N	CTD	0.03
spID 137	LAL 331	N1333	Y	Y	N	CTD	0.22

Note. — Column (4) indicates whether an object passes the criteria of n_{K-6}; Column (5) indicates whether an object passes the criteria of n_{13-31}; Column (6) indicates whether an object passes the criteria of $EW(10\mu m)$; Column (7): subtype of TDs based on the values of *IDEF* in column (8). See Section 4.1.1 for a detailed explanation of *IDEF* and the subtype separation points of *IDEF*.; Column (8): *IDEF* is the inner disk excess fraction.

[a]OriA-44 and OriA-176 do not pass n_{K-6}, n_{13-31}, and $EW(10\mu m)$, but their SEDs resemble a TD's SED.

[b]we did not calculate its spectral indices because its IRS spectrum is not complete, but its SED resemble a TD's SED.

[c]OriA-8 and OriA-172 are selected as CTD, but $IDEF > 0.25$. The spectral type of the objects is M3 or later. When measuring ef using the median spectrum of objects with M3-M5 in Tau, the *IDEF* values are 0.45 and 0.65, respectively.

[d]OriA-23 and OriA-198 are selected as WTD with $IDEF = 0.51$. The spectral type of objects is M0 and K6.5 respectively.

[e1]OriA-149 and OriA-164 have $IDEF<0.5$, but they are selected as PTD because we do not know their spectral types, but the fluxes at wavelength ranges of 2-6 μmare comparable to that of the median spectrum.

[e2]T35 (Sz 27) and 16126-2607 are PTDs, but their *IDEF* are slightly less than 0.5. Their spectral types are M0 and K7, respectively.

[e3]Baud 43 and 16126-2235 are PTDs , but their *IDEF* are less than 0.5.

Their spectral types are M3.25 and M3.0, respectively. When measuring *IDEF* using the median spectrum of objects with M3-M5 in Tau, the *IDEF* values are 0.72 and 0.71, respectively.

[f]OriA-5, OriA-301, 04202606, GY 195, LAL 106, and LAL 245 have spectral types of M3 or later. Their *IDEF* estimated with K5-M2 median spectrum are higher than 0.5 and they are classified as PTDs. The *IDEF* estimated with M3-M5 median spectrum are much higher than the *IDEF* listed in this table: 0.94, 1.07, 0.87, 1.0, 1.5, and 1.14, respectively.

Table 6. number of transitional disks and age trend

region	Age (Myr)	CTD	WTD	PTD	total TD	disks
NGC 1333	< 1	2	0	7	9	53[a]
ONC	< 1	15	10	7	32	127[b]
L1641	1	19	5	6	30	114[b]
Tau	1.5	4	1	8	13	154[c]
ChaI	2	6	1	4	11	68[d]
Oph	0.3-2.1	1	0	9	10	90[e]

Note. — Number of transitional disks and the median age of each star-forming region. The median age of each star-forming region is taken from the literature listed below and references therein. The last column: n(disks) is the number of objects in our sample, which is complete for Class II objects and transitional disks with host stars of type M4 or earlier (see §2).

[a]We keep 53 objects after taking 4 Class I objects out from the 57 disk dominant objects reported in Arnold et al. (2012).

[b]from this work.

[c]This number comes from IRS survey of Taurus by Furlan et al. (2011).

[d]This number comes from IRS survey of Chamaeleon I by Manoj et al. (2011).

[e]This number is the number of disk dominant objects identified from IRS survey of Ophiuchus by McClure et al. (2010).

Table 7. Correlation summary I

Correlation	N	α	β	$corr$[b]	P[c] (%)	P_{range}[d] (%)
$\dot{M}$ vs. $M_\star/M_\odot$	69	-8.5±0.1	1.6±0.3	0.5±0.1	0.001	≪0.001-0.1
L_X vs. $M_\star/M_\odot$	56	30.1±0.1	1.1±0.3	0.5±0.1	0.01	<0.001-0.2
	55	30.1±0.1	1.1±0.3	0.4±0.1	0.3	0.01-2.6
$\dot{M}$ vs. L_X	42	-14.6±7.7	0.2±0.3	0.2±0.2	20.4	0.9-100
$M_\star/M_\odot$ vs. R_{wall}	98[a]	-1.0±0.1	0.7±0.1	0.8±0.1	≪0.001	≪0.001
	97	-1.0±0.1	0.7±0.1	0.7±0.1	≪0.001	≪0.001
$\dot{M}$ vs. R_{wall}	69	-10.1±0.4	1.1±0.4	0.4±0.1	0.07	0.001-1.2
L_X vs. R_{wall}	56[a]	28.5±0.3	1.2±0.3	0.6±0.1	≪0.001	≪0.001-0.01
	55	28.5±0.4	1.2±0.3	0.5±0.1	0.01	≪0.001-0.3
$\dot{M}/\dot{M}[M_\star, R_w]$ vs. R_{wall}	69	0.05±0.3	-0.7±0.3	-0.3±0.1	1.2	0.1-10
$L_X/L_X[M_\star, R_w]$ vs. R_{wall}	56[a]	0.05±0.3	-0.2±0.3	-0.1±0.2	46	2.5-100
	55	0.1±0.4	-0.2±0.3	-0.1±0.2	47	2.6-100
$\dot{M}/\dot{M}[L_X]$ vs. L_X	42	28.6±5.9	-1.0± 0.2	-0.7±0.1	≪0.001	<0.01-≪0.001
$L_\star$ vs. $M_\star$	98[a]	0.3±0.1	1.6±0.1	0.8±0.04	≪0.001	≪0.001
	97	0.3±0.1	1.5±0.1	0.8±0.04	≪0.001	≪0.001
$L_\star/L_\odot$ vs. R_{wall}	98[a]	-1.9±0.1	1.6±0.1	0.9±0.04	≪0.001	≪0.001
	97	-1.8±0.2	1.5±0.1	0.9±0.04	≪0.001	≪0.001
L_X vs. $L_\star/L_\odot$	56[a]	29.8±0.1	0.8±0.2	0.6±0.1	<0.001	≪0.001-<0.01
	55	29.9 ± 0.1	0.8±0.2	0.6±0.1	<0.001	≪0.001-0.01
$L_X/L_\star$ vs. $M_\star/M_\odot$	56[a]	-3.8±0.1	-0.4±0.4	-0.2±0.1	14	2.5-46
	55	-3.8±0.1	-0.3±0.3	-0.2±0.1	14	2.6-47
$\dot{M}$ vs. $L_\star/L_\odot$	69	-8.8±0.1	0.8±0.2	0.5±0.1	<0.001	≪0.001-0.1
$\dot{M}$ vs. $L_X/L_\star$	42	-10.2±1.1	-0.4±0.3	-0.3±0.2	5.4	0.1-53

Note. — Summary of the results from the Bayesian linear regression between X and Y: Y vs. X; $logY = \alpha + \beta logX$. Objects has a known spectral type are only included for the correlations.

[a]The results when we include OriA-88, which has a large value of R_{wall}, $M_\star$, and $L_\star$, and therefore is an outlier.

[b]$corr$ is the linear correlation coefficient between $logY$ and $logX$.

[c]P is the probability of getting $corr$ in random distribution.

[d]P_{range} is the range of P to get $corr$ in 1σ uncertainty.

Table 8. Correlation summary II: details by subtypes of TDs

Correlation	TD type	N	α	β	$corr$[b]	P[c] (%)	P_{range}[d] (%)	MRI[e]	XPE[f]	GPF[g]
$\dot{M}$ vs. $M_\star/M_\odot$	CTD	34	-8.9±0.6	0.7±1.8	0.1±0.3	57	1.9-26			Y
	WTD+PTD	35	-8.2 ± 0.1	1.9±0.5	0.7±0.1	<0.001	≪0.001-0.01			Y
L_X vs. $M_\star/M_\odot$	CTD[a]	30	30.3±0.2	1.8±0.6	0.6±0.2	0.05	≪0.001-2.9			Y
	CTD	29	30.5±0.3	2.2±0.9	0.5±0.2	0.6	0.002-11			Y
	WTD+PTD	26	30.0±0.1	1.0±0.4	0.5±0.2	0.9	0.007-14			Y
$\dot{M}$ vs. R_{wall}	CTD	34	-9.1±0.6	-0.1±0.6	-0.0±0.2	100	26-100	N	N?	Y
	WTD+PTD	35	-10.8±0.6	1.9±0.5	0.7±0.1	<0.001	≪0.001-0.01	Y	Y?	Y
$\dot{M}/\dot{M}(M_\star)$ vs. R_{wall}	CTD	34	0.8±0.7	-1.7±0.6	-0.6±0.2	0.02	≪0.001-1.9	N	Y?	Y
	WTD+PTD	35	-0.9±0.6	0.2±0.5	0.1±0.2	57	8-100	N	N	Y
L_X vs. R_{wall}	CTD[a]	30	28.3±0.4	1.4±0.3	0.7±0.1	0.002	≪0.001-0.05		Y?	Y
	CTD	29	28.2±0.4	1.5±0.4	0.7±0.2	0.002	≪0.001-0.6		Y?	Y
	WTD+PTD	26	28.9±0.9	0.7±0.7	0.3±0.3	14	0.1-100		Y?	Y
$L_X/L_X(M_\star)$ vs. R_{wall}	CTD[a]	30	-0.2±0.3	0.1±0.3	0.1±0.2	60	11-100	N	N	Y
	CTD	29	-0.2±0.4	0.1±0.4	0.1±0.2	61	11-100	N	N	Y
	WTD+PTD	26	0.7±0.9	-0.8±0.7	-0.3±0.3	14	0.1-100	N	N	Y
$\dot{M}$ vs. L_X	CTD	24	-17.1±9.9	0.3±0.3	0.3±0.3	15	0.2-100	N	N?	Y
	WTD+PTD	18	-8.3±10.2	0.0±0.3	0.0±0.3	100	23-100	N		Y
$\dot{M}/\dot{M}(L_X)$ vs. L_X	CTD	24	28.1±10.0	-1.0±0.3	-0.6±0.2	0.2	≪0.001-5.3	N	Y?	Y
	WTD+PTD	18	35.7±9.7	-1.2±0.3	-0.7±0.2	0.1	≪0.001-3.5	N	Y?	Y
$M_\star/M_\odot$ vs. R_{wall}	CTD	46	-1.0±0.1	0.6±0.1	0.8±0.1	≪0.001	≪0.001		Y	
	WTD+PTD	52	-1.1±0.2	0.8±0.1	0.7±0.1	≪0.001	≪0.001		Y	
$\dot{M}$ vs. $L_\star/L_\odot$	CTD	34	-9.3±0.2	-0.3±0.4	-0.2±0.2	26	1.9-100			Y
	WTD+PTD	35	-8.6 ± 0.1	1.2±0.2	0.8±0.1	≪0.001	≪0.001			Y
L_X vs. $L_\star/L_\odot$	CTD[a]	30	29.9±0.1	0.8±0.2	0.6±0.2	0.05	<0.001-2.8	Y		Y
	CTD	29	30.0±0.1	1.0±0.3	0.6±0.2	0.06	<0.001-3.2	Y		Y
	WTD+PTD	26	29.7±0.1	0.8±0.3	0.6±0.2	0.2	<0.001-4.3	Y		Y

Note. — Summary of the results from the Bayesian linear regression between X and Y: Y vs. X; $logY = \alpha + \beta logX$. The index [a,b,c,] and [d] have the same meanings as in Table 7.

[e] *MRI*: The inside-out disk evolution driven by Magnetic Rotational Instability.

[f] *XPE*: The disk dispersion by photoevaporation, specially X-ray photoevaporation

[g] *GPF*: Dynamical effects by infant giant planet formation.

Note. — N or Y checks indicate if a mechanism in the last three columns can explain the corresponding trends in a row.

Table 9. Correlation summary III: TDs in Orion A

Correlation	N	α	β	$corr^{b}$	P^{c} (%)	$P_{range}{}^{d}$ (%)
$\dot{M}$ vs. $M_\star/M_\odot$	50	-8.6±0.2	1.3±0.5	0.4±0.2	0.4	<0.001-16
L_X vs. $M_\star/M_\odot$	35[a]	30.2±0.1	1.0±0.3	0.5±0.2	0.2	<0.001-8
	34	30.2±0.2	0.9±0.4	0.4±0.2	1.9	0.02-26
$\dot{M}$ vs. L_X	33	-20.3±8.7	0.4±0.3	0.3±0.2	9	0.3-58
$M_\star/M_\odot$ vs. R_{wall}	55[a]	-1.1±0.1	0.7±0.1	0.8±0.1	≪0.001	≪0.001
	54	-1.0±0.1	0.6±0.1	0.8±0.1	≪0.001	≪0.001
$\dot{M}$ vs. R_{wall}	50	-9.8±0.5	0.7±0.4	0.3±0.2	3.4	0.2-49
L_X vs. R_{wall}	35[a]	28.8±0.3	1.0±0.3	0.6±0.1	0.01	<0.001-0.2
	34	28.8±0.4	1.0±0.4	0.5±0.2	0.3	<0.001-8.5
$\dot{M}/\dot{M}[M_\star]$ vs. R_{wall}	50	0.3±0.3	-1.0±0.3	-0.5±0.1	0.02	<0.001-0.4
$L_X/L_X[M_\star, R_w]$ vs. R_{wall}	35[a]	0.3±0.3	-0.3±0.3	-0.2±0.2	25	1.7-100
	34	0.4±0.4	-0.3±0.4	-0.2±0.2	26	1.9-100
$\dot{M}/\dot{M}[L_X]$ vs. L_X	33	24.0±6.1	-0.8±0.2	-0.7±0.1	<0.001	≪0.001-0.02
L_X vs. $L_\star/L_\odot$	35[a]	30.0±0.1	0.6±0.2	0.6±0.1	0.01	<0.001-0.2
	34	30.0 ± 0.1	0.7±0.2	0.6±0.2	1.0	≪0.001-1.9
$L_X/L_\star$ vs. $M_\star/M_\odot$	35[a]	-3.8±0.1	-0.7±0.3	-0.4±0.2	1.7	0.01-25
	34	-3.8±0.1	-0.6±0.4	-0.3±0.2	8.5	0.3-57
$\dot{M}$ vs. $L_\star/L_\odot$	50	-8.9±0.1	0.6±0.3	0.4±0.2	0.4	<0.001-16
$\dot{M}$ vs. $L_X/L_\star$	33	-8.3±1.3	0.1±0.4	0.1±0.2	58	9-100

Note. — Summary of the results from the Bayesian linear regression between X and Y: Y vs. X; $logY = \alpha + \beta logX$. Objects has a known spectral type and in Orion A are only included for the correlations.
The index ^{a,b,c,} and ^{d} have the same meanings in Table 7.

Table 10. Correlation summary IV: details by subtypes of TDs in Orion A

Correlation	TD type	N	α	β	$corr$[b]	P[c] (%)	P_{range}[d] (%)
$\dot{M}$ vs. $M_\star/M_\odot$	CTD	30	-9.2±0.5	-0.2±1.3	0.0±0.3	100	11-100
	WTD+PTD	20	-8.3 ± 0.3	2.1±0.7	0.6±0.2	0.5	0.002-8.1
L_X vs. $M_\star/M_\odot$	CTD[a]	24	30.3±0.2	1.4±0.5	0.5±0.2	1.3	0.01-15
	CTD	23	30.5±0.4	1.9±1.2	0.4±0.2	5.7	0.2-36
	WTD+PTD	11	30.2±0.1	0.5±0.4	0.5±0.3	12	0.3-56
$\dot{M}$ vs. R_{wall}	CTD	30	-8.8±0.6	-0.3±0.6	-0.1±0.2	60	11-100
	WTD+PTD	20	-11.1±0.9	2.0±0.8	0.7±0.2	0.06	$\ll$0.001-2.5
$\dot{M}/\dot{M}(M_\star)$ vs. R_{wall}	CTD	30	1.0±0.6	-2.0±0.6	-0.7±0.2	0.002	$\ll$0.001-0.5
	WTD+PTD	20	-1.1±0.8	0.2±0.7	0.1±0.3	67	8.1-100
L_X vs. R_{wall}	CTD[a]	24	28.6±0.4	1.1±0.4	0.6±0.2	0.2	$\ll$0.001-5.3
	CTD	23	28.6±0.6	1.2±0.5	0.5±0.2	1.5	0.02-16
	WTD+PTD	11	29.5±0.6	0.5±0.5	0.4±0.4	22	0.3-100
$L_X/L_X(M_\star)$ vs. R_{wall}	CTD[a]	24	0.2±0.4	-0.2±0.30	-0.1±0.2	64	15-100
	CTD	23	0.2±0.6	-0.2±0.6	-0.1±0.3	65	5.9-100
	WTD+PTD	11	1.1±0.6	-0.8±0.5	-0.6±0.3	5.1	0.02-37
$\dot{M}$ vs. L_X	CTD	23	-14.3±10.5	0.2±0.4	0.1±0.3	65	5.9-100
	WTD+PTD	10	-37.3±29.7	1.0±1.0	0.5±0.4	14	0.04-78
$\dot{M}/\dot{M}(L_X)$ vs. L_X	CTD	23	31.0±9.0	-1.1±0.3	-0.7±0.2	0.02	$\ll$0.001-1.5
	WTD+PTD	10	5.8±22.9	-0.2±0.8	-0.2±0.4	58	6.7-100
$M_\star/M_\odot$ vs. R_{wall}	CTD[a]	33	-1.0±0.1	0.6±0.1	0.8±0.1	$\ll$0.001	$\ll$0.001
	CTD	32	-0.9±0.1	0.5±0.1	0.7±0.1	<0.001	$\ll$0.001-0.03
	WTD+PTD	22	-1.1±0.2	0.8±0.2	0.8±0.1	<0.001	$\ll$0.001-0.03
$\dot{M}$ vs. $L_\star/L_\odot$	CTD	30	-9.3±0.2	-0.4±0.4	-0.3±0.2	11	0.5-60
	WTD+PTD	20	-8.8 ± 0.2	1.4±0.4	0.8±0.1	0.002	$\ll$0.001-0.06
L_X vs. $L_\star/L_\odot$	CTD[a]	24	30.1±0.1	0.7±0.2	0.6±0.2	0.2	<0.001-5.3
	CTD	23	30.0±0.1	0.7±0.2	0.5±0.2	1.5	0.02-16
	WTD+PTD	11	30.0±0.1	0.5±0.2	0.6±0.3	5.1	0.02-37

Note. — Summary of the results from the Bayesian linear regression between X and Y: Y vs. X; $logY = \alpha + \beta logX$. Objects has a known spectral type and in Orion A are only included for the correlations.
The index [a,b,c,] and [d] have the same meanings in Table 7.